國　立　交　通　大　學

電控工程研究所

碩士論文

直流靜電式微型振動發電機之分析、設計與製作

Analysis, Design, and Fabrication of a DC Electrostatic Vibration-to-Electric Micro Power Generator

研究生　：張經富

指導教授：邱一　博士

中華民國九十九年七月

直流靜電式微型振動發電機之分析、設計與製作

Analysis, Design, and Fabrication of a DC Electrostatic Vibration-to-Electric Micro Power Generator

研 究 生:張經富 Student: Chin Fu Chang

指導教授:邱一 Advisor: Yi Chiu

國立交通大學

電控工程研究所

碩士論文

A Thesis
Submitted to Department of Electrical Control Engineering
College of Electrical Engineering
National Chiao Tung University
In Partial Fulfillment of the Requirement
For the Degree of
Master of Science
In

Electrical Control Engineering

July 2010
Hsinchu, Taiwan, R.O.C.

中華民國九十九年

中文摘要

由於近年來在低功率 VLSI 以及 CMOS 技術的發展，積體電路的能量需求已經降低至數十μW 的程度，由環境獲取能量來驅動低功率的遠端感測器成為可能。微機電系統是一個整合機械元件與電子電路的平台，在全世界的發展日漸流行。藉由使用微機電系統科技，具有整合電子元件的機械能量獲取器已具有提供低功率元件能量的能力。

本論文中，我們提出了對於一直流式振動至電能轉換器的新穎設計與分析方法。在一平方公分的晶片面積及 40V 輸出電壓的限制下，由 3.6V 電壓以及 120Hz 振動源驅動，最佳化的輸出功率在有外加 4 克質量塊以及無外加質量塊的情況下分別為 40.5 μW 以及 0.87 μW。

本元件是在 SOI 晶圓上利用深矽蝕刻技術製作。與先前的元件做比較，應用低壓氣相沉積技術所沉積的氮化矽薄膜提升了梳齒結構的絕緣能力。在利用高精準度陰影遮罩的定義下，元件接腳以及開關側向包覆改由金作為沉積材料，解決了先前使用鋁所造成的氧化問題，同時也減少了漏電電阻的產生。利用激振器所測量的共振頻率與設計值相符。元件的可變電容以及寄生電阻皆已量測，其可變電容範圍為 94pF 至 485pF，寄生電阻由 103MΩ提升為 156MΩ。機械式接觸開關經由測試已經確認其可正常工作。然而，由於不垂直的梳齒結構，能量轉換的過程中只產生較低的電壓。輸出功率的測量仍然在進行中。

Abstract

Energy scavenging from ambient environment becomes feasible to power independent remote sensors or portable devices due to low power VLSI and CMOS technology development. The requirement of power consumption has been reduced to a few tens of microwatts. Micro-Electro-Mechanical System (MEMS) is a platform that integrates mechanical devices with electric circuit. The development of MEMS is increasingly popular in the world. By using MEMS technology, a mechanical energy harvester with electric component is capable of supplying those low power devices.

In this thesis, the novel design and modeling method as well as the fabrication and measurement of a DC capacitive vibration-to-electric energy converter are introduced. With the device area constraint of 1 cm^2, bias by a 3.6V battery, output voltage limited to 40V, and operation frequency of 120Hz, the optimum output power is 40.5μW and 0.87 μW for devices with and without a 4 gram external mass attachment, respectively.

The device was fabricated in SOI wafers with deep silicon etching technology. Compared with previous devices, LPCVD nitride improved the isolation of fingers. Gold pads and switch lateral coverage defined by the high precision shadow mask had reduced the aluminum oxidation problem and reduced the leakage resistance. The resonant frequency measured by a shaker agreed with our design value. Variable capacitance of 94pF to 485pF was measured. The parasitic resistance was improved from 103MΩ to 156MΩ. The mechanical contact switch was test and workable. However, due to non vertical combs fingers, lower voltage was generated in the conversion process. The output power measurement is still in progress.

致謝

在經歷許多無法想像的磨練以及挑戰之後，我的碩士生涯終於步入尾聲。首先最感謝的就是我的指導教授邱一老師。老師在研究上一絲不苟的態度實在令人敬佩。老師在我的研究中也時常替我發現問題並提供有用的建議。在嚴格的指導下，這三年中學習到的東西是當初大學畢業的我想像不到的。老師在最後幫忙修改論文的付出，也使得我的論文能夠變得更加流暢明瞭。希望在未來進入社會後能將這段時間所受的訓練學以致用，創造自己的價值。

感謝口試委員方維倫老師以及施錫富老師。老師在繁忙中還安排時間前來，並且對我的論文提出非常有用的建議。感謝實驗室的學長曾繁果以及陳弘諳的經驗傳承，使我的研究能夠順利銜接。至於其他學長黃煒智、張子麟、吳昌修、揚昇儒，也提供了寶貴的研究經驗，雖然相處時間不長但還是要謝謝你們。

感謝一路上與我一起打拼的同學林健安，你在實驗以及製程上的經驗比我多上不少，也時常跟你請教製程中發生的問題。在研究生涯中也時常互相打氣，在苦悶的研究生活中增添不少動力。希望你將來能夠鴻圖大展。

還有要感謝我的大學同學。雖然你們許多人都已離開學校很久了，但是先前的情誼能夠在我碩士生涯的前中期提供給我精神上很大的支持，非常謝謝你們。另外要特別感謝我的好友范澤崴，即使身處軍中依然時常關心我的情況。

另外還要感謝在方維倫老師實驗室提供儀器幫忙做實驗數據的量測，使得我的研究時間能夠減少許多。實驗室碩二學弟妹劉鴻智、陳政安、莊哲明、陳姿穎、劉俊宏及碩一的學弟李彥傑、吳彥霆，感謝你們在這段日子裡的陪伴，使得實驗室的氣氛能夠歡樂不少，我由衷的希望你們能夠研究順利並且早日畢業。

還有要感謝我的母親以及姐姐，能夠支持我讀完碩士學位，將來一定要更加努力使你們過更好的生活。最後要感謝的就是親愛的素華，即使距離遙遠，仍在我人生最低潮的時候陪伴我度過，如果沒遇見妳我想我的人生還是一樣的平淡。

至於一路上所有幫助過我的人，在此致上我最高的謝意。

Table of Content

中文摘要 i

Abstract..ii

致謝..iii

Table of Content..iv

List of Figures..vii

List of Tables..x

Chapter 1 Introduction..1

1-1 literature review 2

1-1-1 Light exposure..2

1-1-2 Thermalelectric effect 4

1-1-3 Human body movement 5

1-1-4 Wind..7

1-1-5 Ambient vibration 8

1-1-6 Summary of power sources..9

1-2 Ambient vibration energy conversion..9

1-2-1 Electromagnetic energy conversion 10

1-2-2 Piezoelectric energy conversion 12

1-2-3 Electrostatic energy conversion 14

1-2-4 Comparision of vibrational energy conversion technologies........16

1-3 Thesis Objective and organization..17

Chapter 2 Principle and Design..20

2-1 Characteristics of vibration sources..20

2-2 Operation principle 22

2-3 Device design..24

2-3-1 Auxiliary battery supply 25

2-3-2 Variable capacitor design..26

2-3-3 Dynamic analysis..29

2-3-4 Static analysis..35

2-4 Optimizing process 37

2-4-1 Conditions for nprmal oscillation discussion..40

2-4-2 Optimum design..42

2-5 Previous design 54

2-6 Summary 55

Chapter 3 Fabrication Process **56**

3-1 Fabrication process flow 56

3-2 Process issues and solutions....67

3-2-1 Non-ideal effects in the ICP etching 67

3-2-2 Silicon nitride deposition 69

3-2-3 Metal deposition issued....71

3-3 Fabricated device 76

3-4 Summary 79

Chapter 4 Measurement and Results **81**

4-1 Mechanical measurement....81

4-1-1 MEMS Motion Analyzer measurement 81

4-1-2 Vibration measurement by our shaker 84

4-2 Static electrical measurement....86

4-2-1 Leakage resistance 87

4-2-2 Static measurement of SW1 92

4-3-3 Static measurement of SW2 94

4-3 Dynamic electrical measurement....95

4-4 Summary 97

Chapter 5 Summary and Future work....**99**

5-1 Summary 99

5-2 Future work....99

Reference 102

Appendix....107

List of Figures

Figure 1-1 Photovoltaic energy conversion [10]. 3

Figure 1-2 Thermoelectric energy converter [12]. 5

Figure 1-3 Components of suspended-load backpack [16]. 6

Figure 1-4 Inverted pendulum model of human walking [16]. 6

Figure 1-5 MEMS air flow harvester, with 10 pence coin for scale [19].. 8

Figure 1-6 Electromagnetic energy converter [21] 10

Figure 1-7 Three types of permanent magnet generation technologies [22] 11

Figure 1-8 (a) PMG-17 energy harvester from Perpetuum Co. [25] and (b) VEH-3 energy harvest from Ferro solutions[26]. 12

Figure 1-9 A two-layer cantilever beam piezoelectric energy converter [28]............. 13

Figure 1-10 A typical piezoelectric generator [28].. 14

Figure 1-11(a) Gap-closing and (b) overlap in-plane variable capacitors [21]........... 15

Figure 2-1 Vibration spectra by Roundy [9]. 21

Figure 2-2 Measurement of air purifier vibration. 21

Figure 2-3 Vibration spectrum of an air purifier. 22

Figure 2-4 Operation circuit of the electrostatic energy converter. 22

Figure 2-5 Variable capacitor schematic 23

Figure 2-6 Capacitor charging and capacitance change by vibration 23

Figure 2-7 Charge transfer and discharge process [36] 24

Figure 2-8 Lithium-ion rechargeable battery. 25

Figure 2-9 Top view of the in-plane gap closing variable capacitor topology. 26

Figure 2-10 A generalized layout design. 27

Figure 2-11 Single cell schematic 28

Figure 2-12 Schematic of the dynamic model. 29

Figure 2-13 Displacement of shuttle mass versus time. 31

Figure 2-14 Time shift for t and T scale....................................32

Figure 2-15 Boundary conditions between z_1 and z_2. 34

Figure 2-16 Fingers at maximum displacement....................................35

Figure 2-17 Optimization flow chart 38

Figure 2-18 Amplitude and power vs. spring constant 39

Figure 2-19 Amplitude and power vs. Frequency. 40

Figure 2-20 System energy versus driven frequency....................................41

Figure 2-21 Contour of output power and voltage with external mass attachment for various Q_r. 44

Figure 2-22 Contour of output power and voltage without external mass attachment for various Q_r. 48

Figure 2-23 Layout view of the previous device. 56

Figure 3-1 Fabrication process flow on the SOI device 64

Figure 3-2 Notching effect (a) schematic and (b) SEM micrograph [42]....................................68

Figure 3-3 (a) Notching occurred on the finger's bottom, (b) improved result [2] 69

Figure 3-4 Schematic of poor step coverage....................................70

Figure 3-5 Shadow mask. 71

Figure 3-6 (a) Gold deposition on SW1 and anchors (b) Gold deposition on SW2. ...72

Figure 3-7 (a) Upper part of a gold coated test finger, (b) close-up view. 73

Figure 3-8 Broken silicon oxide at the big through-wafer hole....................................73

Figure 3-9 (a) Cross section of test structure, (b) close-up view. 74

Figure 3-10 EDS result at square in Fig 3.9(b). 74

Figure 3-11 (a) Cross section view of test structure, (b) close-up view 130 μm below substrate surface, (c) gold particles on wavelike etching profile, (d)

wavelike etching profile......75
Figure 3-12 EDS result at square in Fig 3.11(c).. 75
Figure 3-13 (a) Fabricated die, (b) central hole for mounting the external mass. 77
Figure 3-14 Close-up view of (a) fingers, (b) serpentine spring......77
Figure 3-15 (a) Close-up view of Switch 1, (b) deposited gold on silicon. 77
Figure 3-16 (a) Top view of Switch 2, (b) close-up view of Switch 2......78
Figure 3-17 (a) Backside silicon removed under Switch 1 (b) close-up view. 78
Figure 3-18 Device with silicon nitride coating. 79
Figure 3-19 (a) Device with the external mass on PCB, (b) top view. 79

Figure 4-1 MMA system. 82
Figure 4-2 Frequency response with external mass. 82
Figure 4-3 Frequency response without external mass. 83
Figure 4-4 (a) Mechanical measurement schematic (b) measurement setup 85
Figure 4-5 (a) Device at rest (b) device at resonance of 118 Hz (c) input acceleration waveform.. 86
Figure 4-6 Leakage resistance measurement circuit. 87
Figure 4-7 Variable capacitor measurement circuit [43]......88
Figure 4-8 RC discharge time constant measurement for LPCVD deposition. 89
Figure 4-9 Measured variable capacitor versus displacement. 90
Figure 4-10 Cross-section of non-parallel capacitor......91
Figure 4-11 C_{actual}/C_{ideal} versus oblique angle. 92
Figure 4-12 4.12 SEM photo (a) Close-up of non-parallel capacitance (b) rough surface of finger sidewall [47] 93
Figure 4-13 DC model operation with mechanical switches. 93
Figure 4-14 Mechanical switch SW1 is (a) off (b) on. 93

Figure 4-15 Charge Voltage. 94

Figure 4-16 SW2 with (a) no applied voltage, (b) 98 V applied voltage (pull-in). 94

Figure 4-17 Voltage on the variable capacitor. 95

Figure 4-18 Voltage on the variable capacitor and input acceleration. 96

Figure 4-19 (a) SW2 overview, (b) SW2 schematic circuit. 96

Figure 4-20 Schematic of Switch2 control method. 97

Figure 5-1 AC mode operation of the electrostatic energy converter. 100

List of Tables

Table 1-1 Comparison of power sources 9
Table 1-2 Comparisons of three types of vibrational energy converter [21] 17
Table 2-1 Fixed parameters of optimizing process. 37
Table 2-2 Free parameters of optimizing process 38
Table 2-3 System Energy at different instances and positions. 41
Table 2-4 Variable capacitor design parameters (with external mass). 47
Table 2-5 Variable capacitor design parameters (without external mass). 53
Table 2-6 Design parameter for previous device. 54
Table 3-1 Thin film property of LPCVD and PECVD nitride [46]. 71
Table 3-2 Element percentage at upper and lower part of sidewall. 76
Table A-1 Thin film property of LPCVD and PECVD nitride [46]. 107

Chapter 1 Introduction

Micro-Electro-Mechanical System (MEMS) is a multi purpose platform which integrates several different fields such as mechanical, electronic, control, optical, chemical, and biomedical technology. Through combining different types of subsystems on a common substrate, the most significant advantage is reduced cost due to miniaturization. Quality, performance, and durability may also be improved dramatically in many different cases. The concept of systems on chip (SOC) is made possible by the integration of these subsystems. This state-of-the-art technology has already been applied in numerous occasions. There are many common applications such as sensors and actuators, micro optical systems, biomedical systems, and aerospace and defense systems. The best known MEMS device is the accelerometer mounted on the hand controller of video gaming machine.

Due to the advance of manufacturing technology and the requirements from consumers, portable electronic devices have received increasing interests in recent years. However, conventional power storage devices have limited energy capacity, causing power supply a primary concern [1]. Generally, energy is stored in storage devices such as traditional batteries [2], micro-batteries [3], micro-fuel cells [4], ultra capacitors [5], micro heat engine [6], and radioactive materials [7]. High efficiency and low power loss are necessary to prolong the active time of these storage devices. Researchers have attempted to increase the energy density in those storage devices, but still, finite lifetime and high maintenance cost remain problems.

Thanks to the breakthrough of low power CMOS VLSI (Very Large Scale Integrated circuit) technology and the low duty cycle characteristics, it is feasible to develop applications such as wireless sensor networks or personal health monitoring

systems. These devices have reduced power consumption in the level of tens to hundreds of microwatts [8]. Scavenging ambient energy from the environment to power these sensor nodes become a possible method. One can design a self-sustainable or self-renewable energy device by scavenging the environmental energy to supply part of or all of the consumed energy.

1.1 Literature review

Different technologies, such as light exposure, thermal gradients, human power, air flow, and vibration [9], can be used to scavenge or harvest energy from the environment. The environment is a sustainable energy supply compared with the common storage devices like batteries or fuel cells. Various approaches to convert energy from the environment to electrical energy to drive low power electronics are reviewed in this chapter. Due to the inexhaustible nature of scavenged energy, the performance of the energy devices is characterized by their power density, instead of energy density used for traditional storage devices.

1.1.1 Light exposure

Light exposure is a popular and mature method to scavenge energy. Solar or photovoltaic cells are the leading technology to convert solar energy directly to electricity with high efficiency. Solar cells can be manufactured by IC-compatible technologies with high quality, therefore causing its popularity. Such devices can supply low cost and pollution free energy.

Photovoltaic cells function by the photovoltaic effect [10]. When the cell is exposed to light, a light-induced voltage is generated. The photons of the incident solar radiation excite the electrons in the semiconductor, allowing the electrons to

move freely and thus cause an electric current flow through a load. The operation is shown in Fig. 1.1. For single crystal silicon, the device has efficiency ranging from 12% to 25%. The thin film polysilicon and amorphous silicon cost less than single crystal silicon cells but have lower efficiency [11].

In total, photovoltaic energy conversion can provide sufficient power and with a mature IC-compatible technology. However, the output power of photovoltaic devices depends heavily on the environmental circumstances. For example, the photovoltaic cells offer adequate power density up to 15 mW/cm^2 if the device is placed outdoor and operated primarily during daytime. However, in regular indoor office lighting conditions, the same photovoltaic cell will merely produce about 10 μW/cm^2 [10]. Because of the environmentally dependent characteristics, photovoltaic cells are limited to certain applications.

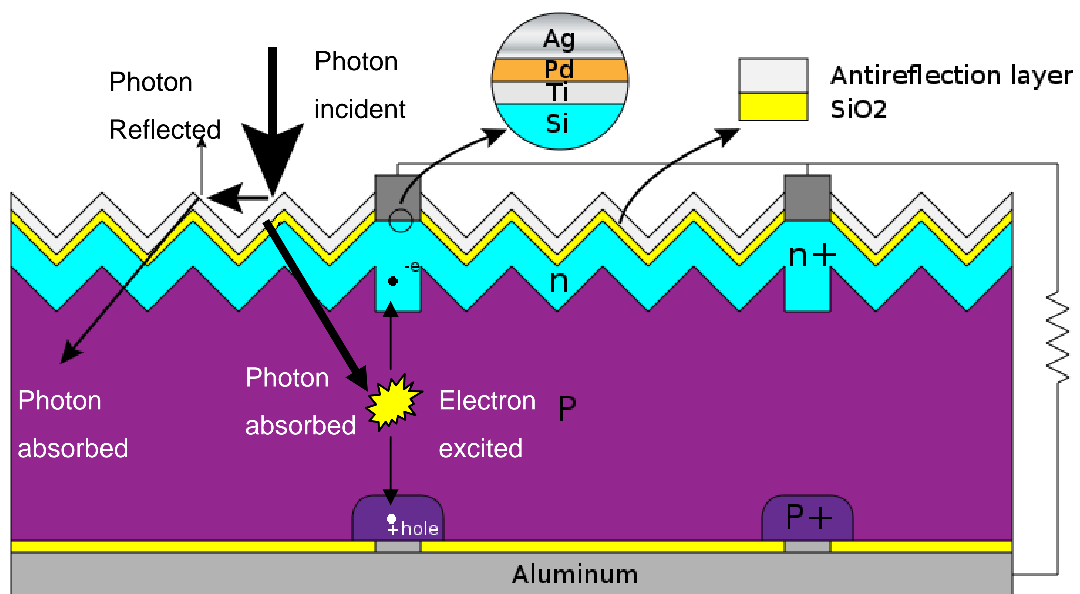

Fig. 1.1 Photovoltaic energy conversion [10]

1.1.2 Thermoelectric effect

Temperature gradient is basically a power source which can be converted into electric power. This thermal-to-electric behavior is described by the Seebeck effect, or the thermoelectric effect [12]. Once two different metals are connected in a closed loop, a temperature variation in the loop will cause electrons to move and a voltage potential is built up between the two metals or semiconductor junctions.

According to the Seebeck effect, the developed voltage is proportional to the temperature difference between the high temperature and low temperature ends, and to the Seebeck coefficients of the two materials. Large Seebeck coefficients and high electrical conductivity can increase conversion efficiency and decrease power losses and, therefore, is beneficial to the thermal-to-electric energy conversion.

Materials typically used for thermoelectric energy conversion, including Sb_2Te_3, Bi_2Te_3, Bi-Sb, PbTe, Si-Ge, polysilicon, BiSbTeSe compounds, and InSbTe, are not completely compatible to the IC process. In [13], annealing conditions have tremendous influence on the electrical resistivity of Bi-Sb and the thermoelectric generator performances as a consequence. An output power density of 140 $\mu W/cm^3$ for a 100 ˚C temperature difference is obtained but the temperature difference of this level is not commonly seen in a micro system [14]. So the output power is limited without large thermal gradients.

Fig. 1.2 illustrates the simplest thermoelectric generator comprising a p-type and a n-type thermoelements connected electrically in series and thermally in parallel. Heat is pumped into one side of the couple and rejected from the opposite side. An electrical current is produced, proportional to the temperature difference between the hot and cold junctions.

In general, connecting several thermocouple elements in series can achieve better performance. However, large series resistance increases ohmic power loss and thus

reduces the overall power conversion efficiency.

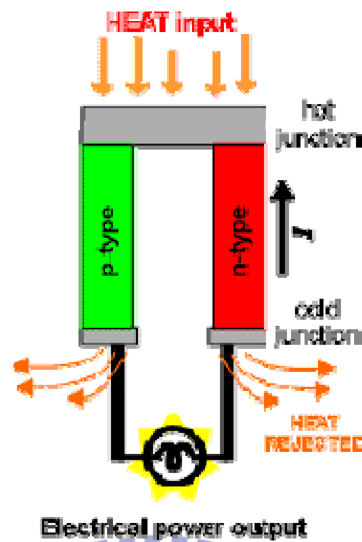

Fig. 1.2 Thermoelectric energy converter [12]

1.1.3 Human body movement

Human power is known as one of the most conventional energy sources. However, human-movement-to-electric power conversion has not been studied until recent years. The conversion principle is to transfer power from human activities to electric power. The activities include walking, breathing, body heat and so on. It is possible to power portable devices by harvesting energy from the human movement.

In recent years, needs of wearable electronic devices [15-17] have grown significantly. Many researchers focus their efforts on walking since this process seems a more practical energy source for wearable electronic devices. For example, a field scientist or explorer carrying heavy load can use a specially-designed power harvesting back pack to generate electric energy for his instruments such as GPS or notebook computers [16]. An average 7.37 W power output was measured from 6 participants who walked with speed ranging from of 4.0 to 6.4 km/hour and carried 20-, 29-, and 38 kg loads in addition to the fixed frame weighing 5.6 kg as shown in

Fig. 1.3 [16]. During walking, a person moves like an inverted pendulum, as shown in Fig. 1.4, causing the hip to move up and down by 4 to 7 cm, a considerable amount of mechanical energy must be transferred if the load is heavy.

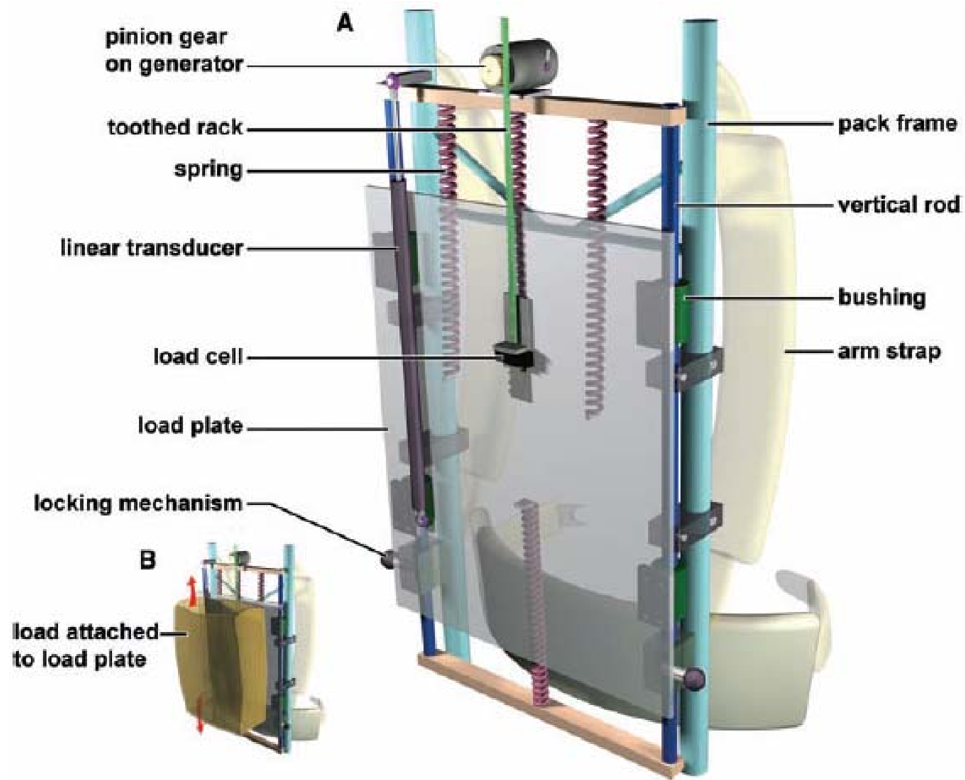

Fig.1.3 Components of suspended-load backpack [16]

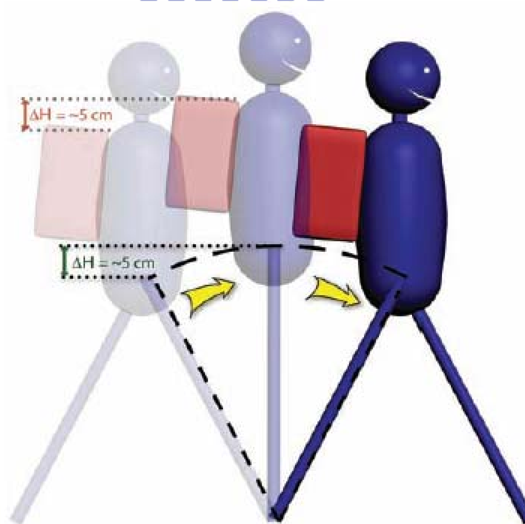

Fig.1.4 Inverted pendulum model of human walking [16]

"Heel-strike" devices are another walking power harvester [17]. However, the energy level of generation is relatively small (10 to 20 mW). This energy could be used in a variety of low-power applications, such as health monitors, self-powered emergency receivers, and radio frequency identification tags. The application is limited by the piezoelectrics and IC integration issues as well as power delivery issues. The piezoelectric shoe inserts offer a good solution for specific requirement such as RFID tags or other wireless devices worn on the foot.

1.1.4 Wind

Wind power is a renewable power generation technology to become a mainstream alternative for generation capacity expansion in the twenty-first century. This idea is to convert wind energy into a useful form like electricity by wind turbines or windmill. Due to the rotating characteristic of wind blades, the majority type of wind energy converter is electromagnetic conversion. Wind generated energy is also environmentally dependent which is similar to solar energy.

The power from wind is related to the air velocity. With slow wind at 3 m/s velocity, the average power is about 80 $\mu W/cm^3$. The maximum average power density of 1060 $\mu W/cm^3$ at 12 m/s air velocity was produced from a strong wind [18]. This indicates more usable power can be generated from high-velocity wind. However, wind power generation should be at large scale in order to obtain large amount of energy. Wind energy generators should be placed at locations where a sustainable and stable air flow is present. Therefore, wind power is a suitable energy source for wireless sensors for where a suitable wind source exists.

Few small-scale air flow harvesters have been proposed to date. One device based on MEMS technology is shown in Fig. 1.5 [19]. It comprises a 12-mm-diameter axial-flow turbine integrated with an electromagnetic generator. Tests showed that an

output power of 1 mW could be delivered at a volume flow of 35 l/min and a pressure drop of 8.4 mbar. For operation in a free stream, the same output power would be expected at a flow speed of around 40 m/s which is rarely seen in practical use.

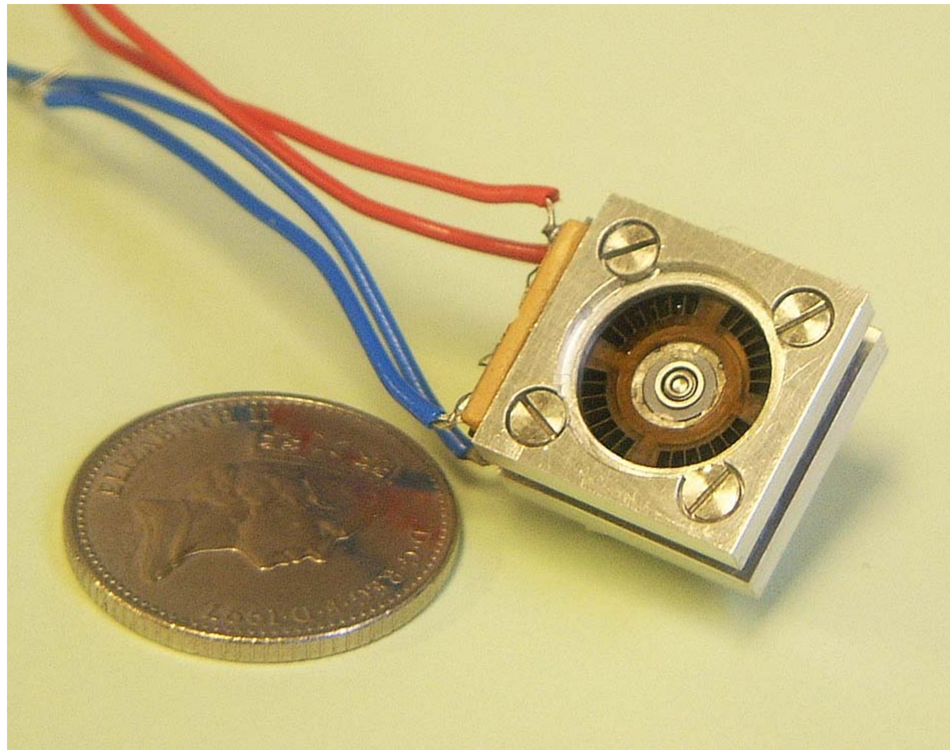

Fig. 1.5 MEMS air flow harvester, with 10 pence coin for scale [19]

1.1.5 Ambient Vibration

Vibration can also serve as an energy source. Ambient vibration can be observed in many environments. Most sources of vibrations are at low frequencies ranging from 60 to 200 Hz [9]. Different levels of mechanical vibration occur in exterior windows, aircraft, automobile, industrial equipments, and many small household appliances. Generally, the maximum power is extracted at resonance with the ambient vibration source. Theory and experiments show that the power density of more than 300 $\mu W/cm^3$ can be generated [20]. A more detailed discussion of this harvesting method is presented in Chapter 2.

1.1.6 Summary of power sources

Table 1.1 shows the comparison of the several power sources for portable devices. The values in this table are estimates taken from literatures or analysis based on the survey in the previous sections. Vibration is chosen as the source of energy scavenging in this study because of its ubiquity and sufficient power density.

Table 1.1 Comparison of power sources

Power sources	Power density	Commercially available?
Solar (outdoors) [10]	15, 000 μW/cm^2	Yes
Solar (indoors) [10]	10 μW/cm^2	Yes
Temperature gradient [13]	140 μW/cm^3 at 100°C gradient	Soon
Human power [15, 16]	330 μW/cm^2	No
Wind energy [18]	1060 μW/cm^3 at 12 m/s velocity	No
Vibration [20]	375μW/cm^3 at 120Hz, 2.5m/s^2	Yes

1.2 Ambient vibration energy conversion

Ambient vibration can be converted into electricity based on the overview described in previous sections. Vibration-driven harvesters will be introduced and discussed in this section. Three types of methods can be utilized to generate electricity from vibration sources.

In conventional macroscale engineering, electrical generators are based on electromagnetic transduction. In small-scale energy harvesting, two main techniques are added. Piezoelectric transduction is generally impractical for rotating systems but is well suited to the reciprocating nature of the motions typically used for harvesting. Electrostatic transduction, which is both impractical and inefficient for large machines,

becomes much more practical at small size scales and is well suited for MEMS implementation.

1.2.1 Electromagnetic energy conversion

As described by Faraday's low of induction, a change of magnetic flux linkage with a coil induces a voltage in the coil, driving a current in the circuit. The combined force on the moving charges in the magnetic field acts to oppose the relative motion, as described by Lenz's low. The mechanical work done against the opposing force is converted to energy in the magnetic field associated with the circuit inductance. A typical electromagnetic energy converter is shown in Fig. 1.6 [21]. Mechanical acceleration is produced by vibrations that cause the mass to oscillate. A coil is attached to the mass and moves through a magnetic field built by a permanent magnet. The induced voltage was produced by the change of magnetic flux. Thus, the output power is proportional to the magnetic field and coil number.

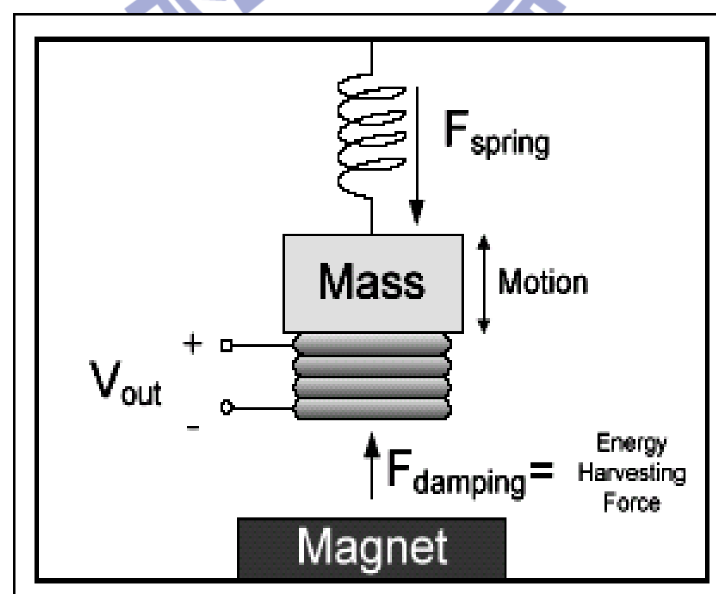

Fig. 1.6 Electromagnetic energy converter [21]

Microscale electromagnetic generation technologies can be broadly classified into three categories: rotational, oscillatory, and hybrid devices [22], as shown in Fig. 1.7. Rotational generators imitate the operation of macroscale motor/generators and have been designed to operate using rotational power from miniature turbines or heat engines. They are designed for continuous rotational motion under a steady driving torque. In contrast, oscillatory generators operate in a resonance mode, usually relying on relatively small displacements between a permanent magnet and coil to acquire power from environmental vibrations. Lastly, hybrid devices rely on vibrations, but convert linear motion into rotational motion using an imbalanced rotor.

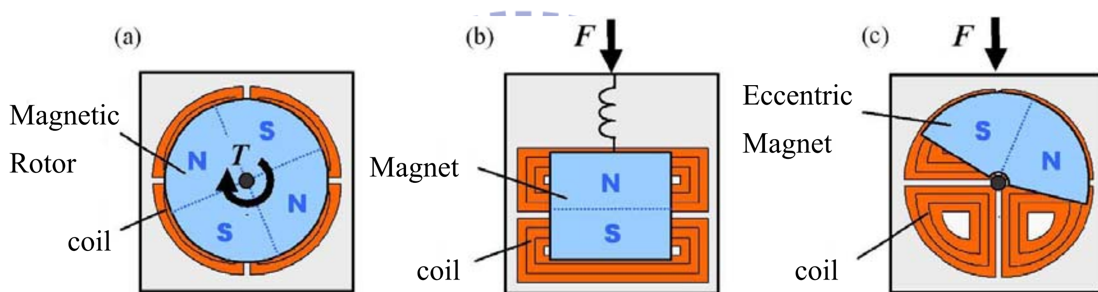

Fig1.7 Three types of permanent magnet generation technologies [22]

The most common issue for electromagnetic energy conversion is the relatively low induced voltage. Methods to increase induced voltage include increasing the number of turns of the coil or increasing the permanent magnetic field. However, it is difficult to fabricate large number of coils with planer thin film processes. Thus the power density of electromagnet converter is lower than other types of device.

The first microscale implementation of this type of vibration-driven harvester was reported in 1995 by Williams *et al*. [23]. The $25\,mm^3$ device demonstrated a peak power of 0.3 μW for a 0.5 μm vibrations at 4400Hz. Ching *et al*. used a small NdFeB magnet supported by a laser-micromachined Cu spring structure [24]. A maximum of 830 μW output power was obtained from a 200 μm vibrations at 110Hz,

and the devices successfully powered low data rate infrared and RF wireless communication modules.

There are also commercial products that utilize resonant magnetic power generation schemes. Perpetuum Co. Ltd. markets a 130 cm^3 vibration energy harvester tuned to 100 or 120 Hz vibrations that delivers 3.5 mW for 0.1 g vibrations or 40 mW at 1 g [25]. Ferro Solutions offers a similar 87 cm^3 product that can produce 10.8 mW for 0.1 g vibrations at 60 Hz [26].

1896

(a) (b)

Fig. 1.8(a) PMG-17 energy harvester from Perpetuum Co. [25]
and (b) VEH-3 energy harvest from Ferro solutions[26]

1.2.2 Piezoelectric energy conversion

Piezoelectric effect is a phenomenon whereby a strain in a material generates an electric field in that material, and inversely an applied electric field generates a mechanical strain [27]. The former can be used to convert energy. When an external force is applied, some of the work done is stored as elastic strain energy, and some in the electric field associated with the induced polarization of the material. If there is an external conduction route through a load, a current is generated to neutralize the net

charge produced as a result. Piezoelectric materials with high electromechanical coupling coefficients are generally ceramics, with lead zirconate titanate being the most common. The most common geometry is to place the piezoelectric material as a thin layer on a cantilever beam from which the proof mass is suspended.

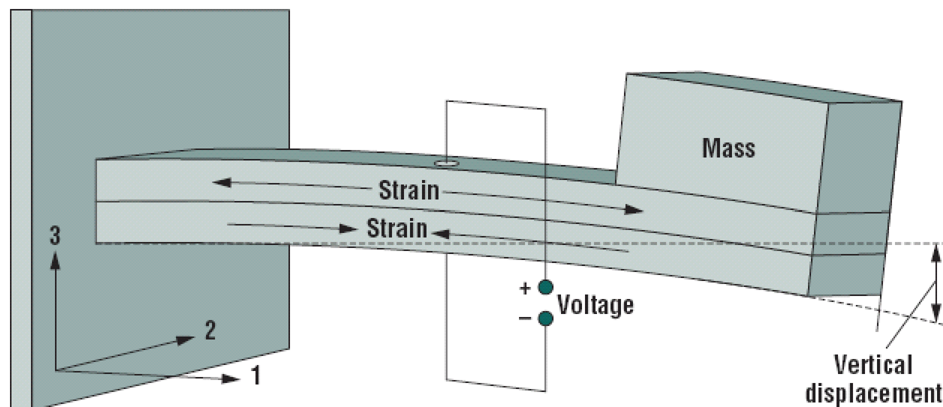

Fig.1.9 A two-layer cantilever beam piezoelectric energy converter [28]

The first reported piezoelectric microgenerators appear in the patent literature. Snyder described the use of a piezoelectric generator mounted on the wheels of a car to power the tire pressure sensors [29, 30]. The device would be powered from the wheel vibration during driving. If an abnormal tire pressure is detected, the signal could be reported to the driver via a low-power radio link. This kind of device is mounted on all newly produced cars in the United States due to the government regulation.

Roundy *et al.* described an RF beacon powered by both a solar cell and an optimized piezoelectric generator [28]. A power level of 375 μW was generated from an acceleration of $2.25\ \mathrm{m/s^2}$ at 60Hz, corresponding to amplitude of 16 μm.

1896

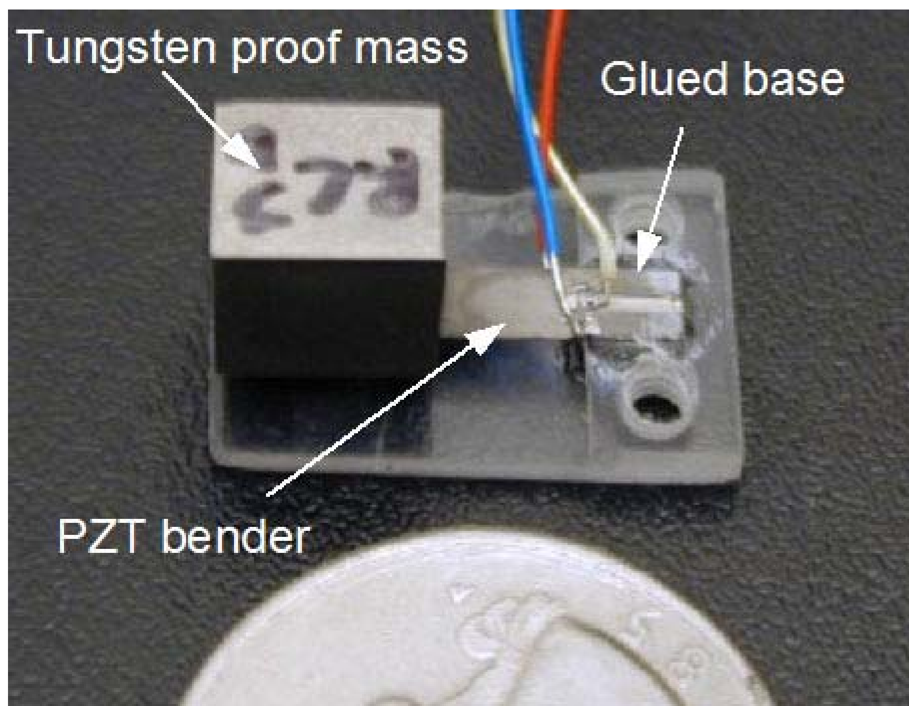

Fig. 1.10 A typical piezoelectric generator [28]

The difficulty of using piezoelectric material is the incompatibility with MEMS and CMOS processes. Another drawback of the piezoelectric converter is the requirement of additional circuitry to rectify the AC current. The supplementary circuitry has power losses and decreases the efficiency of the conversion. Most researches so far utilize bulk materials, which is still not suitable for integration with microsystem technology.

1.2.3 Electrostatic energy conversion

Electrostatic energy converters mainly use the change of capacitance of a mechanically driven variable capacitor as shown in Fig. 1.11. Mechanical forces from vibration are utilized to do work against the attraction of opposite charged parts. For a typical electrostatic energy converter, the variable capacitor is initially biased from a voltage source and disconnected instantly after the capacitor is fully charged. In the

constant charge process, when the capacitance decreases due to vibration, the voltage on the variable capacitor increases ($Q_{constant}$=CV) and thus the mechanical kinetic energy is transfered into electrical potential energy.

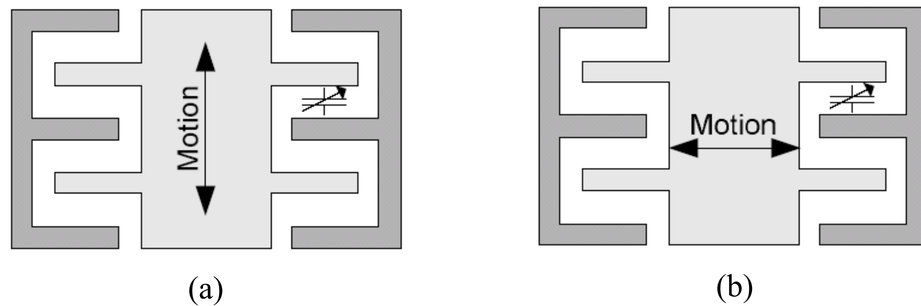

Fig. 1.11 (a) Gap-closing and (b) overlap in-plane variable capacitors [21]

MEMS variable capacitor can be fabricated through mature silicon-based micromachining process such as deep reactive ion etching. Therefore, it is relatively suitable for IC processes as mentioned earlier in this thesis. The converter also provides relatively high output voltage levels and adequate power density compared with electromagnetical counterparts. However, the disadvantage of the converter is the necessity of an auxiliary voltage source V_{in} used to initiate the conversion cycle. The lifetime of the voltage source is unfortunately limited. One solution proposed by Bernard *et al*. [32] was to use an inductive flyback circuitry to constantly feedbacks the temporary storage energy back to the external voltage supply for further usage. Another solution was proposed by Ingo Kuehne *et al*. [33] where the build-in voltage caused by the work function difference between two conductors was utilized as a bias source and thus no outer bias source is needed. In addition, one can also employ a moving layer of permanently embedded charge, or electret, to carry out electric energy harvesting [34], although such devices currently suffered from low power density and material instability problems. In addition, the output voltage in an electret

device is AC signal which needs to be rectified and thus the power loss is inevitable.

A capacitive energy converter was implemented by Meninger et al. [35]. The comb finger structure in MEMS technology was used with silicon on insulator (SOI) wafers. The simulation showed an output power of 8.6 μW with a device size of 1.5 cm × 0.5 cm × 1 mm from the vibration of 2.52 kHz. Another design was proposed by Roundy [9], which could achieve an output power density of 110 $\mu W/cm^3$ under vibration input 2.25 m/s^2 and frequency of 120 Hz.

In electrostatic capacitive energy conversion, the switch timing control should be controlled accurately to achieve maximum conversion efficiency. A prototype circuitry with the two ideal diodes was proposed by Roundy [9]. The experiment showed excessive power reduction due to the far from ideal operation of the diodes. The power consumption by the electronics or parasitic capacitive and resistive coupling still existed. Therefore, improved switch design is critical for better energy conversion efficiency.

1.2.4 Comparison of vibrational energy conversion technologies

From the above literature overview, the three types of vibrational energy converters are listed in Table 1.2 [21]. According to the characteristic comparison of these energy converters, electrostatic capacitive vibration-to-electric energy conversion is suitable for scavenging ambient energy because of its ubiquity in the environment and sufficient output power density. The fabrication technologies for electrostatic converter are very mature in MEMS system. The materials and process are compatible with IC process.

Table 1.2 Comparisons of three types of vibrational energy converter [21]

Converter	Power density	Advantages	Disadvantages
Piezoelectric	~200 μW/cm^3	High power density No bias source	AC output Process integration
Electromagnetic	< 1 μW/cm^3	No bias source	AC output Low power density Process integration
Electrostatic	1-100 μW/cm^3	DC output Process integration High power density	Bias souce

1.3 Thesis objectives and organization

Most electrostatic energy converters use switching devices such as diodes, MOSFET, or integrated mechanical switches for the control of conversion cycles. This kind of operation results in a nonlinear system, especially in the movement of mechanically variable capacitor. Many researchers [33, 36, 37] used simulation tools to model their devices. However, it is difficult to perform systematic analysis by using simulation tools. Oftentimes some parameters have to be assumed in order to run the simulation. For example, Roundy *et al.* assumed the minimum gap of their in-plane gap closing type converter to be 0.5 μm or 0.25 μm [38]. In fact, this value should not be chosen arbitrarily because it is critical for determining the maximum electrostatic spring constant, which will significantly affect the stability of the dynamic system. In our study, the minimum gap is determined by the initial gap and the amplitude of the oscillating mass. Both the amplitude and the initial gap are parameters in the

calculation. If the minimum gap is too small, the total effective spring constant will decrease dramatically. The pull-in effect can happen when the effective spring constant becomes to zero. The detail discussion will be presented in chapter2.

Another simplification is about the system nature frequency; many studies [36, 37, 39] ignored the interaction between the electrostatic attraction and the mechanical restoring force and simply designed the system nature frequency from mass and spring. In reality, during oscillation, the effective spring constant would not be simply the same as that of the mechanical system. In this study, the mechanical spring constant is also a varying parameter in our calculation.

In our previous work on capacitive energy conversion with integrated mechanical switches [39], Simulink was used to simulate the time domain behaviors of the device. The problem of time domain simulation was the difficulties to find the physics behind phenomena. Another problem of the previous device was the oxidation of the aluminum coating on the integrated mechanical switches. This results in high contact resistance. Moreover, even the improvement of fabrication processes and electrical power measurement were conducted, the leakage resistance still existed in the variable capacitance.

Based on our previous work on the electrostatic generator with integrated mechanical switches [39], the goals of this thesis include:

(a) Design and analysis of the optimal power generation for the electrostatic converter with or without the external mass attached,

(b) Novel method for modeling the dynamics of the energy converter,

(c) Solving the mechanical switch contact problem.

The organization of this thesis is as the following. The principle, design and optimization of the energy converter are discussed in Chapter 2. Fabrication processes and results are described in Chapter 3. The measurement results and discussions are

presented in Chapter 4. Finally, conclusion and future work will be discussed in Chapter 5.

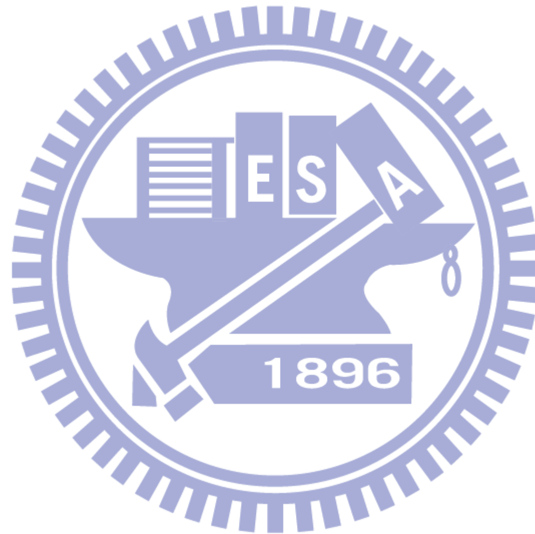

Chapter 2 Principle and Design

In this chapter, we will discuss the fundamentals of micro electrostatic capacitive energy converters. The energy generation depends on the change of capacitance of a variable capacitor caused by vibration. Kinetic energy is converted into electrical energy during this process. The variable capacitor is initially charged by an external power supply such as a battery. The charge-discharge cycles are controlled by mechanical switches. The optimal design and analysis are presented in this chapter. A theoretical model was established to analyze the device characteristics; the results are compared with simulation in our previous work [39].

2.1 Characteristics of vibration sources

Vibration sources are generally more ubiquitous. The output power of a vibration driven converter depends on the nature of the vibration source, which should be known in order to estimate the power generating capability. There are various kinds of vibration sources in the environment. Measurement of different vibration sources was conducted by Roundy [9], as shown in Fig. 2.1. From the low level vibration sources, two characteristics can be observed. First, fundamental peaks occur at a common low frequency. Second, the high frequency vibration modes are lower in acceleration magnitude than the low frequency fundamental modes. Low level vibration in typical households, offices, and manufacturing environments is considered also as a possible power source for wireless sensor nodes.

Our measurement of the vibration spectrum of an air purifier is shown in Fig. 2.2. A piezoelectric accelerometer (PCB Piezotronics model 353B17) was put on the air purifier and the data was collected by an oscilloscope. The fundamental vibration mode was at about 120 Hz, as observed by Roundy. The peak acceleration of the air

purifier is about 2.2m/s^2 at about 120 Hz, as shown in Fig. 2.3. These results will be used as our targeted input vibration source due to its common existence.

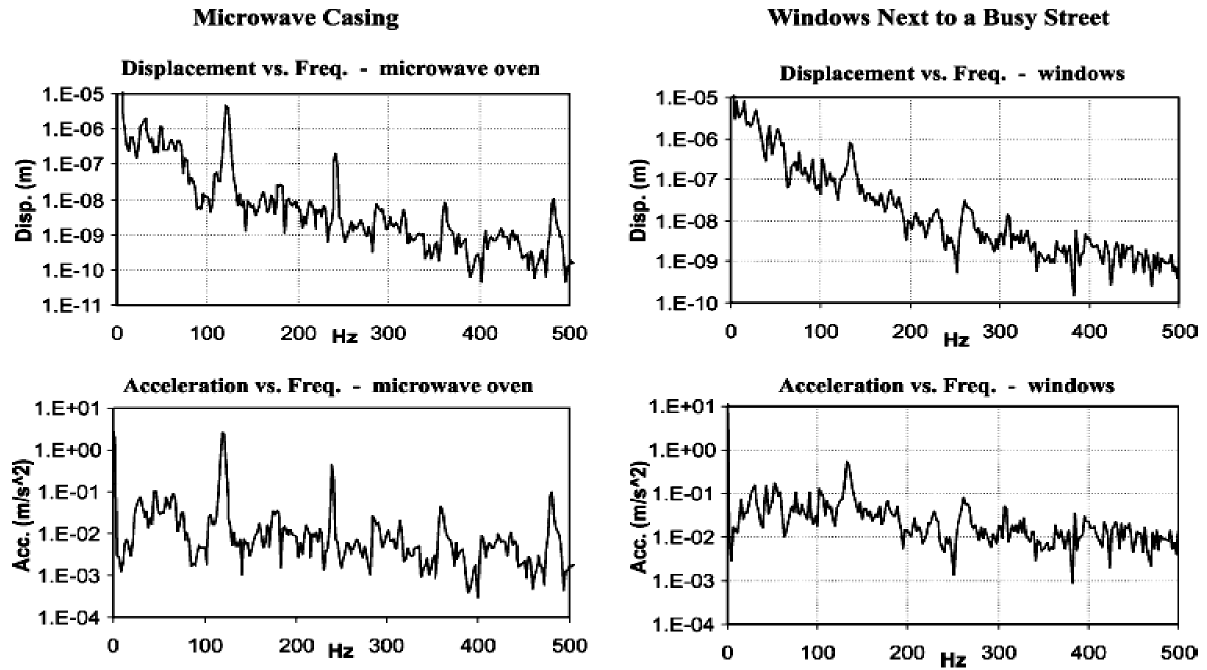

Fig. 2.1 Vibration spectra by Roundy [9]

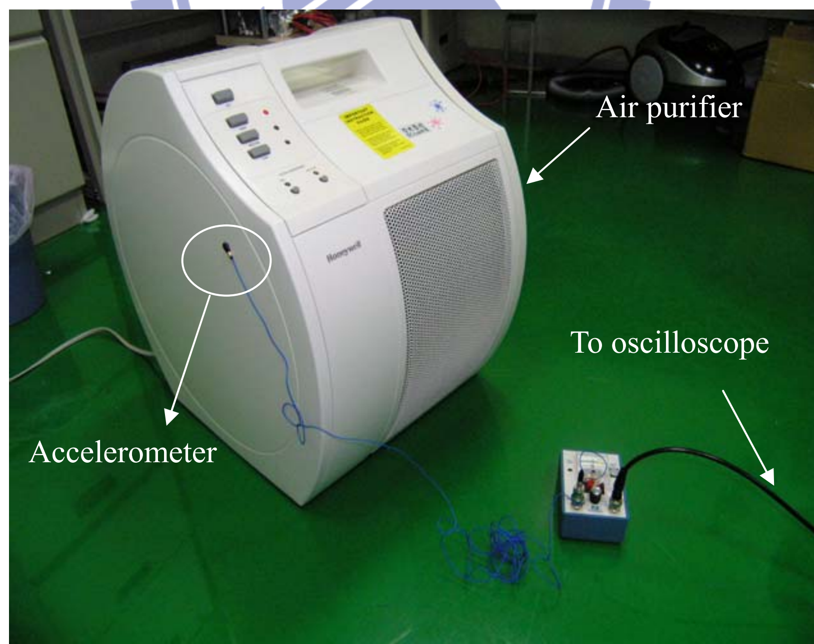

Fig. 2.2 Measurement of air purifier vibration

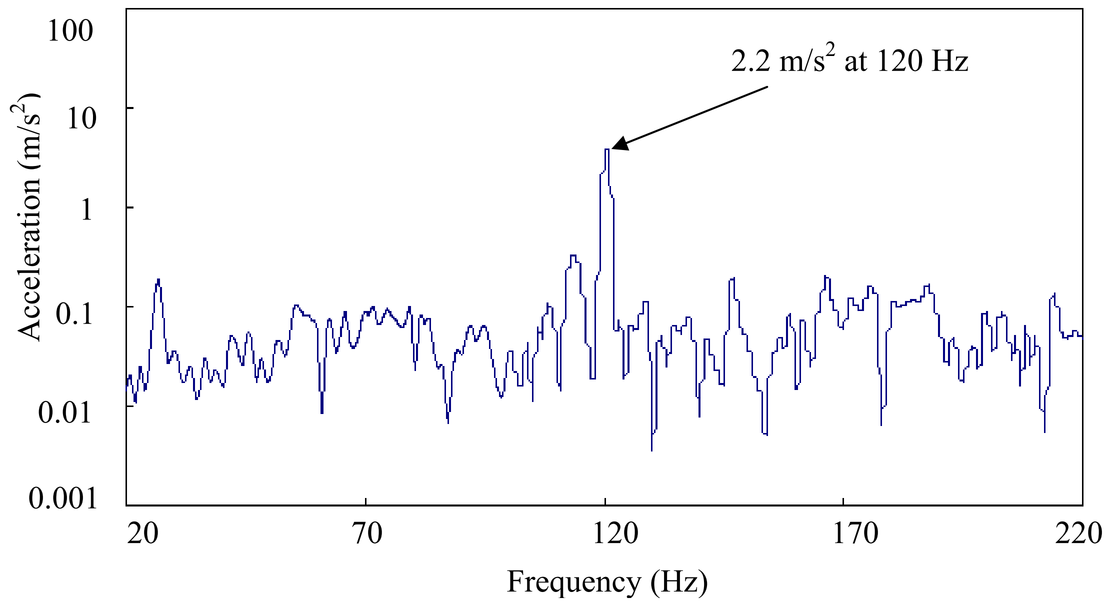

Fig. 2.3 Vibration spectrum of an air purifier

2.2 Operation principle

The main component of the electrostatic energy converter is a variable capacitor C_v [36]. A schematic circuit of the energy converter is shown in Fig. 2.4. It is composed of an auxiliary battery supply V_{in}, a vibration driven variable capacitor C_v and an output storage capacitor C_{stor}, which is connected to the load R_L. Two switches, SW1 and SW2, are used to connect these components and control the charge-discharge conversion timing [39].

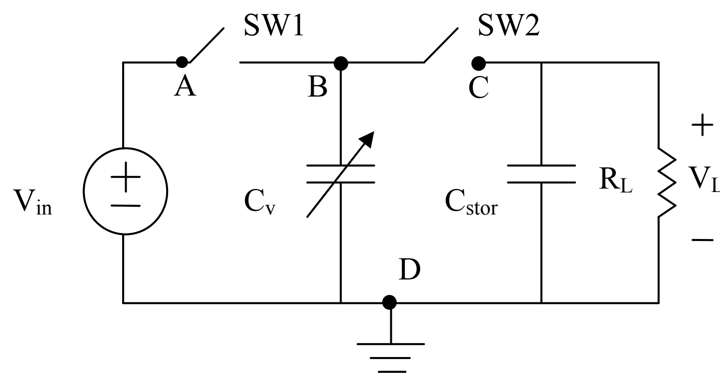

Fig. 2.4 Operation circuit of the electrostatic energy converter

1896 ES A

A more detailed schematic of the energy converter is shown in Fig. 2.5. The change of the capacitance is driven by the external vibration source. SW1 is implemented by a contact mechanism between nodes A and B. SW2 is actuated by the electrostatic pull-in force between nodes B and D. When node B reaches the pull-in voltage, it will be attracted by node D and touch node C.

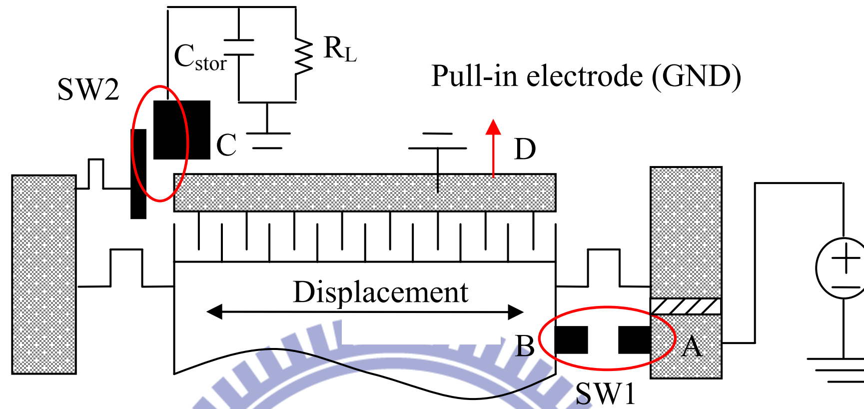

Fig. 2.5 Variable capacitor schematic

In the energy conversion cycle, the variable capacitor C_v is first charged by the auxiliary voltage supply V_{in} through the switch SW1 when C_v is at its maximum C_{max}, as shown in Fig. 2.6. After C_v is charged to V_{in}, SW1 is opened and the capacitance changes from C_{max} to C_{min} due to the electrode displacement by vibration. In the process, the charge Q on the capacitor remains constant (SW1 and SW2 both open). Therefore, the terminal voltage across the capacitor C_v is increased and the mechanical energy is converted to the electrical energy stored in the capacitor.

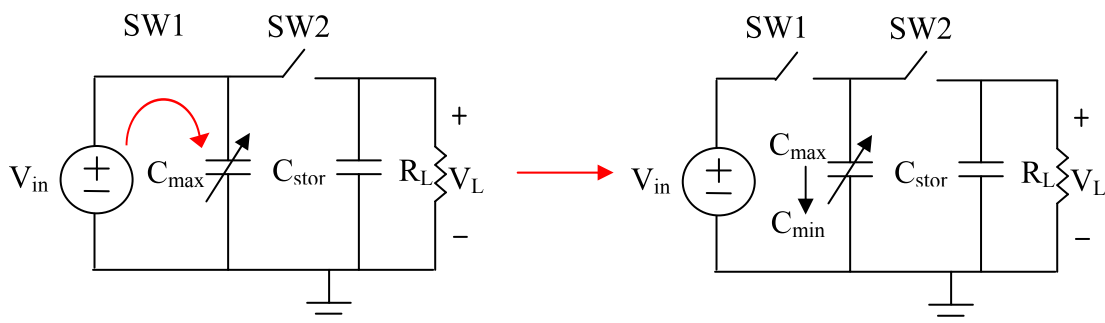

Fig. 2.6 Capacitor charging and capacitance change by vibration

When the capacitance reaches C_{min} and terminal voltage reaches $V_{max,}$ SW2 is closed and the charge redistributes between C_v and C_{stor} with balanced voltage Vo, as shown in Fig. 2.7 [36]. The energy stored in the variable capacitor C_v is transferred to the the storage capacitor C_{stor}. SW2 is then opened and C_v varies back to C_{max}, preparing for the next conversion cycle. We notice that there are two conversion cycles in one oscillation cycle since the period of oscillation contains two headings. The charge on C_{stor} is dissapated through the load resistance R_L with a time constant $\tau = R_L C_{stor}$ before it is charged again by $C_{v.}$ The output voltage V_L will eventually reach the steady state when the initial and final voltages of the charge-discharge process become equal.

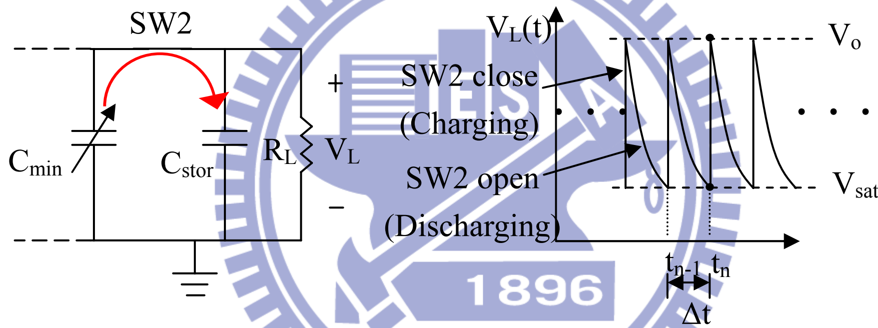

Fig. 2.7 Charge transfer and discharge process [36]

2.3 Device design

The variable capacitor is the main component of the converter. In this study, capacitors with and without an external mass are both considered. To meet the 120Hz vibration source, we used an external mass mounted on the device to adjust its resonance frequency. In the case without external mass, the 120Hz requirement results in a very small mechanical spring constant. Because of the small mass, the kinetic energy in the system is inevitably small, causing very low output power compared to the case with an external mass. However, the vertical force caused by the weight of the mass is also reduced so that damage caused by the external mass can be alleviated.

The output power strongly depends on the maximum capacitance C_{max}. But the electrostatic force also increases with the C_{max}, indicating that it may influence the movement of the mass for large C_{max}. Therefore, the variable capacitor must be designed by considering the 1 cm^2 device area constraint, the maximum capacitance C_{max} and the associated electrostatic force.

2.3.1 Auxiliary battery supply

The auxiliary battery supply is used to pre-charge the variable capacitor through SW1. Typical energy storage devices include capacitors, inductors and batteries. Capacitors and inductors have lower energy density. They often serve as short-term energy storage cells. Batteries, such as NiZn, NiMH, NiCd, and Lithium-ion (Li-ion), store energy chemically and are rechargeable. Among these types, Li-ion batteries (Fig. 2.8) offer the best performance with high energy density, high discharge rate, high cell voltage, long life span, and no memory effect. In this study, LIR1620 (3.6 V, Φ 16 mm, H 2.2 mm, 1.2 g) and LIR2016 (3.6 V, Φ 20 mm, H 1.8 mm, 1.6 g) Li-ion cells can be used as the auxiliary battery supply. Moreover, the battery can act as part of the external mass if it is well bonded on the device.

Fig. 2.8 Lithium-ion rechargeable battery

2.3.2 Variable capacitor design

SOI wafers with highly doped thick device layers and deep silicon etching technology were used to fabricate the devices. An in-plane gap-closing comb structure is used for the variable capacitor, as shown in Fig. 2.9. Compared with the in-plane overlap type comb structures, this topology has the advantage of larger capacitance change for smaller displacement. Compared with the out-of-plane gap closing capacitors, this topology has the advantage of lower mechanical damping loss and possibility to incorporate minimum gap control designs.

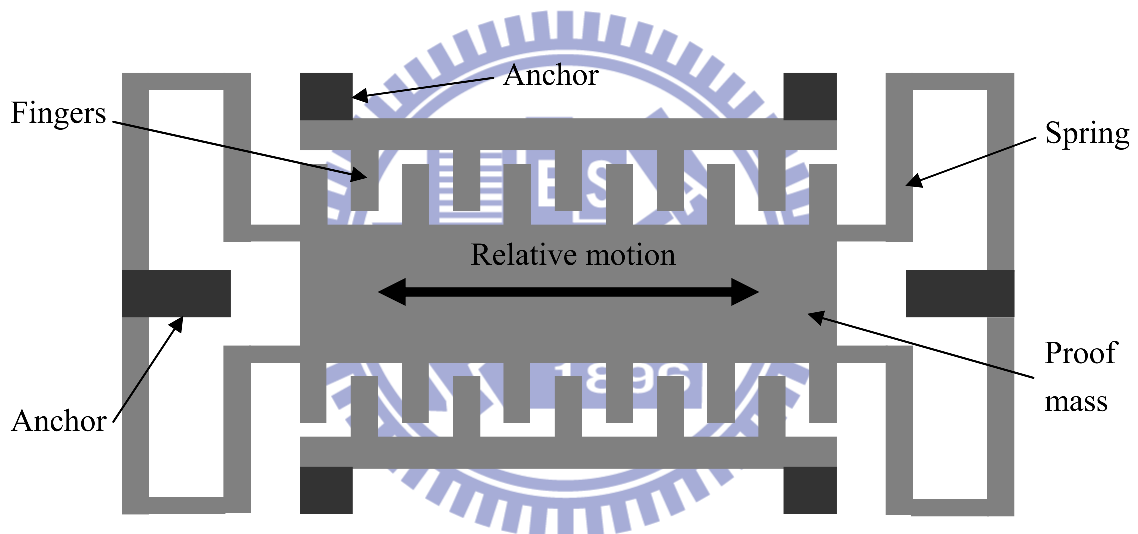

Fig. 2.9 Top view of the in-plane gap closing variable capacitor topology

The symbols used in the following discussion are listed below:

d: initial gap between comb fingers

d_{min}: minimum air gap between fingers

t: comb finger width

L_f: overlap length of comb fingers

h: thickness of device layer

z : relative displacement between the movable and fixed electrodes

N_g: number of variable capacitor finger cells

ε_0 : permittivity of free space ($\varepsilon_0 = 8.842 \times 10^{-12}$ F/m)

μ : viscosity of air at 1 atm ($\mu = 1.82 \times 10^{-5}$ Pa-sec)

α : damping coefficient depending on effective region ($\alpha \approx 1.74$)

The total variable capacitance between the comb fingers is [36]

$$C_v(z) = \frac{2N_g \varepsilon_0 L_f hd}{d^2 - z^2} \tag{2.1}$$

From this equation, the variable capacitance strongly depends on the comb finger structure. Layout design under restricted area directly affects the variable capacitance. A general model of the comb finger layout is shown in Fig. 2.10. The total layout area is limited to $1\,cm^2$. A number of free parameters can be adjusted to obtain the optimal design. In Fig. 2.10, the layout can be divided into three parts. First is the gray portion for the support of the fixed comb fingers. The second part is the rest of the layout area which is defined as S. The third part is the area occupied by the finger cells in S, which is defined as S', the area ratio is defined as

$$S_r = \frac{S'}{S} \tag{2.2}$$

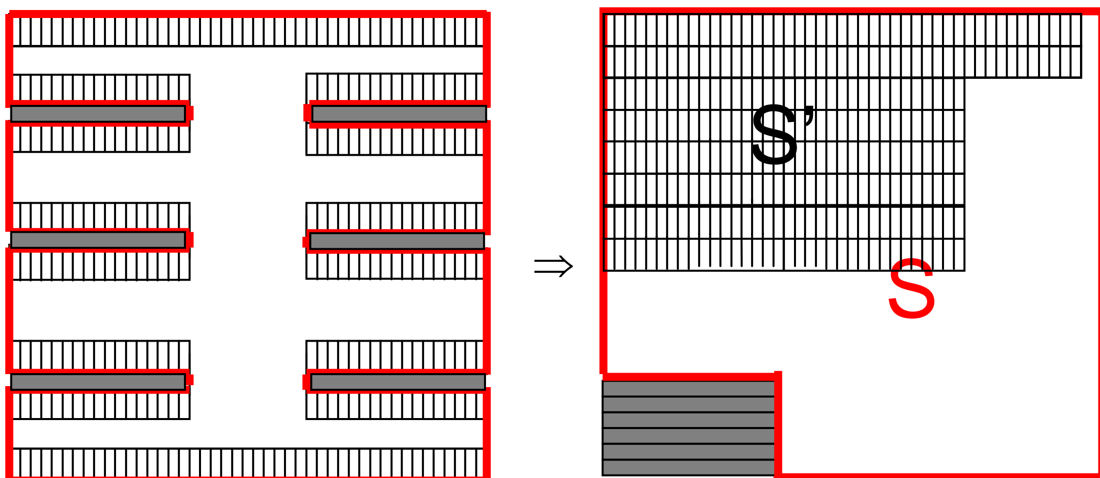

Fig 2.10 A generalized layout design

For the movable part of the variable capacitor, the area S' occupied by fingers can be divided into cells, as marked by the rectangle in Fig. 2.11. The air gaps around the fingers are equal to maintain consistent etching rate in the ICP deep RIE process.

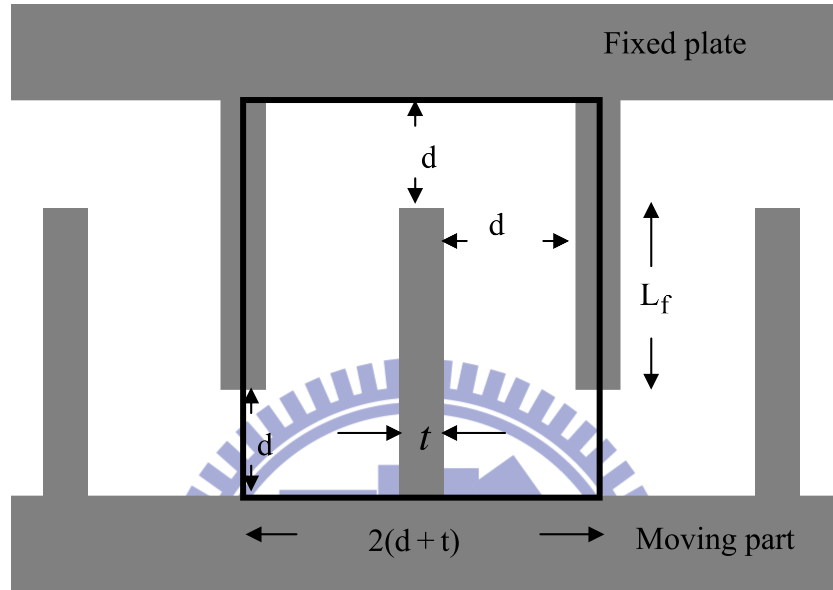

Fig 2.11 Single cell schematic

The number of fingers is the finger area S' in layout divided by the finger cell area

$$N_g = \frac{SS_r}{2(d+t)(L_f+2d)} \tag{2.3}$$

The mass of movable plate is

$$m_0 = \rho h\left[S(1-S_r) + N_g t(L_f + d)\right] \tag{2.4}$$

In these two equations, two free parameters, S_r and d, are utilized to optimize the layout design.

The device will be fabricated on SOI wafers. The thickness h is chosen as 200 μm to have large capacitance. The finger width t of 10 μm is restricted by the aspect ratio of up to 20:1 in the deep reactive ion etching process. A maximum device area of $1\ cm^2$ is set as the device size constraint.

2.3.3 Dynamic analysis

The dynamic analysis is performed to decide the mechanical spring constant k under certain proof mass m in order to achieve the theoretical maximum displacement under the targeted input vibration. The electro-mechanical dynamics of the variable capacitor can be modeled as a spring-damper-mass system, as shown in Fig. 2.12.

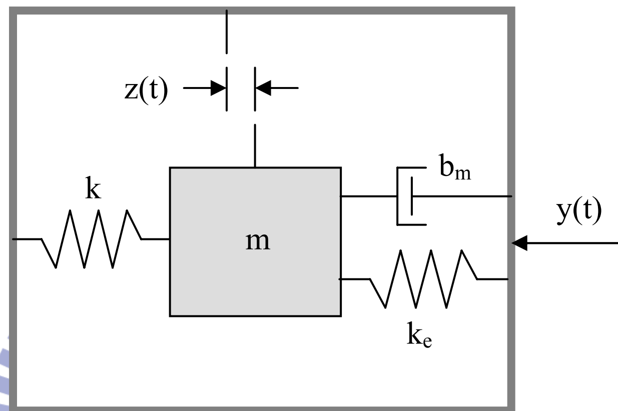

Fig. 2.12 Schematic of the dynamic model

The equation of motion is

$$m\ddot{z} + b_m\dot{z} + (k_0 + k_e)z = -m\ddot{y} \tag{2.5}$$

where y (=$Y_0 \sin\omega t$) is the displacement of device frame caused by the vibration, z is the relative displacement between movable and fixed plates, k_0 is the mechanical spring coefficient, $b_m\dot{z}$ is the mechanical damping force, and $k_e z$ is the electrostatic force caused by the charge on the capacitor, which acts as a negative spring force with k_e as the electrostatic spring constant.

The mechanical damping can be determined from experimental data. From our previous MMA (MEMS motion analyzer) measurements, the quality factor is approximately 6 to 8. The corresponding mechanical damping is 0.38 to 0.52 based on Eq. 2.6.

$$Q = \sqrt{\frac{km}{{b_m}^2}} \tag{2.6}$$

The electrostatic force induced by constant charge Q on C_v is [36]

$$F_e = k_e z = \left[\frac{-Q^2}{2N_g \varepsilon_o L_f hd}\right] z. \tag{2.7}$$

The force can be viewed as a negative spring force with a negative electrostatic spring constant k_e. The electrostatic spring constant is determined by the charge Q on the variable capacitor which alternates between Q_{max} and Q_{min} in the charge-discharge process. The corresponding electrostatic spring constants are defined as $k_{e,max}$ and $k_{e,min}$. A newly introduced parameter Q_r is defined as the charge ratio between Q_{min} to Q_{max}

$$Q_r = \frac{Q_{min}}{Q_{max}} \tag{2.8}$$

The charge ratio is related to the output characteristics. Further discussion of this parameter will be presented in the next section.

The relationship between the electrostatic spring constant and the dynamic activities of the system is

$$k(t) = \begin{cases} k_1 = k_0 + k_{e,max}\ ;\ z(t)\dot{z}(t) < 0 \\ k_2 = k_0 + k_{e,min}\ ;\ z(t)\dot{z}(t) > 0 \end{cases} \tag{2.9}$$

The system becomes a piecewise linear system described by

$$\begin{aligned} m\ddot{z}_1 + b_m \dot{z}_1 + k_1 z_1 &= -m\ddot{y};\ z(t)\dot{z}(t) < 0 \\ m\ddot{z}_2 + b_m \dot{z}_2 + k_2 z_2 &= -m\ddot{y};\ z(t)\dot{z}(t) > 0 \end{aligned} \tag{2.10}$$

where z_1 is the relative displacement between fingers after charging at ends and before discharging at center with $Q = Q_{max}$, z_2 is relative displacement after discharging at center and before charging at ends with $Q = Q_{min}$. In Fig. 2.13, the conditions $z(t)\dot{z}(t) < 0$ and $z(t)\dot{z}(t) > 0$ are satisfied at $z = z_1$ or z_1' and $z = z_2$ or z_2'

respectively. The solutions to Eq. 2.10 are composed of homogeneous solution and particular solution [40],

$$\begin{aligned} z_1 &= e^{-\zeta_1\omega_1 t}\left(C_1\cos\omega_{d1}t + C_2\sin\omega_{d1}t\right) + z_{p1}(t) \\ z_2 &= e^{-\zeta_2\omega_2 t}\left(C_3\cos\omega_{d2}t + C_4\sin\omega_{d2}t\right) + z_{p2}(t) \end{aligned} \tag{2.11}$$

where

$\zeta_1 = \dfrac{b_m}{2m\omega_1}, \zeta_2 = \dfrac{b_m}{2m\omega_2}; \omega_1 = \sqrt{\dfrac{k_1}{m}}, \omega_2 = \sqrt{\dfrac{k_2}{m}}; \omega_{d1} = \omega_1\sqrt{1-\zeta_1^2}, \omega_{d2} = \omega_2\sqrt{1-\zeta_2^2}$;and

z_{p1} and z_{p2} are the particular solutions of the equations as shown below

$$\begin{aligned} z_{p1}(t) &= \frac{Y_0\omega_0^2}{\left(\omega_1^2-\omega_0^2\right)^2 - \left(\dfrac{b_m\omega_0}{m}\right)^2}\left[\left(\omega_1^2-\omega_0^2\right)\sin\omega_0 t - \frac{b_m\omega_0}{m}\cos\omega_0 t\right] \\ z_{p2}(t) &= \frac{Y_0\omega_0^2}{\left(\omega_2^2-\omega_0^2\right)^2 - \left(\dfrac{b_m\omega_0}{m}\right)^2}\left[\left(\omega_2^2-\omega_0^2\right)\sin\omega_0 t - \frac{b_m\omega_0}{m}\cos\omega_0 t\right] \end{aligned} \tag{2.12}$$

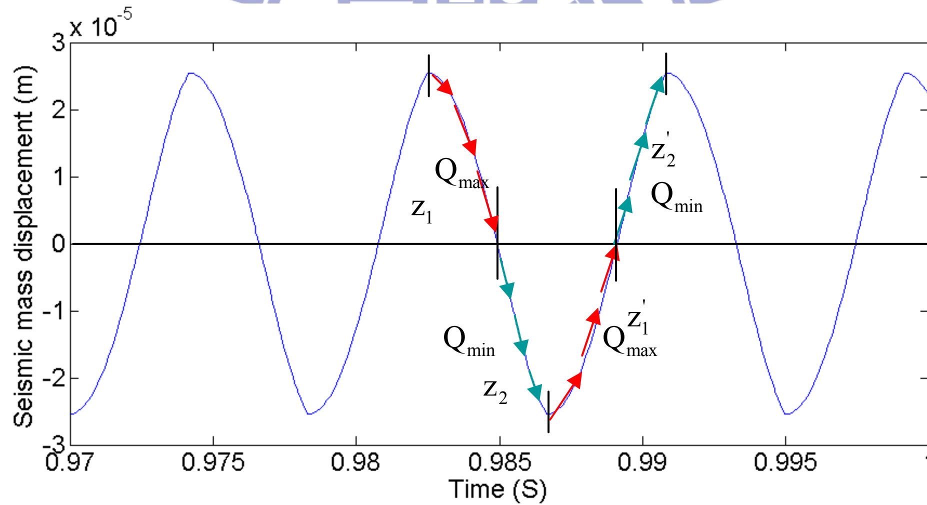

Fig.2.13 Displacement of shuttle mass versus time

Due to the difference in total spring constants, the time needed for the mass to move from ends to center is not equal to the time needed from center to ends. Therefore a parameter α is defined as the portion of time occupied by maximum charge on C_V.

$$\alpha = \frac{t_1}{t_1 + t_2} \tag{2.13}$$

where t_1 and t_2 represent the time occupied by the k_1 and k_2 equations in Eq. 2.10, respectively. During t_1, the charge on C_V is Q_{max}; during t_2, the charge on C_V is Q_{min}.

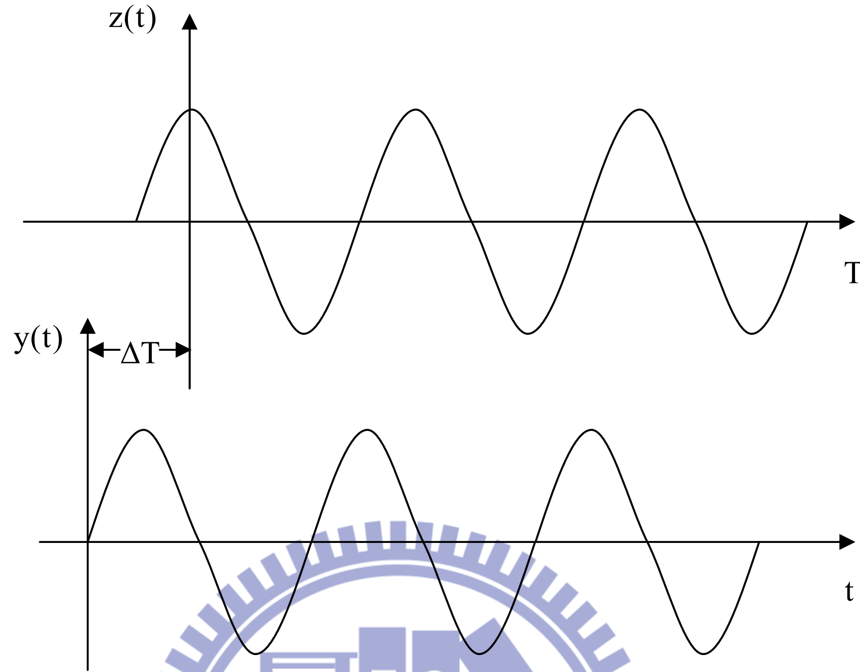

Fig. 2.14 Time shift for t and T scale

ES A 1896

A new time scale is also defined to describe the system behavior. At T = 0, the mass is at the maximum displacement, as shown in Fig. 2.14. The delay between T and t is ΔT. If $T = t - \Delta T$ is substitute into Eq. 2.11, the solution or the displacement function can be rewritten as

$$\begin{aligned} z_1(T) &= e^{-\zeta_1\omega_1(T+\Delta T)}\left(C_1\cos\omega_{d1}(T+\Delta T)+C_2\sin\omega_{d1}(T+\Delta T)\right)+z_{p1}(T+\Delta T) \\ z_2(T) &= e^{-\zeta_2\omega_2(T+\Delta T)}\left(C_3\cos\omega_{d2}(T+\Delta T)+C_4\sin\omega_{d2}(T+\Delta T)\right)+z_{p2}(T+\Delta T) \end{aligned} \tag{2.14}$$

The velocity is the derivative of the displacement functions

$$\begin{aligned} \dot{z}_1(T) &= -\omega_1 e^{-\zeta_1\omega_1(T+\Delta T)}\left[C_1\sin\left(\omega_{d1}(T+\Delta T)+\phi_1\right)-C_2\cos(\omega_{d1}(T+\Delta T)+\phi_1)\right] \\ &\quad +\dot{z}_{p1}(T+\Delta T) \\ \dot{z}_2(T) &= -\omega_2 e^{-\zeta_2\omega_2(T+\Delta T)}\left[C_3\sin\left(\omega_{d2}(T+\Delta T)+\phi_2\right)-C_4\cos(\omega_{d2}(T+\Delta T)+\phi_2)\right] \\ &\quad +\dot{z}_{p2}(T+\Delta T) \end{aligned} \tag{2.15}$$

where $\phi_1 = \tan^{-1}\frac{\zeta_1}{\sqrt{1-\zeta_1^2}}$, $\phi_2 = \tan^{-1}\frac{\zeta_2}{\sqrt{1-\zeta_2^2}}$

The boundary conditions between z_1 and z_2 can be found from the stable oscillating dynamics. At the ends of its travel range indicated in Fig.2.13, the velocity of the moving mass is equal to zero; at the center of travel, the velocity of z_1 and z_2 are continues and the displacement is equal to zero. The next conversion cycle has the same dynamic characteristics; however, the direction is opposite to the previous one. Therefore, there are two conversion cycles in one oscillation cycle. The boundary conditions used in this analysis can be summarized as

$$\dot{z}_1(0) = 0, \tag{2.16a}$$

$$\dot{z}_2\left(\frac{1}{2f}\right) = 0 \tag{2.16b}$$

$$z_1(0) = -z_2\left(\frac{1}{2f}\right) \tag{2.16c}$$

$$\left|z_1(0)\right| = A \tag{2.16d}$$

$$z_1\left(\frac{\alpha}{2f}\right) = 0 \tag{2.16e}$$

$$z_2\left(\frac{\alpha}{2f}\right) = 0 \tag{2.16f}$$

$$\dot{z}_1\left(\frac{\alpha}{2f}\right) = \dot{z}_2\left(\frac{\alpha}{2f}\right) \tag{2.16g}$$

Eqs. 2.16a and b mean the velocity at both ends are equal to zero; Eqs. 2.16c and d show the amplitude equals to A; Eq. 2.16e and f show that the displacement at center is zero; Eq. 2.16g is the continuity of velocity at center. The next conversion cycle has identical behavior as the previous one except for the opposite direction. The boundary conditions are depicted in Fig. 2.15.

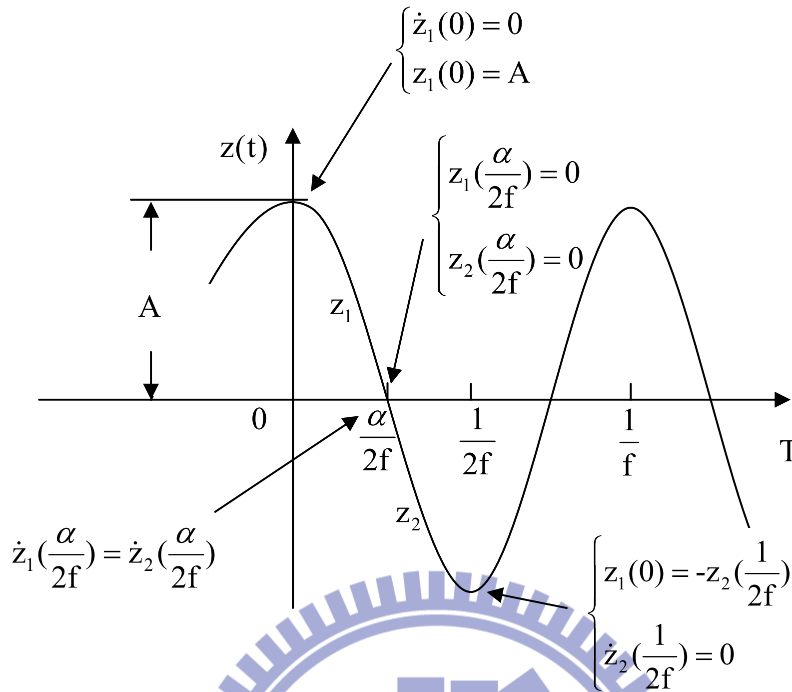

Fig. 2.15 Boundary conditions between z_1 and z_2.

The amplitude A solved from above equations is directly related to $k_{e,max}$. The amplitude A and the initial gap d of the comb fingers are depicted in Fig. 2.16. The capacitance is maximum as the shuttle mass reaches its maximum displacement A. The electrostatic spring constant $k_{e,max}$ is related to A as

$$k_{e,max}=\frac{-Q_{max}^2}{2N\varepsilon_0 L_f hd}=\frac{-C_{max}^2 V_{in}^2}{2N\varepsilon_0 L_f hd}=\frac{-2N\varepsilon_0 L_f hd V_{in}^2}{(d^2-A^2)^2} \tag{2.17}$$

The electrostatic constant $k_{e,min}$ is also a function of amplitude because

$$k_{e,min}=(\frac{Q_{min}}{Q_{max}})^2 k_{e,max}=Q_r^2 k_{e,max} \tag{2.18}$$

Therefore, the parameters related to k_e such as the nature frequencies and damping ratios can also be expressed as functions of the amplitude A. The seven unknowns $C_1, C_2, C_3, C_4, \alpha, \Delta T$, and A can be solved from the seven boundary conditions in Eq.

2.16. Since they are complicated set of nonlinear equations, a MATLAB solver is used to find the numerical solution.

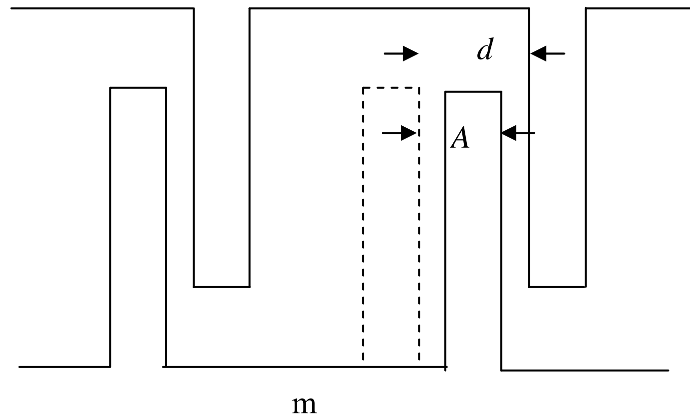

Fig. 2.16 Fingers at maximum displacement

2.3.4 Static analysis

Static analysis can be used to obtain mathematical guidelines for overall system design including layout and circuit. Once the amplitude is decided from the dynamic analysis, parameters such as initial gap and mechanical spring constant can be determined directly. At the output node of the variable capacitor, the charge ratio before and after SW2 is switched and can be expressed as

$$Q_r = \frac{Q_{min}}{Q_{max}} = \frac{C_{min}V_o}{C_{max}V_{min}} = \frac{C_{min}V_o}{C_{min}V_{max}} = \frac{V_o}{V_{max}}, \quad (2.19)$$

where V_{max} and V_o are the capacitor voltage before and after discharge by SW2, as discussed in section 2.2. Assume the storage capacitor C_{stor} is large and the output ripple can be ignored, the charge flow through output load is

$$Q_{out} = \frac{V_o}{2fR_L} \quad (2.20)$$

The charge flow into the variable capacitor is

$$Q_{in} = C_{max}V_{in}(1 - Q_r) \quad (2.21)$$

Because charge conservation, at steady state, $Q_{out} = Q_{in}$ and

$$C_{min}V_{max}(1-Q_r) = \frac{V_o}{2fR_L}$$

$$\Rightarrow C_{min}V_{max} - C_{min}V_o = \frac{V_o}{2fR_L}$$

$$\Rightarrow Q_r = \frac{V_o}{V_{max}} = \frac{C_{min}}{\frac{1}{2fR_L} + C_{min}} = \frac{2fR_L C_{min}}{1+2fR_L C_{min}} \qquad (2.22)$$

Eq. 2.22 can be rearranged to the following form

$$R_L = \frac{Q_r}{2fC_{min}(1-Q_r)} \qquad (2.23)$$

From Eq. 2.22, we know that the charge ratio is determined by the frequency of vibration, the minimum capacitance and the output load. If the voltage ripple of C_{stor} needs to be considered, the charge ratio is

$$Q_r = \frac{C_{min}}{C_{stor}\left(1-e^{\frac{-1}{2fR_L C_{stor}}}\right)+C_{min}} \qquad (2.24)$$

The approximation of Eq. 2.24 for large C_{stor} is the same as Eq. 2.22.

The output power can also be determined as we know the amplitude of the shuttle mass displacement. For large C_{stor}, the output power is

$$P_{out} = \frac{V_o^2}{R_L} \qquad (2.25)$$

Output power can also be expressed in following form from Eq. 2.22 and Eq. 2.23

$$P_{out} = 2fC_{min}V_{max}^2 Q_r(1-Q_r) \qquad (2.26)$$

It is worthy to mention that an optimum load based on a similar system analysis was derived in [41] by finding the derivative of output power with respect to the output load. The optimal load is [41]

$$R_{L,opt} = \frac{1}{2fC_{min}} \qquad (2.27)$$

However; the result in Eq. 2.27 was based on an assumption of fixed amplitude. The same result can also be derived by finding the derivative of output power respect to

charge ratio in Eq. 2.26 if we regard other parameters as constants. The maximum output power occurred at $Q_r = 0.5$. As we substitute $Q_r = 0.5$ into Eq. 2.23, we can obtain an identical result as Eq. 2.27.

However; in this research, the charge ratio is related to the electrostatic force and thus the amplitude. Therefore, we should not assume a fixed amplitude arbitrarily. The assumption ignored the electromechanical coupling effect in the mass-spring-damper system. We treat Q_r as an operation parameter instead of a constant.

2.4 Optimizing process

Because Eqs. 2.16 are highly nonlinear, we use “fsolve” in Matlab to find numerical solution. The “fsolve” solver needs an initial guess to find the solution of the set of equations. At low amplitude, the system can be regarded as linear. The starting guess was therefore found by the approximated linear results. For the next calculation the previous solution was used as new starting guess. After repeating these steps, the maximum amplitude can be found.

The dimensions of the device are partially fixed as shown in Table 2.1. Four free parameters are used to find the optimal condition under restricted area, as listed in Table 2.2. The detailed optimization flow chart is shown in Fig. 2.17.

Table 2.1 Fixed parameters of optimizing process

Parameter	**Description of constants**	**Value**
h	Device thickness	200μm
t	Finger width	10μm
L_f	Finger overlap length	400μm

Table 2.2 Free parameters of optimizing process

Variable	Description of variables	Range
k_0	Mechanical spring constant	1~3000N/m
Q_r	Charge ratio	0.1~0.9
S_r	Surface ratio	0.05~0.95
d	Initial gap	1μm~70μm

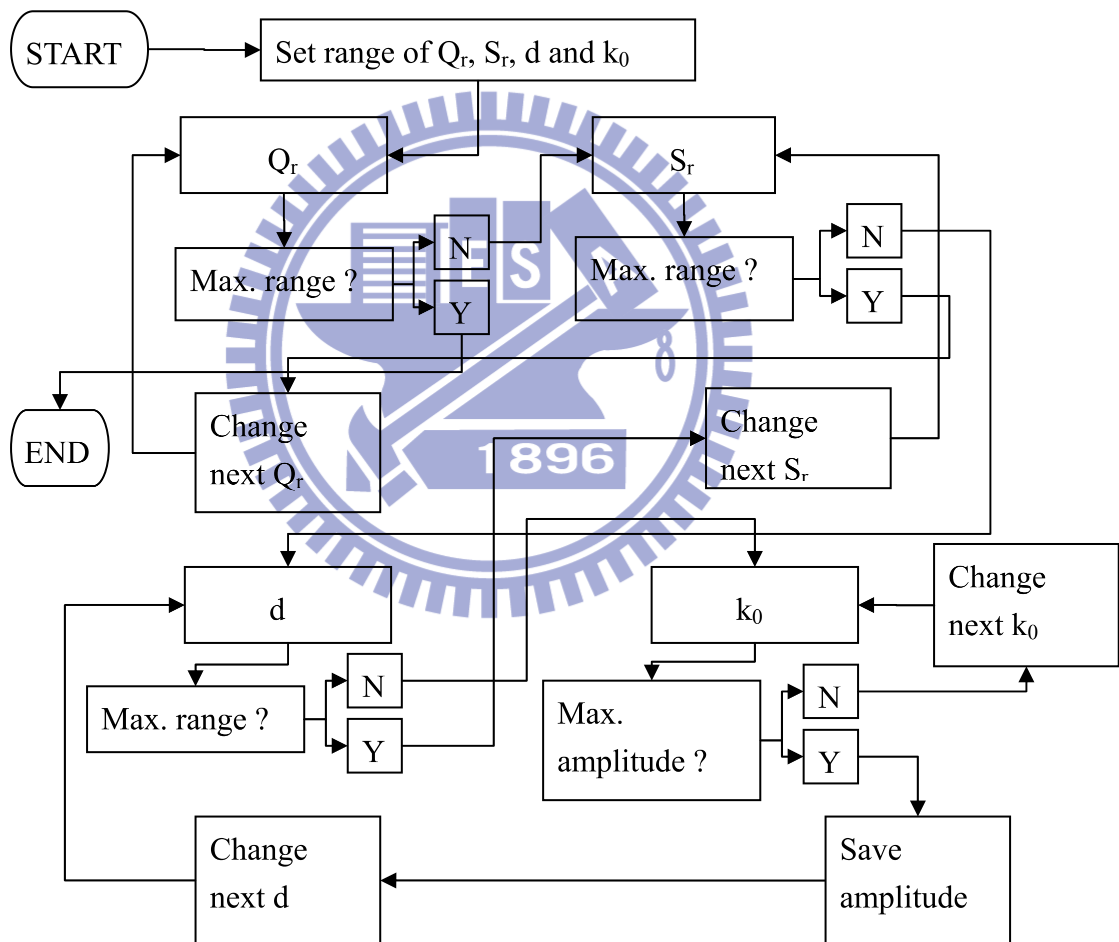

Fig. 2.17 Optimization flow chart

The oscillation amplitude A was calculated by the "fsolve" solver for each set of free parameter values in the ranges in Table 2.2. For example, Fig.2.18 shows the calculation results for the initial gap of 40 μm, charge ratio of 0.5 and area ratio of 0.8 as a function of k_0. At $k_0 = 2392 N/m$ the amplitude reaches the maximum of 39.35 μm. The corresponding output power is 45.8μW and output voltage is 68.62V.

Similar results can also be obtained in frequency domain. Fig.2.19 shows the amplitude and power versus frequency for k_0=2392N/m, which corresponds to the maximum power in Fig 2.18.

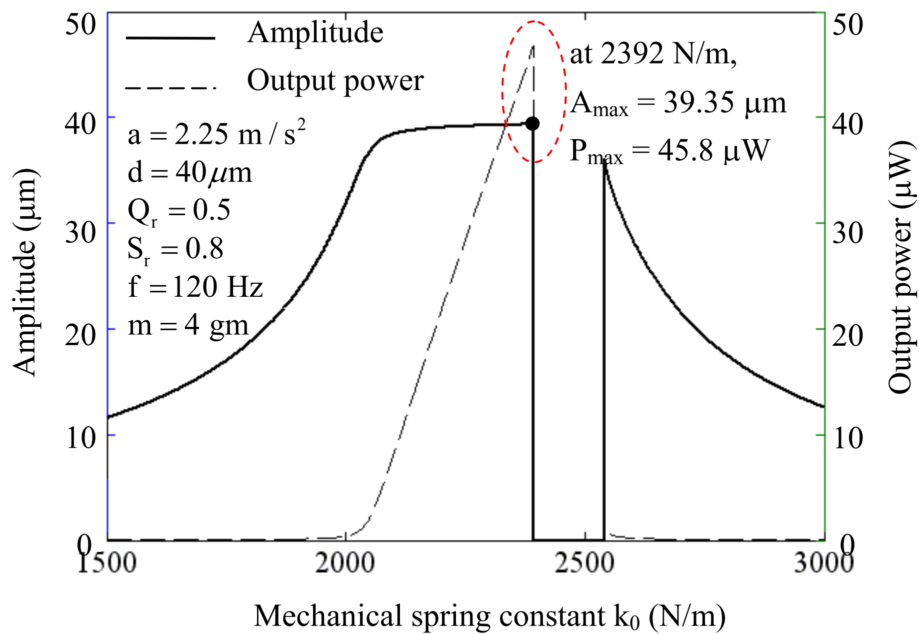

Fig 2.18 Amplitude and power vs. spring constant

It is interesting to notice that there is a range of design or operation parameters where no solution of the oscillation amplitude A exists in Figs. 2.18 and 2.19. This phenomenon is discussed in the next section from an energy point of view.

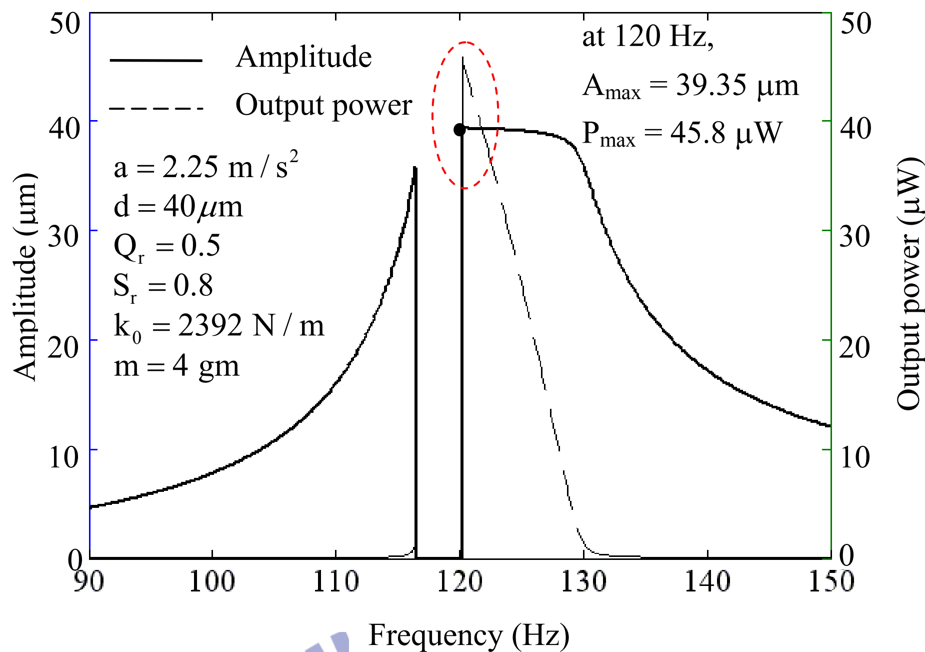

Fig. 2.19 Amplitude and power vs. Frequency

2.4.1 Conditions for normal oscillation discussion

At maximum displacement, the energy in the system is the sum of the mechanical spring potential energy and the capacitor electrostatic energy. The capacitor energy increases after charging by the battery. At center, the system energy is the sum of the kinetic energy and the capacitor energy. The capacitor energy decreases after discharging to the load. The system energy at different instances and positions is listed in Table 2.3. Fig. 2.20 shows these calculated system energies at different frequencies. The interaction between the external force and the restoring force in the system cause two conditions for which the energy can not be balanced and no normal oscillation can be found, as discussed next.

Table 2.3 System Energy at different instances and positions

Position	**At center before discharging**	**At center after discharging**	**At ends before charging**	**At ends after charging**
Kinetic energy	$\frac{1}{2}m\dot{z}^2$	$\frac{1}{2}m\dot{z}^2$	0	0
Spring energy	0	0	$\frac{1}{2}k_0A^2$	$\frac{1}{2}k_0A^2$
Capacitor energy	$\frac{Q_{max}^2}{2C_{max}}$	$\frac{Q_{min}^2}{2C_{max}}$	$\frac{Q_{min}^2}{2C_{min}}$	$\frac{Q_{max}^2}{2C_{max}}$

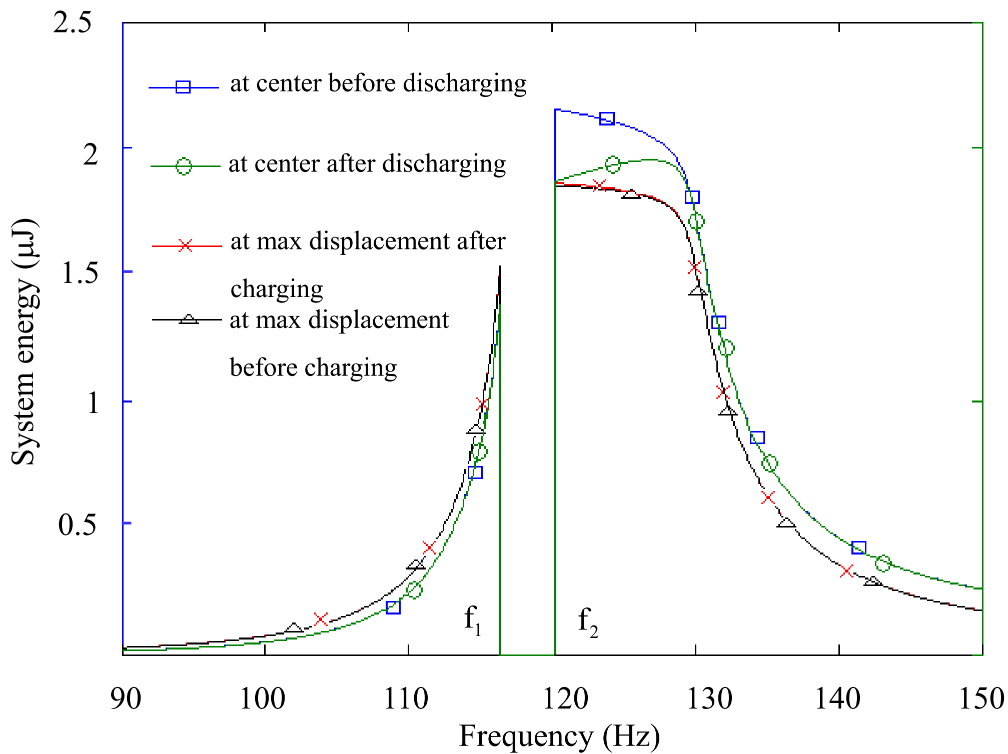

Fig. 2.20 System energy versus driven frequency

In Fig 2.20, we can see the energy at center after discharging crosses the energy at ends after charging at 120Hz. As the system approaches resonance at f_2, the output reaches maximum and the energy left in the system after discharging at center becomes insufficient for the mass to move to maximum displacement. Similar observation can be found at f_1. As the system approaches the frequency at f_1 the energy stored in the system after charging at maximum displacement becomes too large for

the mass to maintain stable operation.

2. 4 .2 Optimum design

The output voltage is limited to 40V for further integration with power management circuits. The calculated power can be plotted versus area ratio S_r and initial gap d for each charge ratio Q_r as shown in Fig. 2.21 and Fig. 2.22 for devices with and without attached external mass, respectively. From Eqs. 2.23 and 2.26, we know that a larger surface ratio has benefits of lower load resistance and higher output power. For the device with attached mass, the robustness of the devices and the area reserved for mass attachment must be considered. Therefore, a maximum value of surface ratio of 0.8 is chosen in our consideration. For the device without attached mass, it is simpler and there is no such restriction.

The optimal design under 40V output voltage is obtained from Fig. 2.21 and Fig. 2.22. The parameters used in this design are optimized for maximum power and the results are summarized in Table 2.4 and Table 2.5. The optimum design with external mass attachment can generate 40.53μW. In the case without external mass attachment, 0.87μW can be generated.

Since the battery provides the initial charge for the energy conversion, the net output power is slightly less than the values calculated above. Because the current that flows into the variable capacitor from the battery is equal to the current that flows out the variable capacitor to the load, the percentage of net power generation is about 91%, as calculated in Eq. 2.29.

$$\frac{P_{out}}{P_{in}} = \frac{I_{out}V_{out}}{I_{in}V_{in}} = \frac{V_{out}}{V_{in}} \tag{2.28}$$

$$\%P_{net} = 1 - \frac{P_{in}}{P_{out}} = 91\% \tag{2.29}$$

We can notice that in the device with the external mass, the output power is less dependent on the area ratio because the difference of silicon mass caused by the area ratio is minor compared to the external mass. On the other hand, in the device without external mass, the output power is related to both area ratio and initial gap. An obvious trend is the less the area ratio is, the higher output power is.

With external mass attached

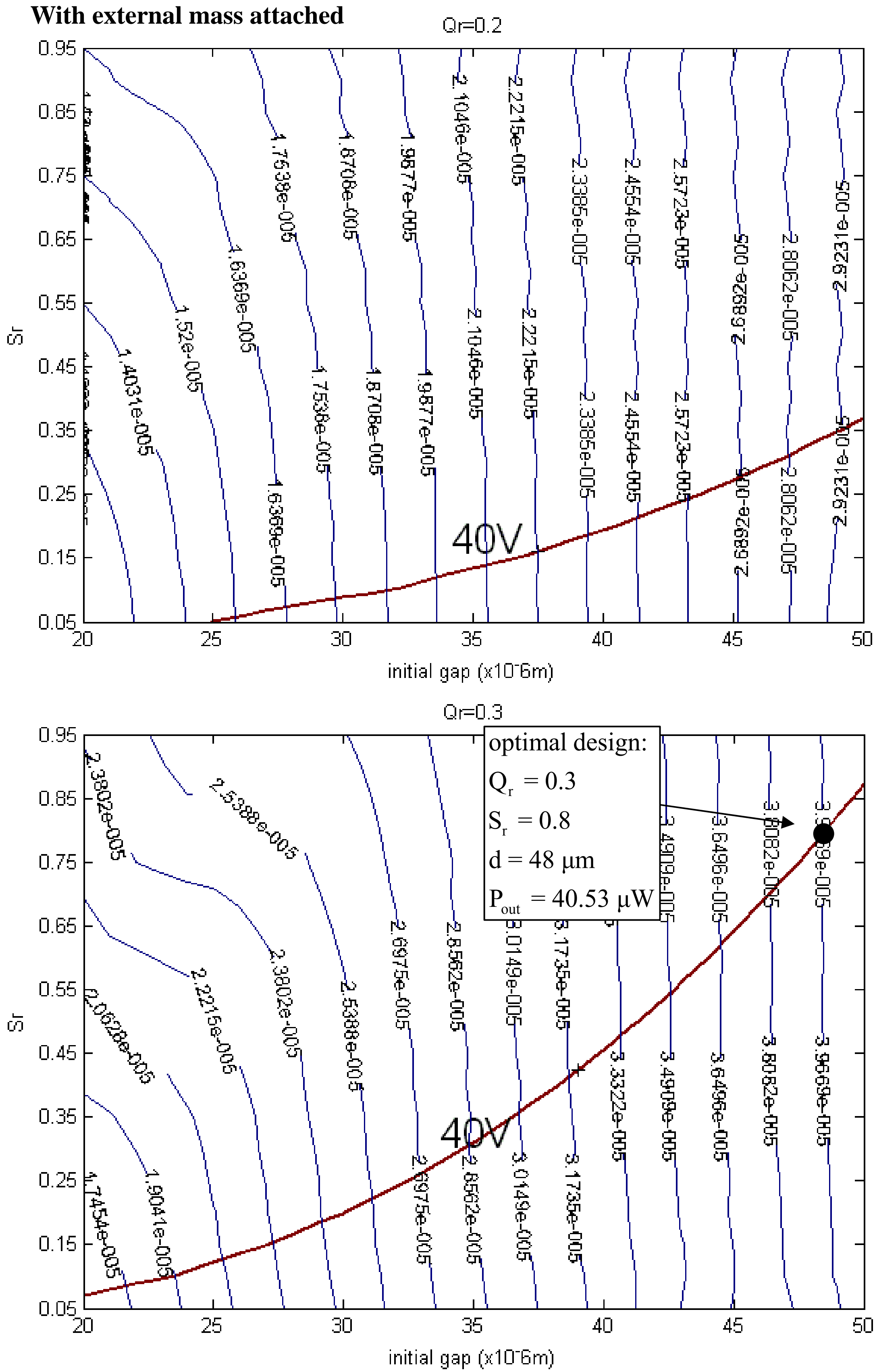

Fig. 2.21 Contour of output power and voltage with external mass attachment for various Q_r

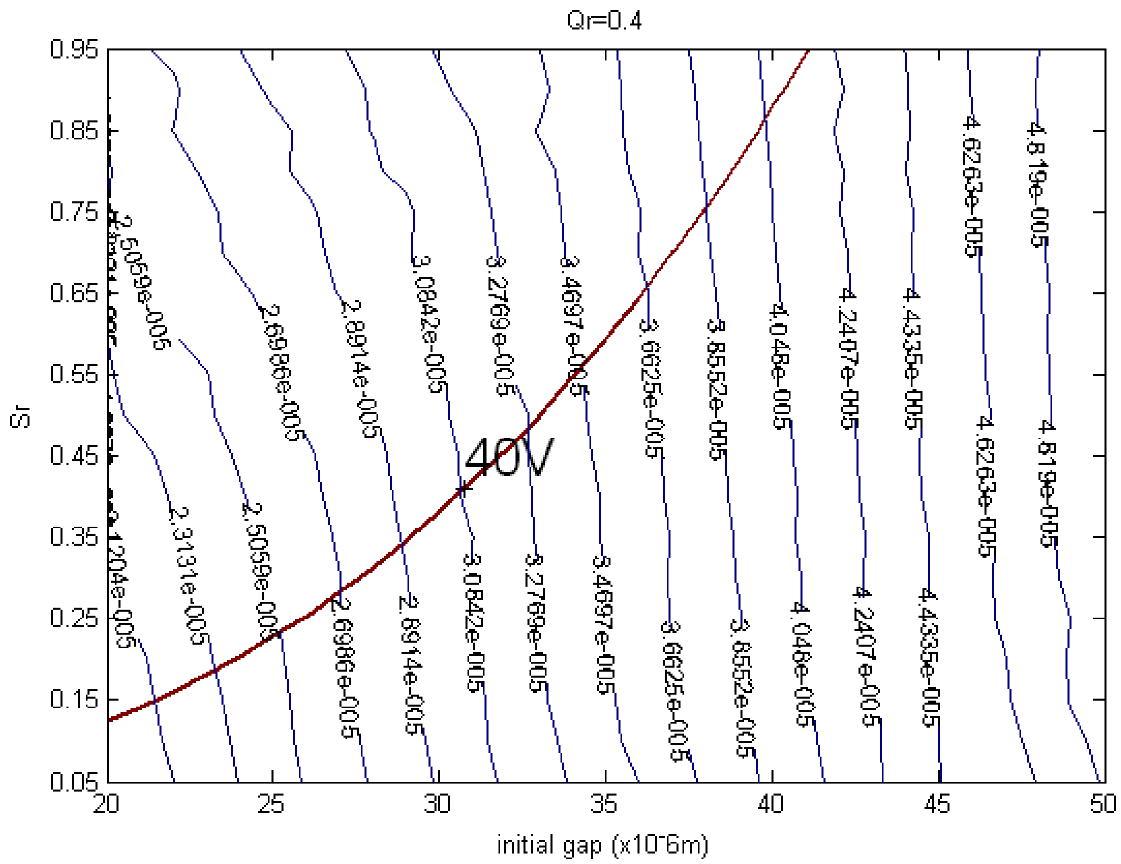

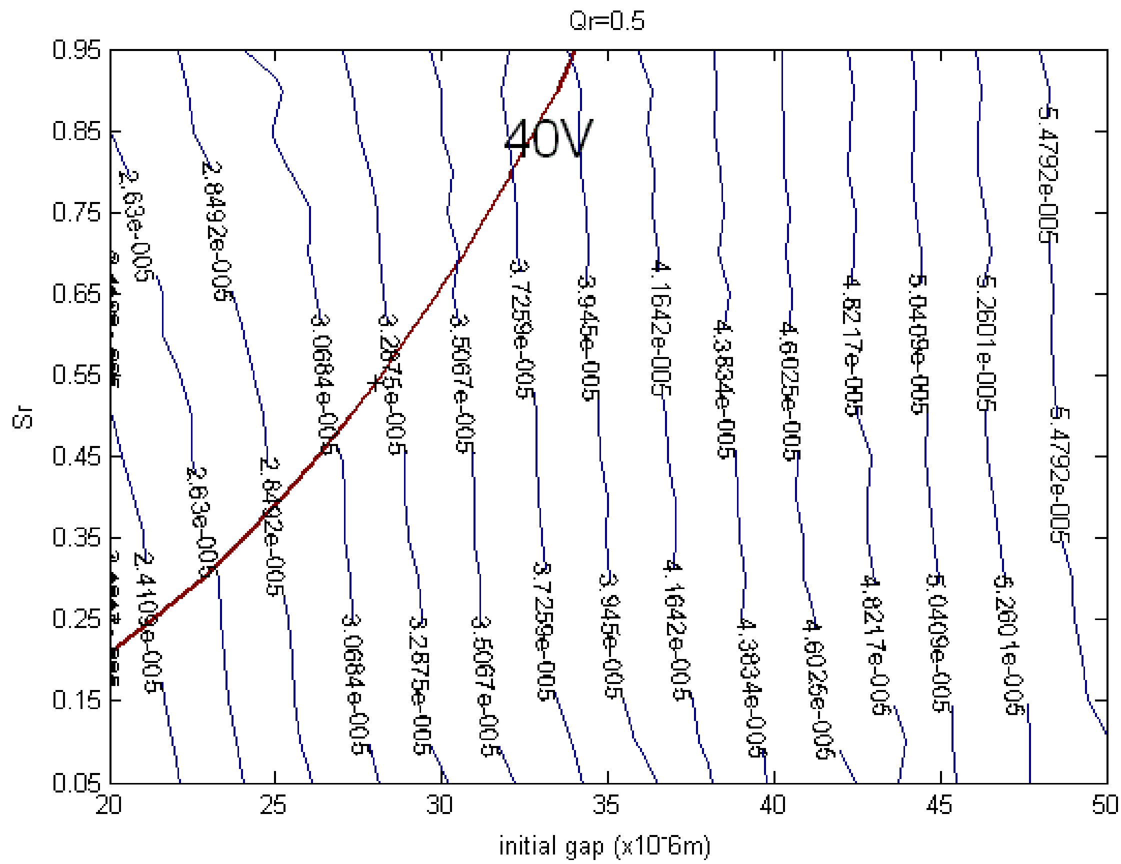

Fig. 2.21 Contour of output power and voltage with external mass attachment for various Q_r (continued)

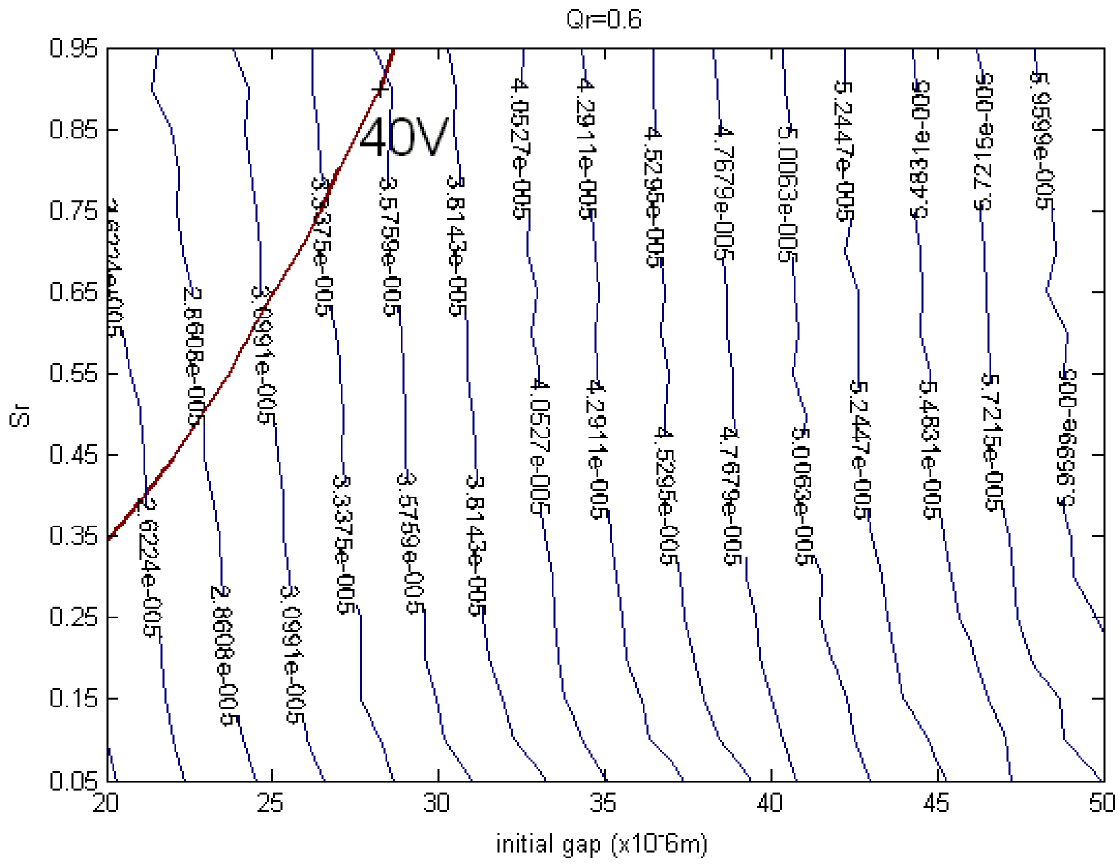

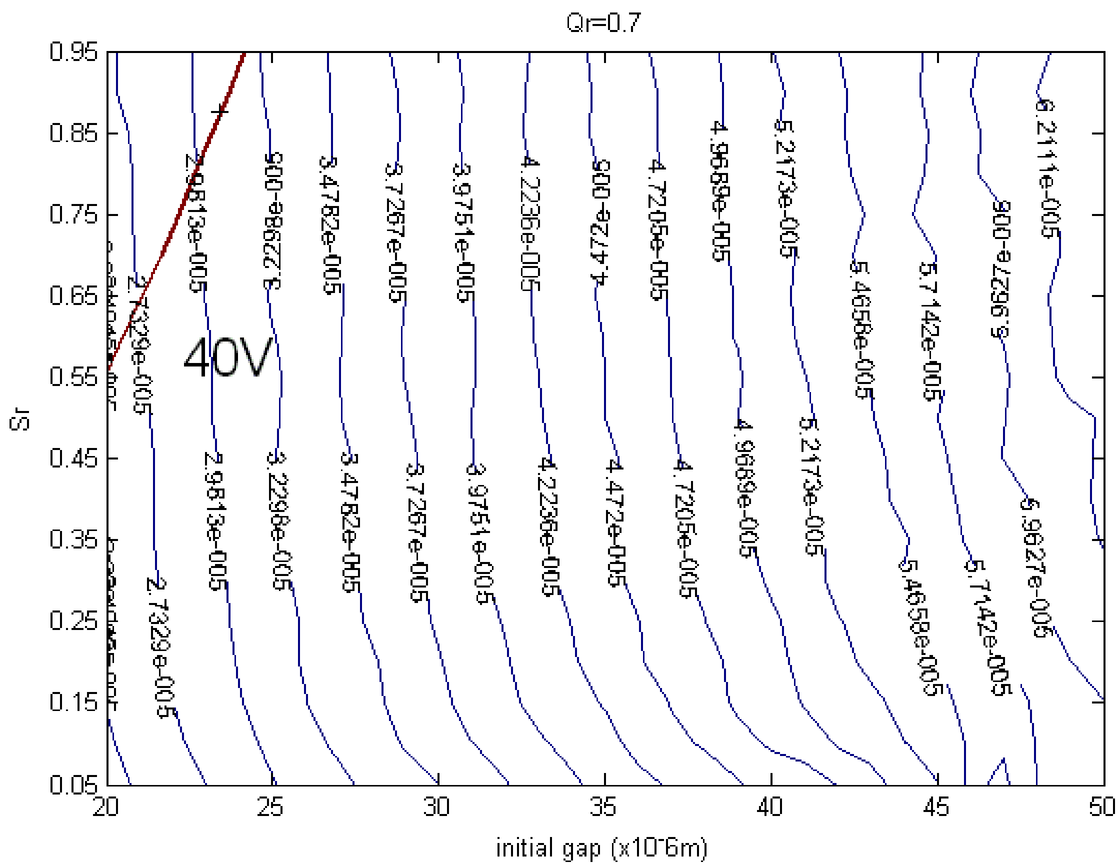

Fig. 2.21 Contour of output power and voltage with external mass attachment for various Q_r (continued)

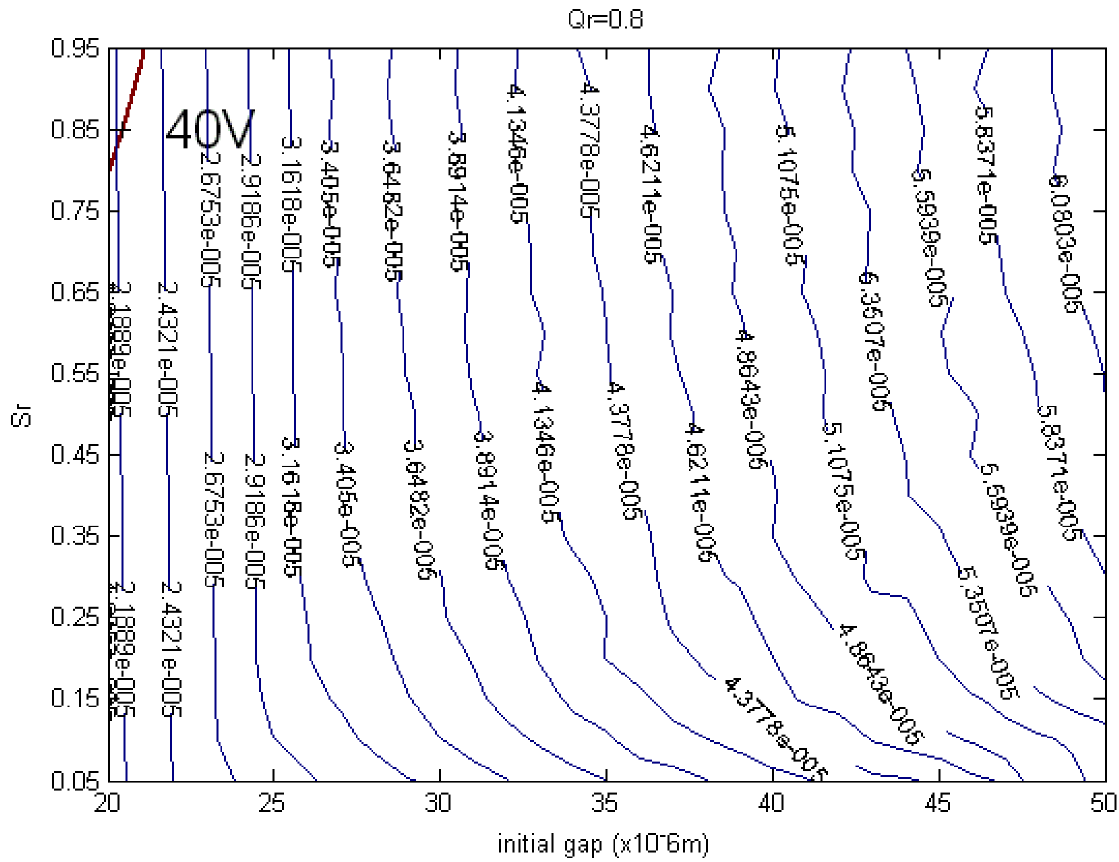

Fig. 2.21 Contour of output power and voltage with external mass attachment for various Q_r (continued)

Table 2.4 Variable capacitor design parameters (with external mass)

Variable	Description of variables	Designed value
h	Device thickness	200 μm
N_g	Number of variable capacitor cells	1539
W_f	Finger width	10 μm
L_f	Finger overlap length	400 μm
d	Finger initial gap	48 μm
Z_{max}	Maximum displacement	47.34 μm
Qr	Charge ratio	0.3
C_{max}	Maximum value of capacitance	1663.5 pF

C_{min}	Minimum value of capacitance	45.4 pF
k	Mechanical spring const.	2305 μN/μm
m	Mass of movable plate	4.03g
R_L	Driven load resistance	39.3MΩ
C_{stor}	Output temporary storage capacitor	10.6 nF
V_{out}	Output voltage (steady state)	40 V
P_{out}	Output power (steady state)	40.53 μW

Without external mass attached

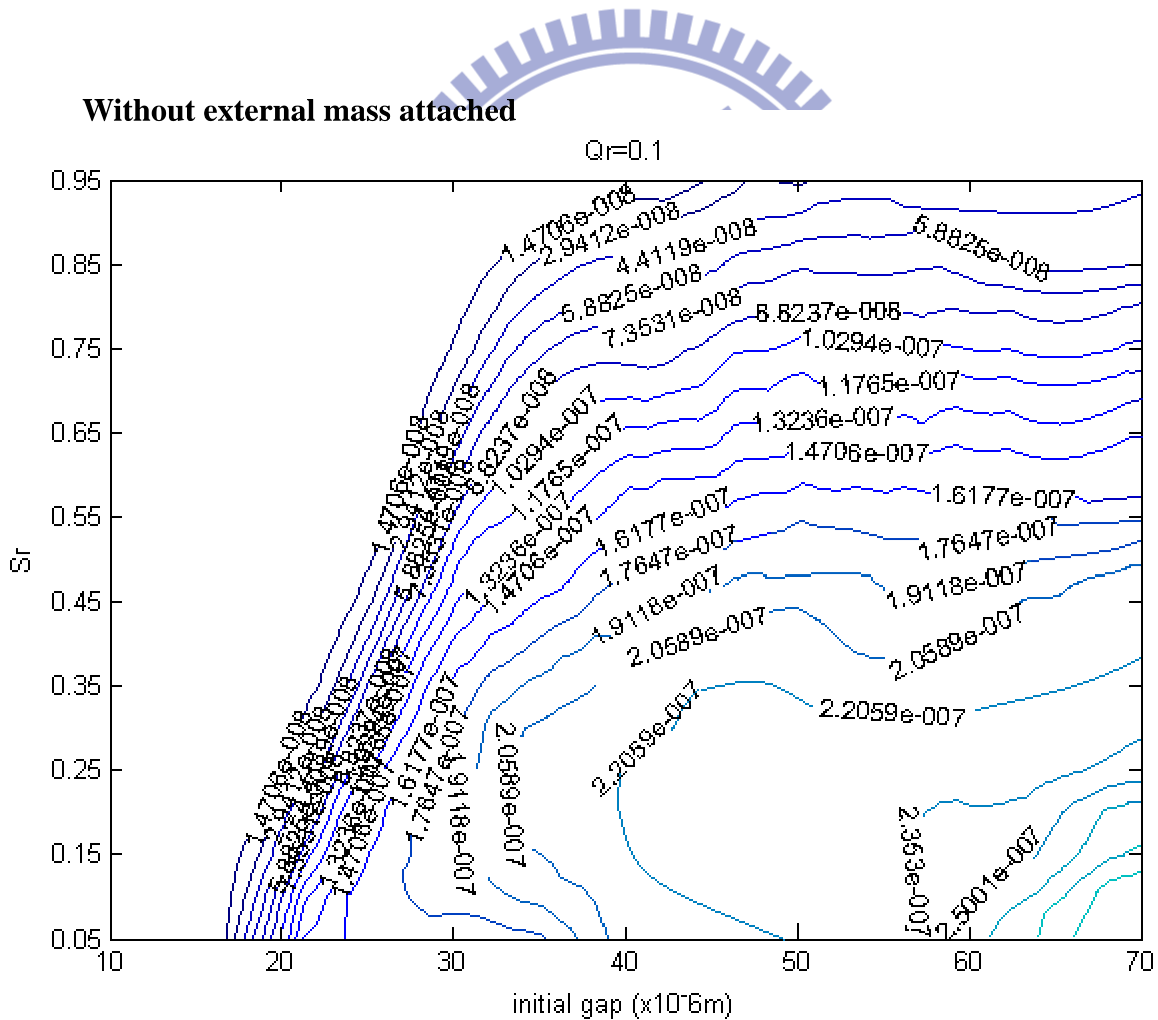

Fig. 2.22 Contour of output power and voltage without external mass for various Q_r(continued)

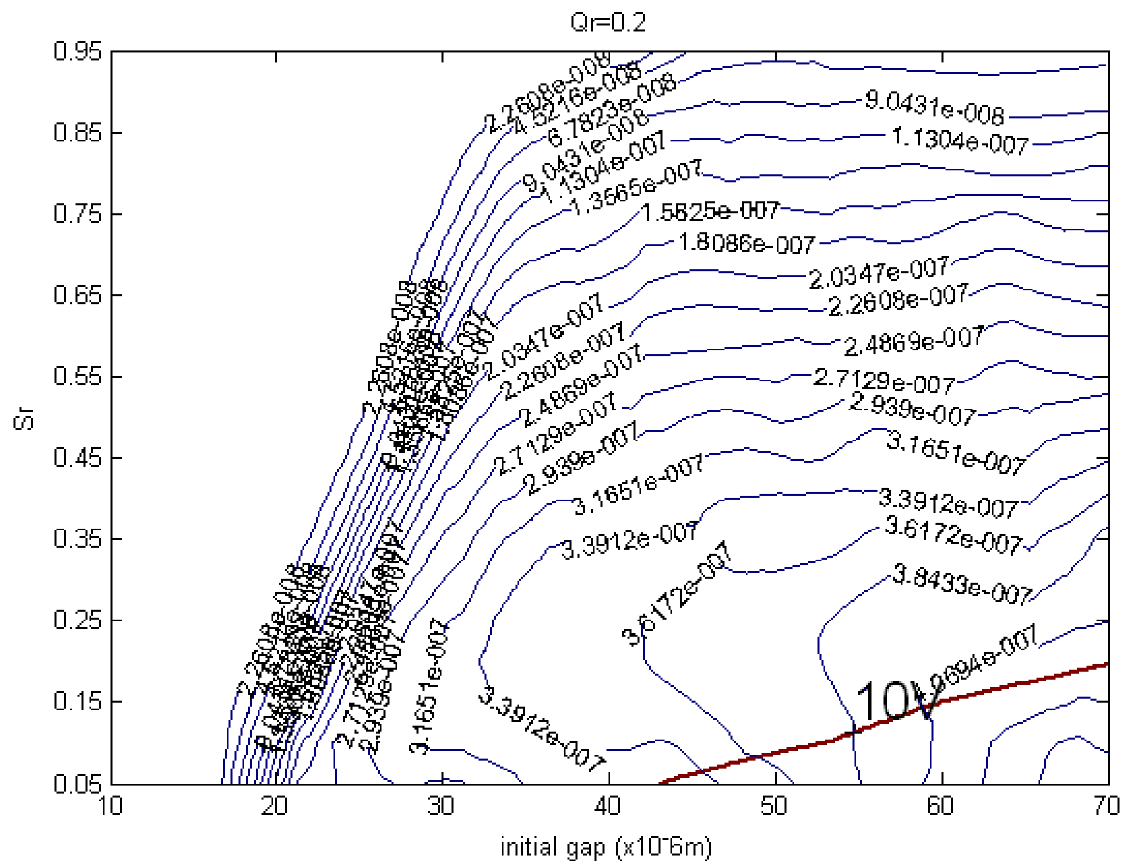

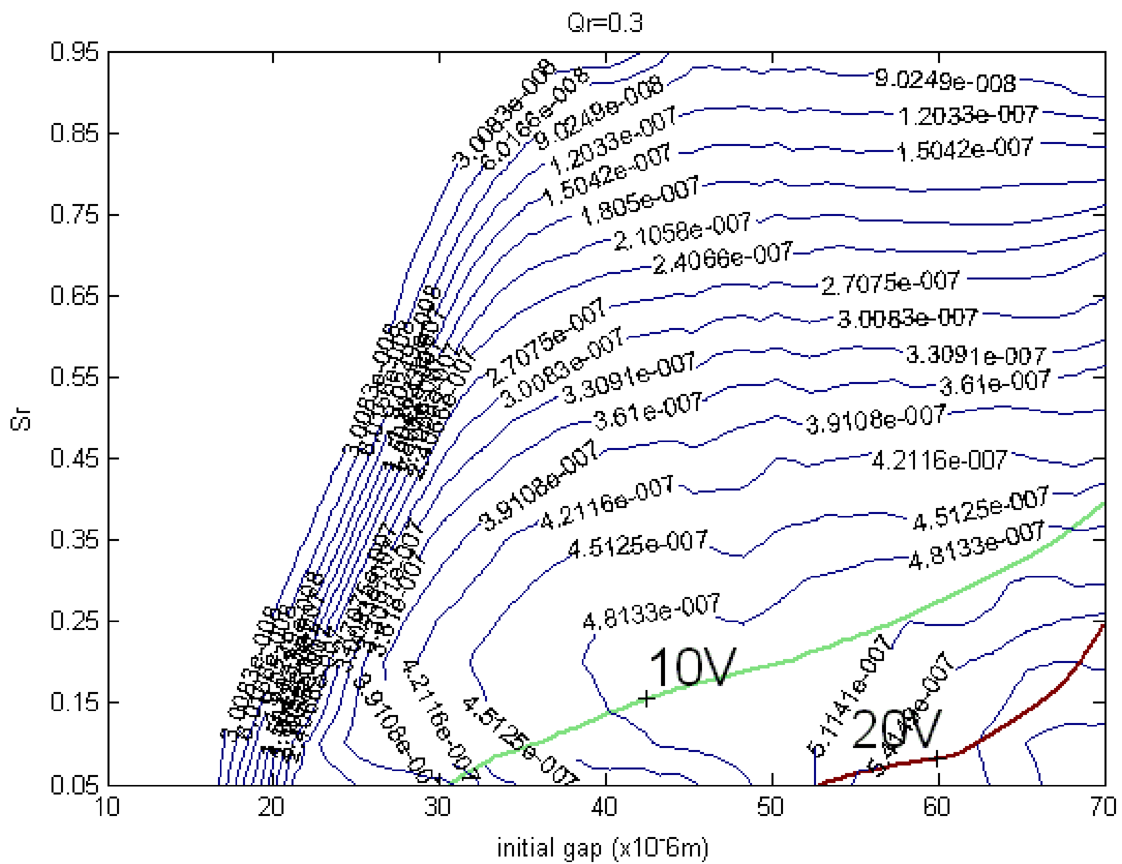

Fig. 2.22 Contour of output power and voltage with ball attachment for various Q_r (continued)

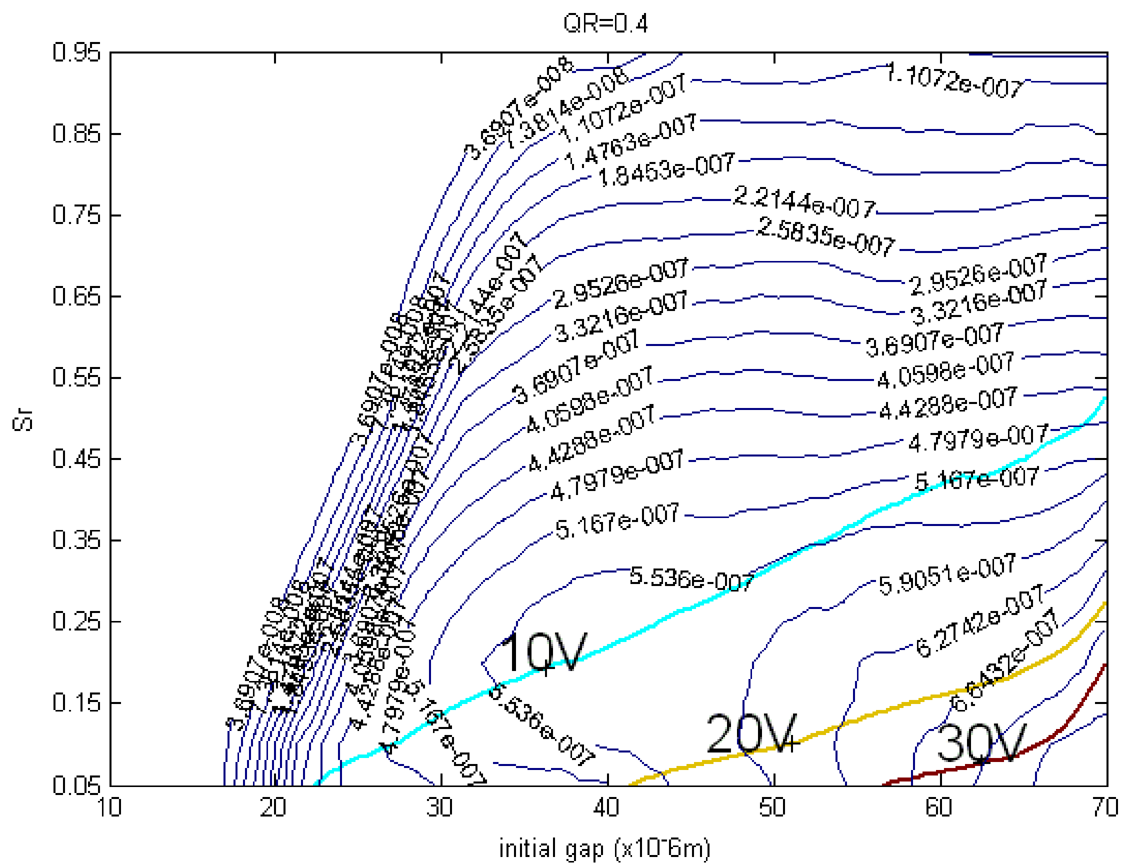

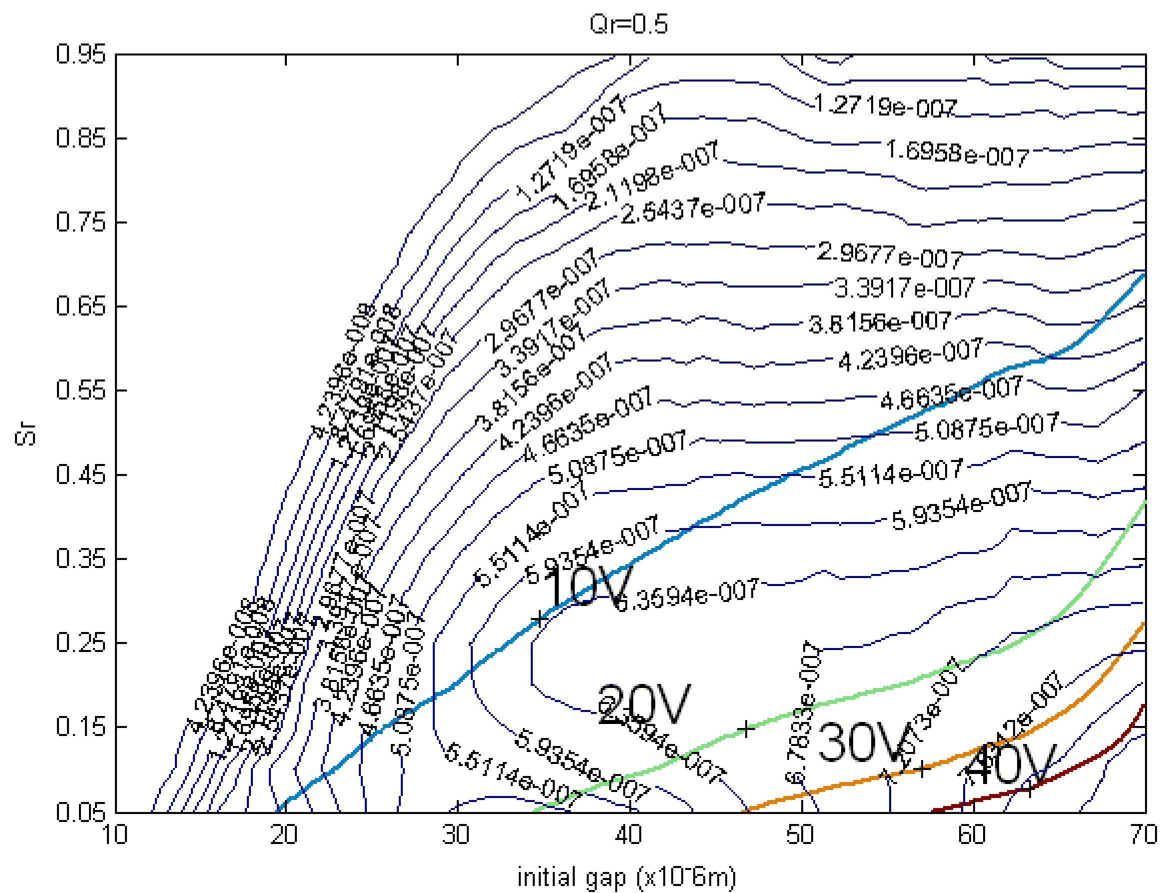

Fig. 2.22 Contour of output power and voltage with ball attachment for various Q_r

(continued)

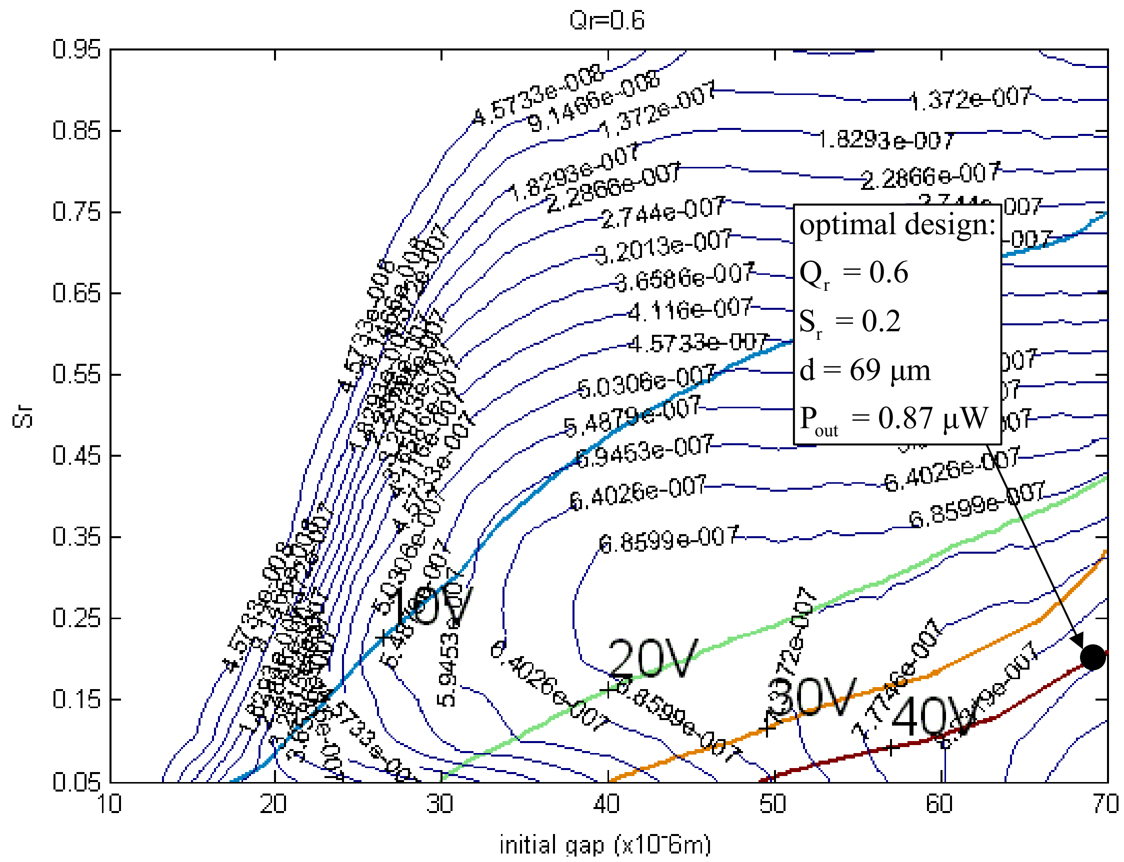

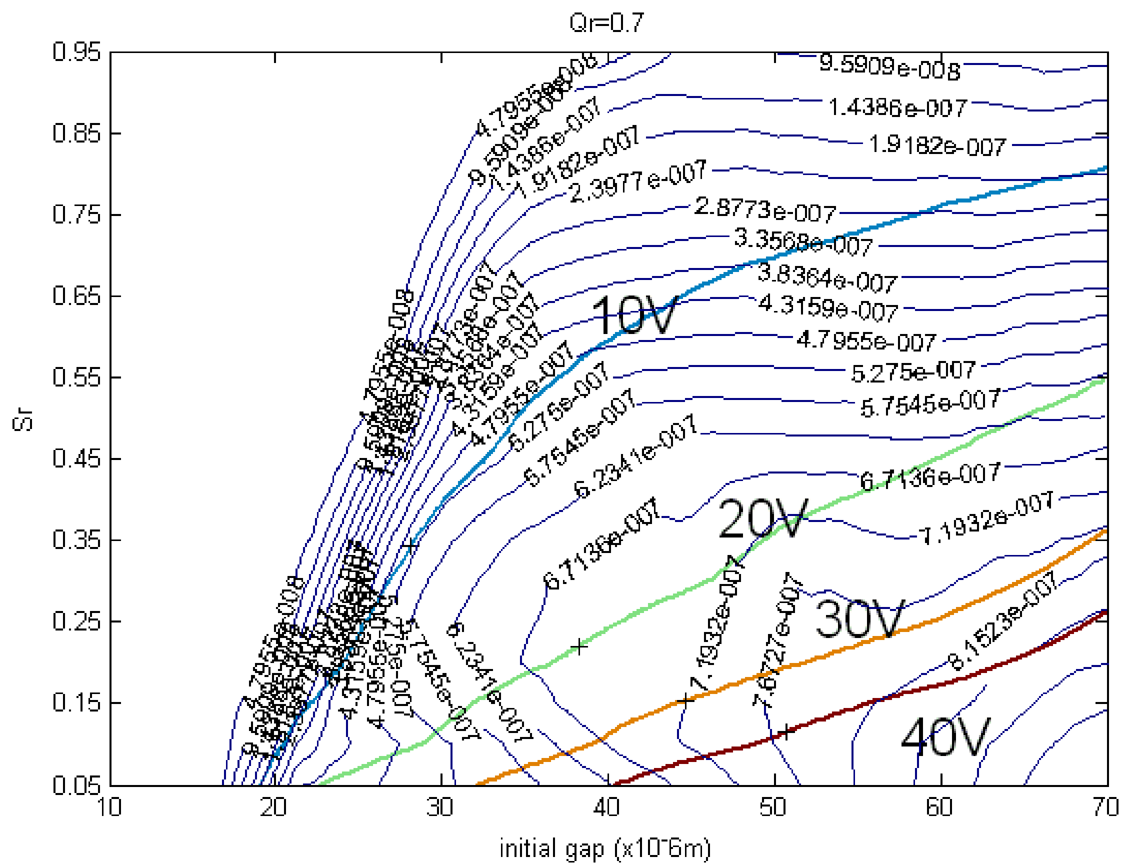

Fig. 2.22 Contour of output power and voltage with ball attachment for various Q_r (continued)

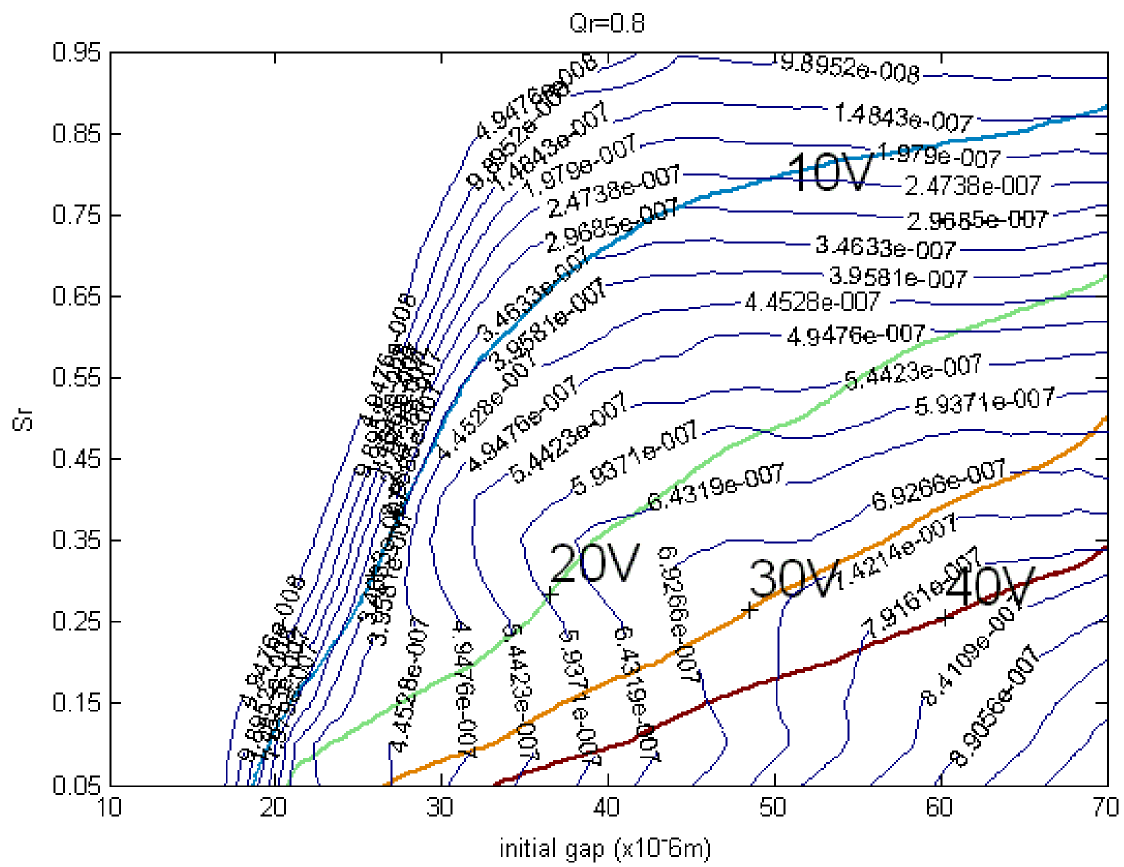

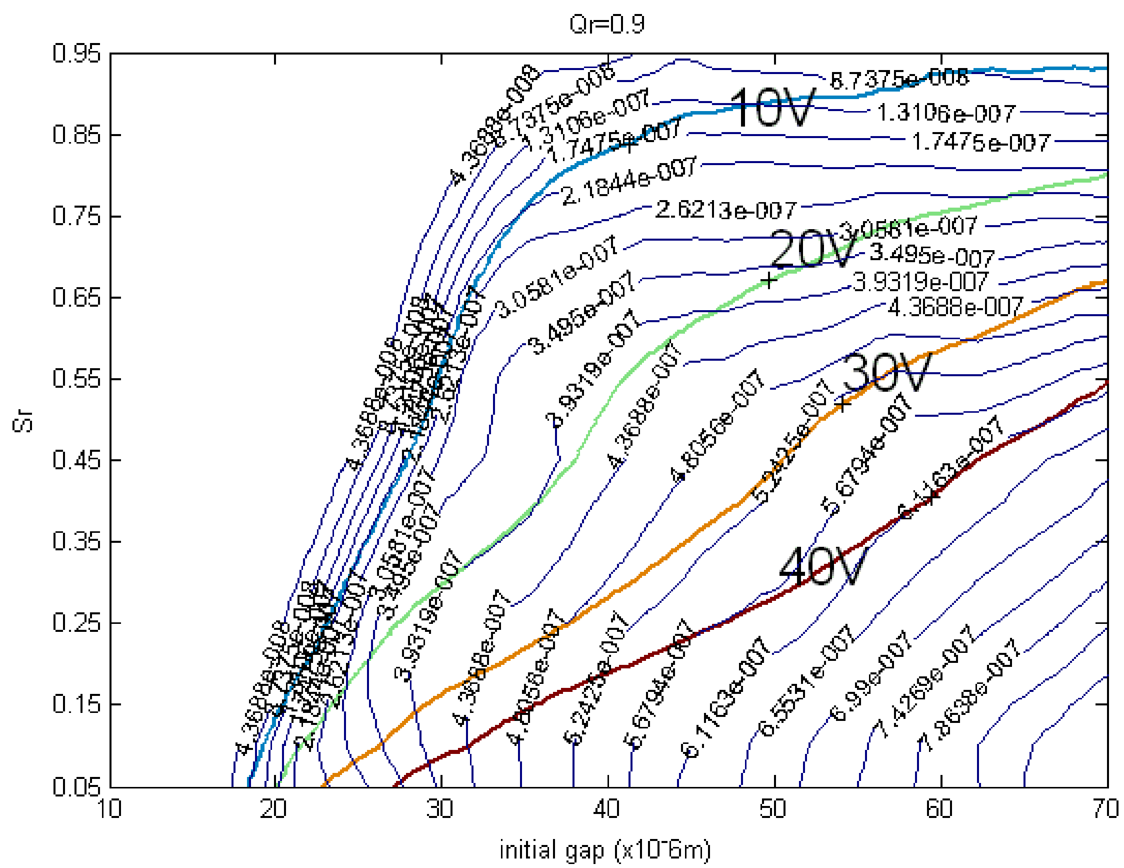

Fig. 2.22 Contour of output power and voltage with ball attachment for various Q_r(continued)

Table 2.5 Variable capacitor design parameters (without external mass)

Variable	**Description of variables**	**Designed value**
h	Device thickness	200 μm
N_g	Number of variable capacitor cells	162
W_f	Finger width	10 μm
L_f	Finger overlap length	400 μm
d	Finger initial gap	69 μm
Z_{max}	Maximum displacement	67.15 μm
Qr	Charge ratio	0.6
Sr	Surface ratio	0.2
C_{max}	Maximum value of capacitance	62.8 pF
C_{min}	Minimum value of capacitance	3.32 pF
k	Mechanical spring const.	23.9 μN/μm
m	Mass of movable plate	41.36mg
R_L	Driven load resistance	1879.8 MΩ
C_{stor}	Output temporary storage capacitor	22.16 nF
V_{out}	Output voltage (steady state)	40 V
P_{out}	Output power (steady state)	0.87 μW

2.5 Previous design

To solve the previous encountered process issues, we used the previous layout design to test the modified fabrication process. The layout of the previous design is shown in Fig. 2.23. It was designed by Simulink instead of the new modeling method. The mechanical structure was designed to generate an output power of 31 μW. An external mass of 4 grams was put on the central hole to adjust the device resonance to match the input vibration. Two integrated mechanical switches, SW1 and SW2, were used to provide accurate charge-discharge energy conversion timing. Detailed parameter was listed in Table 2.6

Table 2.6 Design parameter for previous device

Variable	Description of variables	Designed value
h	Device thickness	200 μm
W_f	Finger width	10 μm
L_f	Finger overlap length	400 μm
d	Finger initial gap	26 μm
Qr	Charge ratio	0.42
Sr	Surface ratio	0.345
C_{max}	Maximum value of capacitance	1570 pF
C_{min}	Minimum value of capacitance	62 pF
k	Mechanical spring const.	2425 μN/μm
m	Mass of movable plate	4 g
R_L	Driven load resistance	50 MΩ
C_{stor}	Output temporary storage capacitor	5 nF

V_{out}	Output voltage (steady state)	40 V
P_{out}	Output power (steady state)	31 μW

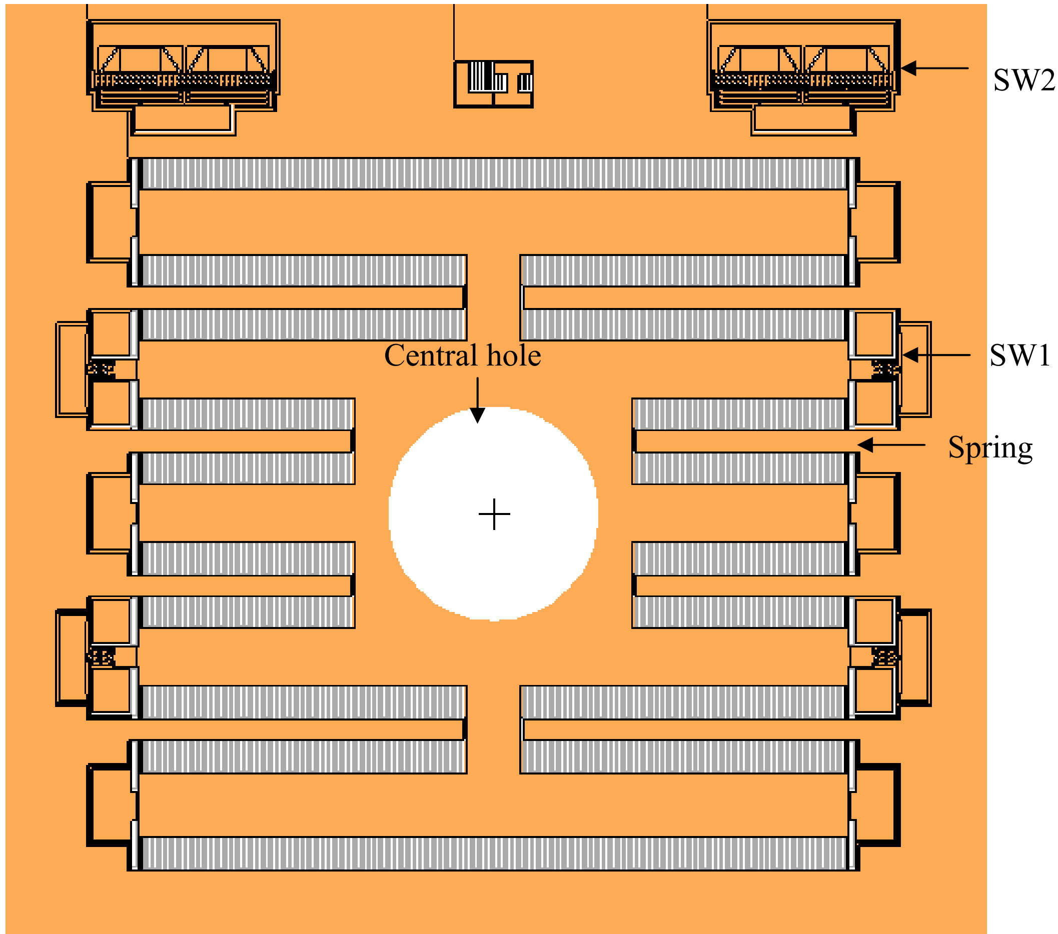

Fig. 2.23 Layout view of the previous device

2.6 Summary

The design and analysis of a vibration-to-electric energy converter with and without external mass attached on the device is presented in this chapter. For the 3.6 V supply voltage and 1cm^2 chip mass area constraint, this device can be designed to generate 40.53 μW and 0.87 μW for the input vibration with frequency of 120 Hz.

Chapter 3 Fabrication Process

Detailed fabrication process flows and process issues encountered in the SOI based devices are presented in this chapter. The first section of this chapter shows the processes based on SOI wafers. The processes include wafer cleaning, photolithography, deep reactive ion etching, structure releasing, and metal deposition. The second part discusses the process issues which were encountered in the experiments. The problems were solved and devices were successfully fabricated.

3.1 Fabrication process flow

As mentioned in Chapter 2, the high aspect ratio MEMS comb finger structures serve the variable capacitor to convert energy. The structure is fabricated by the deep reactive ion etching technology. Inductively Couple Plasma (ICP) etching is used in our case. The comb fingers attached to the moving plate are the moving electrodes of the variable capacitor. The fingers on outer frame serve as the fixed electrodes of the variable capacitor.

To obtain the maximum output power, the device thickness should be as large as possible. However, it is limited by the ICP fabrication capability to define the finger structure. The resistive loss was reduced by using a highly conductive device layer with a resistivity less than 0.02 Ω-cm. The buried oxide layer is 2 μm. The handle layer is 400 μm for a firm structural support.

Most of the fabrication was conducted in the Nano Facility Center at National Chiao Tung University. The fabrication process is illustrated in Fig. 3.1 and the detail of the parameters in every process step is presented in the following sections.

Step 1: Wafer cleaning

RCA cleaning is an industrial standard process for removing contaminants from wafers. It should be performed before high temperature processing steps to minimize defects in following processes. The procedure has three major steps in sequence:

A. Organic Clean: Removal of insoluble organic contaminants

B. Oxide Strip: Removal of the thin silicon dioxide layer.

C. Ionic Clean: Removal of ionic and heavy metal atomic contaminants.

The SOI wafer is first cleaned with the following parameters and steps, as shown in Fig. 3.1(a). Every step begins and ends with 5 minute de-ionized water (DI water) rinse.

Step	Process parameters	Function
1	H_2SO_4 : H_2O_2 = 3 : 1 (10 min 85 °C)	Organic removal
2	HF : H_2O = 1 :100 (room temperature 30 seconds)	Chemical oxide removal
3	NH_4OH : H_2O_2 : H_2O = 1 : 4 : 20 (10 min 85 °C)	Particle removal
4	HCl : H_2O_2 : H_2O = 1 : 1 : 6 (10 min 85 °C)	Ion removal
5	HF : H_2O = 1 :100 (room temperature 30 seconds)	Chemical oxide removal

Step 2: Silicon oxide deposition on the backside

Silicon oxide was deposited by a BR-2000LL plasma enhanced chemical vapor deposition (PECVD) system on the back side of the SOI handle wafer, as shown in Fig. 3.1(b). The silicon oxide serves as the hard mask for the following backside ICP etching process due to the relatively superior heat dissipation in the ICP etching process.

A 4.5-μm-thick silicon oxide is required according to the selectivity of 100:1 between silicon and silicon oxide in the ICP process. Deposition was divided into several 2.2 μm steps to prevent cracking of oxide layer due to residual stress. Detailed

parameters are given as below.

Description	Process parameters
SiH_4 flow rate	5 sccm
N_2O flow rate	90 sccm
Process pressure	400 mTorr
Process temperature	350 °C
RF power	11 W
Deposition rate	35 minutes resulting in 2.2 μm (repeat 2 times)

Step 3: Backside photolithography on silicon oxide

The backside photolithography was performed on an EV620 aligner on the silicon oxide deposited in the previous step, as shown in Fig. 3.1 (c). The photoresist was AZ4620 due to its available thickness in the spin coater. The thickness of AZ4620 was 7 μm according to the selectivity between AZ4620 and oxide in the buried oxide etchant (BOE). The photoresist mask should be hard baked for at least 1 hour before wet etching to ensure the material integrity. Detail parameters are given as below.

Step	Description	Process parameters
1	HMDS coating	150 °C 30 minutes
2	1st spin (spread cycle)	500 rpm 10 seconds
3	2nd spin (spin cycle)	2000 rpm 40 seconds
4	Static settlement	10 minutes
5	Soft bake	90 °C 12 minutes
6	Exposure	20 seconds
7	Development	80 seconds
8	DI water Rinsing	90 seconds
9	Hard bake	120 °C at least 1 hour

Step 4: Backside wet etching of silicon dioxide

This step is shown in Fig. 3.1(d). The silicon oxide below the photoresist was etched by a buffered oxide etchant (NH_4F: HF=6:1) with an etch rate of 1 μm per minute roughly. Due to the relatively low selectivity between silicon oxide and photoresist in the RIE process, we used BOE solution instead. The undercutting effect of wet etching was minimal and did not cause the pattern to peel off from the substrate. The samples than were immersed in DI water to wash off the BOE solvent to protect the photoresist mask from further BOE attack and prevent the peeling off problem.

Step 5: Frontside photolithography

The frontside photolithography was performed on an EV620 double side aligner to define the photoresist mask, as shown in Fig. 3.1(e). The subsequent ICP etching is the primary process to define the device structure. In order to protect the structure in the device layer, the frontside photolithography is performed after the backside etching process. The photoresist thickness is 5 μm because the minimum selectivity of ICP etching between silicon and AZ4620 photoresist is 40:1. Hard bake should be as long as possible to withstand the ICP etching. Detailed parameters are given below:

Step	Description	Process parameters
1	HMDS coating	150 °C 30 minutes
2	1st spin (spread cycle)	500 rpm 10 seconds
3	2nd spin (spin cycle)	4000 rpm 40 seconds
4	Static settlement	10 minutes
5	Soft bake	90 °C 7 minutes
6	Exposure	11 seconds
7	Development	60 seconds
8	DI water Rinsing	90 seconds
9	Hard bake	120 °C at least 1 hour

Step 6: Frontside deep reactive ion etching

The silicon structure in the device layer is defined by ICP etching which is performed by using a STS MESC multiplex ICP reactor with standard Bosch processes, as shown in Fig. 3.1(f). By applying suitable etching and passivation parameters, a better etching profile can be ensured. The details will be discussed later. In order to maintain a uniform etch rate and better heat dissipation, maximum helium leak rate should be limited. The averaged etch rate is roughly 2 μm per minute. Detailed parameters are given as below.

Description	Etch phase parameters	Passivation phase parameters
Time per cycle	11.5 seconds	7.0 seconds
SF_6 flow rate	130 sccm	0 sccm
C_4F_8 flow rate	0 sccm	85 sccm
O_2 flow rate	13 sccm	0 sccm
Coil RF power	600 W	600 W
Platen RF power	11.5 W	0 W
Process pressure	APC position = 81.2 % Base pressure = 0.3 mTorr	
Helium back side cooling	Helium back side pressure = 10 Torr Maximum helium leak up rate = 20 mTorr/min	
Etch rate	0.6-0.7 μm per cycle depending on pattern	

Step 7: Wafer dicing

Wafer dicing must be performed before the backside deep silicon etching. The reason is that the entire wafer becomes very fragile and may disintegrate in the reactor chamber when a large area of the backside silicon is removed. The other problem is that the residual stress in the buried oxide can damage the structures in the frontside layer. Therefore, the wafer is diced first by a Disco 2H/6T system. The structures in the device layer are protected during the dicing process by a 7-μm-thick AZ4620

photoresist. The detailed parameters of the protection photoresist coating are given as below. The subsequent backside etching will be conducted with the individual chips bonded to a carrier wafer with thermal grease.

Step	Description	Process parameters
1	Photoresist mask removal	A.C.E or H_2SO_4
2	1st spin (spread cycle)	500 rpm 10 seconds
3	2nd spin (spin cycle)	1800 rpm 40 seconds
4	Soft bake	20 minutes

Step 8: Backside deep reactive ion etching

Diced chips were bonded on a carrier wafer with thermal grease. The thickness of thermal grease should be limited and it should be applied to the peripheral areas to prevent contamination of the chips. In order to prevent the rupture of the carrier wafer, silicon oxide should be deposited on the carrier wafer before the chip bonding to avoid the plasma attacking during the ICP process. The process of the backside ICP etching is shown in Fig. 3.1 (g). Heat dissipation issues due to poor helium cooling capability on the bonded chip could jeopardize the selectivity and vertical profiles of the etched sidewalls. Fortunately, the backside structure is rather insensitive to or even benefiting from the non-vertical etching profiles. Since the goal of this step is creating holes to allow HF to attack buried oxide in the release step, a larger contact area caused by non-vertical profiles is beneficial in the following process. The process parameters are identical to these for the frontside ICP process in step 6.

Step 9: HF Release

The chip is released by 49 % HF to remove the unwanted buried oxide and the blocking structure in the handle layer. The process is shown in Fig. 3.1 (h). HF vapor can also release the device but the process is very time consuming.

The release time using 49% HF is about 20 min and the oxide layer is over etched in order to prevent shortage during metal deposition. Finally, the device is cleaned by rinsing in isopropanol (IPA) and then hot baked after the release is finished. DI water cannot be used for cleaning to avoid the stiction between the comb fingers in the release process.

Step 10: Silicon nitride deposition

In our design, a dielectric layer is applied on the fingers to avoid contact shortage. Silicon nitride is chosen because it is a good dielectric material with high dielectric constant ($\varepsilon_r = 7$). Low-pressure chemical vapor deposition (LPCVD) is used to deposit a 500-Å-thick sidewall nitride.

The original process using plasma-enhanced chemical vapor deposition (PECVD) was proved to be less efficient due to poor lateral coverage. Due to the poor selectivity between the silicon nitride and silicon oxide, HF release is performed before silicon nitrite deposition.

Step 11: Silicon nitride removal in anchor areas

After the silicon nitride was deposited, the top side silicon nitride layer on the anchor area should be removed by a SAMCO RIE-10N RIE in order to provide the electrical contact to the silicon device, as shown in Fig. 3.1 (j). To prevent the shortage between the fingers, the silicon nitride deposited on the top side of the comb finger cannot be removed.

With Shadow mask A in Fig. 3.1 (j), the silicon nitride is protected in the RIE process. Detailed parameters are given as below.

Description	Process parameters
SF_6 flow rate	30 sccm
CHF_3 flow rate	10 sccm
Helium backside cooling	15 sccm
Process pressure	50 mTorr
RF power	100 W
Etch rate	1000 Å per minute

Step 12: Metal deposition

As shown in Fig. 3.1(k), gold is deposited on the contact pads and the lateral contacts in the mechanical switches. With Shadow mask B in Fig. 3.1 (k), gold is only applied to the contact pad and the switch gap areas to prevent unwanted electrical conduction. E-gun evaporator was used in this process and the step coverage is better than our expectation. Titanium or Chromium must be applied as the adhesion layer to prevent gold from peeling off. Gold is used on contact switches and electrodes because of its good resistance to oxidative corrosion and excellent quality as a conductor of electricity. Aluminum should not be used because of its poor oxidation resistance. The detail process parameters are shown below:

Description	Process parameters
Ti/Cr deposition	1000 Å
Au deposition	4000 Å

Step 13: Wire bonding and external mass attachment

The last two steps are to bond wires from the contact pads to a PCB and then attach the external mass to the center hole to complete the device, as shown in Fig. 3.1 (l). The chip is attached to the PCB board with silver glue before wire bonding. Other adhesive material can also be used. The ball has a mass of 4 grams and is attached by epoxy. Care must be taken in this step otherwise the device may be broken.

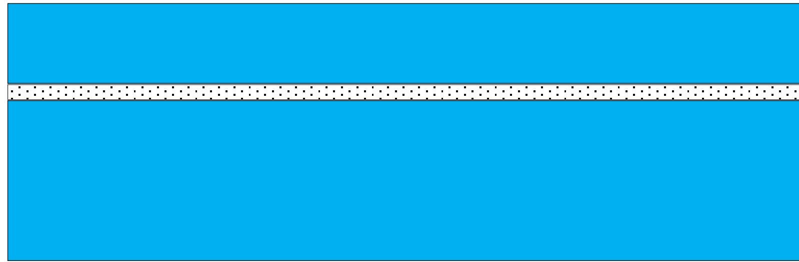

(a) RCA cleaning (Step 1)

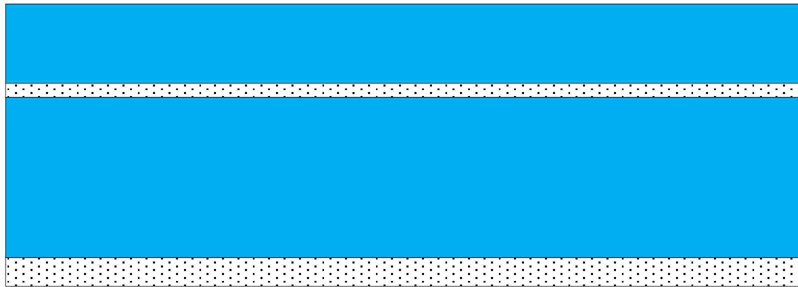

(b) PECVD silicon oxide deposition on the backside (Step 2)

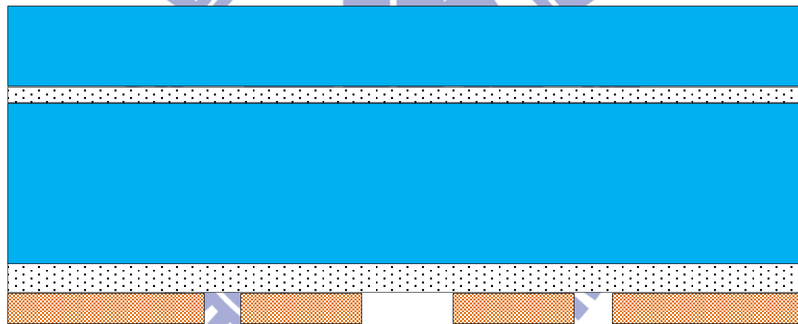

(c) Silicon oxide patterning by photoresist (Step 3)

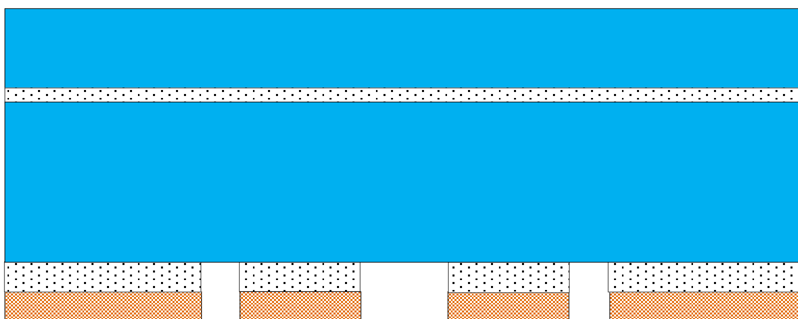

(d) Silicon oxide hard mask etching by BOE (Step 4)

Fig. 3.1 Fabrication process flow of the SOI device

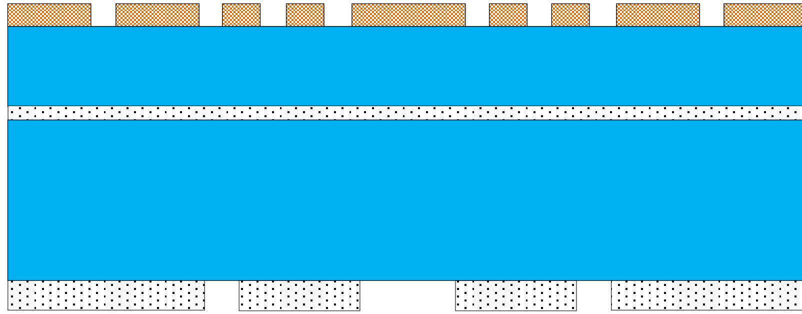

(e) Front side photoresist patterned by double side photolithography (Step 5)

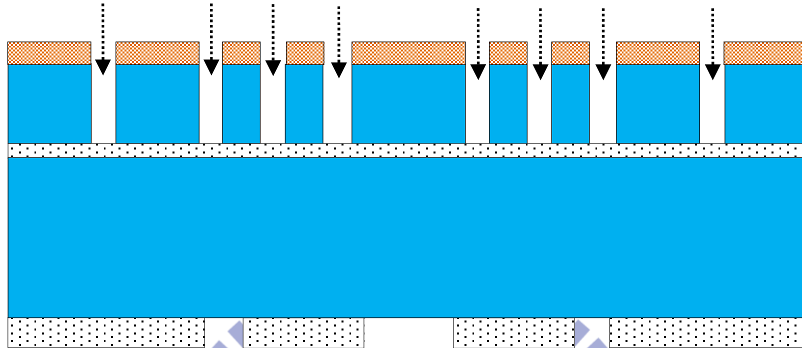

(f) ICP deep silicon etching on the front side (Step 6)

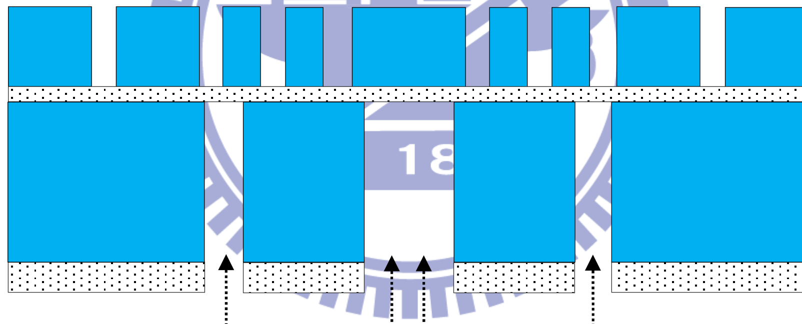

(g) Back side ICP deep silicon etching (Step 8)

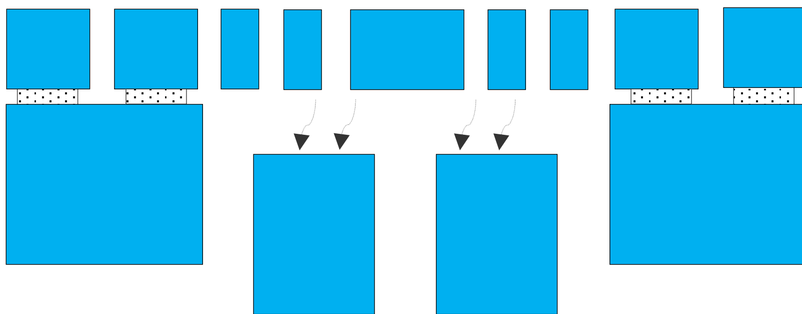

(h) Release in HF solution (Step 9)

Fig. 3.1 Fabrication process flow of the SOI device (continued)

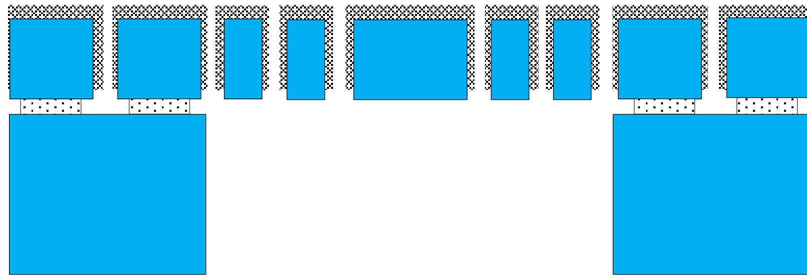

(i) Silicon nitride deposition by LPCVD (Step 10)

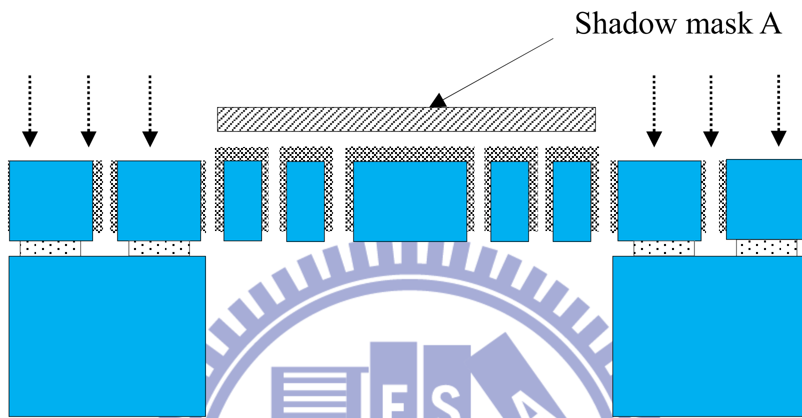

(j) Top side silicon nitride removal by RIE with Shadow mask A (Step 11)

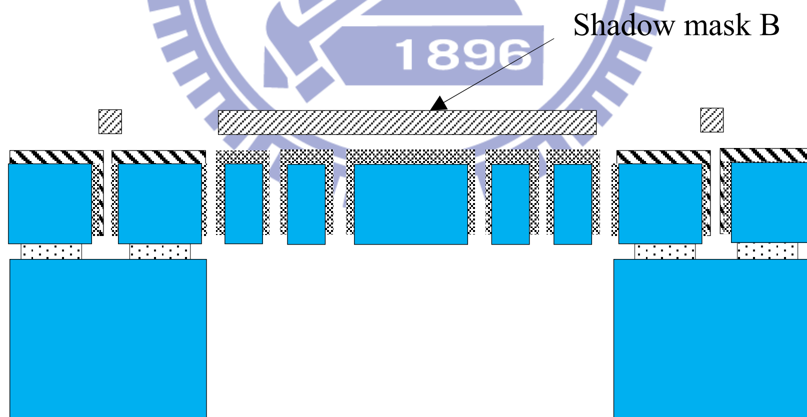

(k) Metal deposition by sputtering with Shadow mask B (Step 12)

Fig. 3.1 Fabrication process flow of the SOI device (continued)

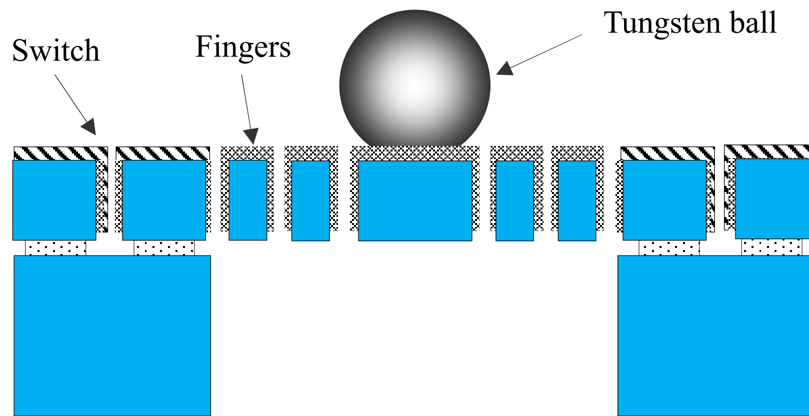

(l) Wire bonding and tungsten ball attachment (Step 13)

Fig. 3.1 Fabrication process flow on the SOI device (continued)

3.2 Processing issues and solution

A number of problems occurred in our fabrication. One of the problems is caused by the ICP etching process. Another major problem is the shortage of fingers due to poor isolation. This is the cause of parasitic conduction. Several procedures were taken in order to overcome those difficulties.

3.2.1 Non-ideal effects in the ICP process

Inevitably, non-ideal effects exist due to process inaccuracy. The effects include notching, loading effect, sidewall flatness, etc. The detail process will be discussed in the following sections.

Notching effect

Deep reactive ion etching through the silicon device layer is an essential step in microstructure fabrication. However, plasma etching the silicon over an insulator layer has a silicon notching problem at the silicon/insulator interface. The phenomenon is shown in Fig. 3.2 [42]. The positive charge accumulated in the

isolation layer causes deflection of reactant ion and forwarding scattering. The poor profile caused by the notching may result in degraded performances. As this undercutting is aspect ratio dependent, the profiles and the characteristics of the final devices may further vary across the wafer, affecting the repeatability and reliability, especially for thick device layers.

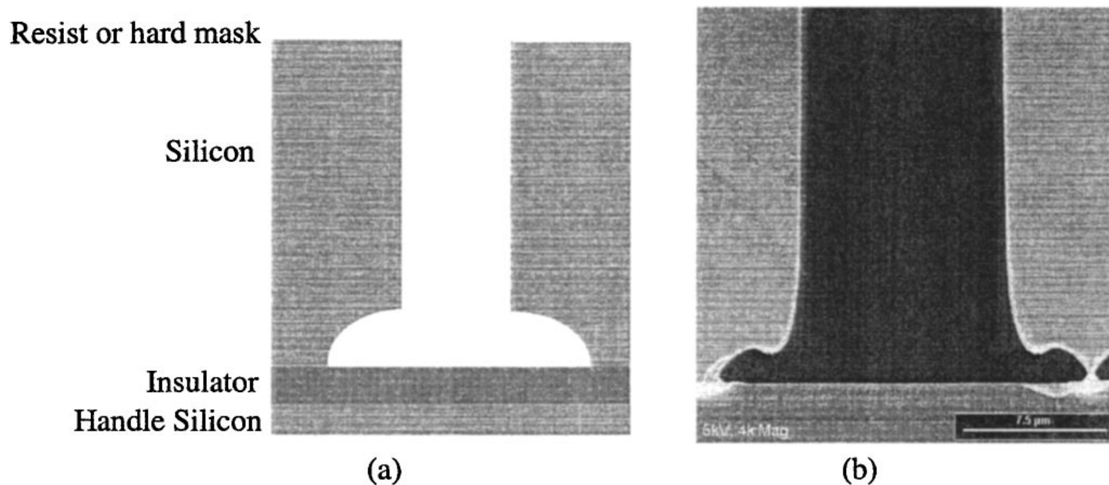

Fig. 3.2 Notching effect (a) schematic and (b) SEM micrograph [42]

The problem was encountered in our device structure, as shown in Fig. 3.3 (a). The bottom of the comb fingers was over etched due to the plasma bombarding on the interface between silicon and oxide. Therefore, the deep ion etching was divided into several steps to prevent over etching. The etch rate of the deep silicon etching should be controlled accurately. Once the depth of etching is approaching the estimated value, devices should be examined by an optical microscope to ensure the overetching is minimized. A better profile of comb fingers is shown in Fig. 3.3 (b) [2]

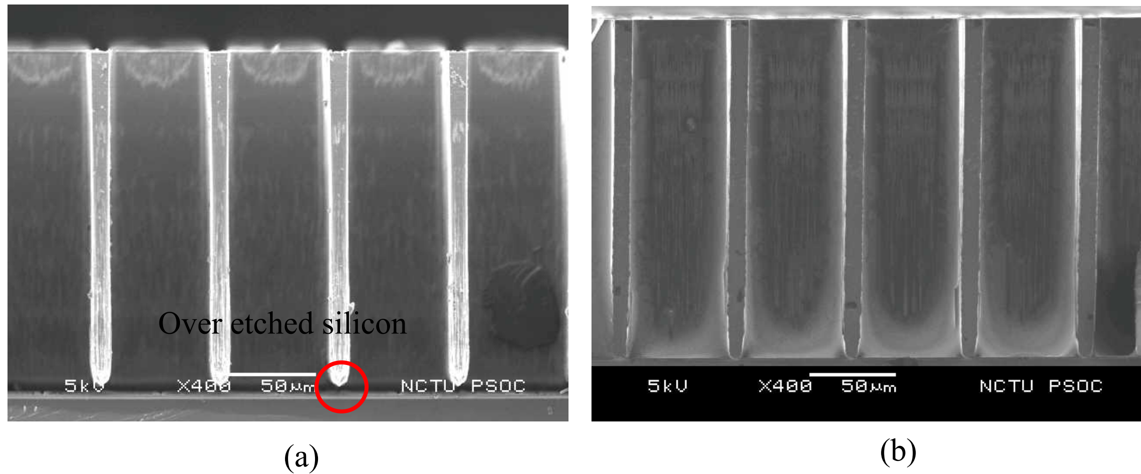

(a) (b)

Fig. 3.3 (a) Notching occurred on the finger's bottom, (b) improved result [2]

Loading effect

The loading effect is an important issue for the ICP etching process. This effect indicates that the etch rate will be severely reduced when the number of chips and percentage of the etched silicon area is too large [44]. It also happens in our device during the backside ICP etching. The etch rate in the ICP process is 0.6 μm per cycle with six chips but is reduced to about 0.56 μm with ten chips bonded on the carrier wafer. The etched silicon area is proportional to the number of chips bonded on the wafer. More chips on the carrier wafer also cause poor heat dissipation and reduce the etch rate of silicon.

3.2.2 Silicon nitride deposition

Silicon nitride is the material for the isolation layer. Many issues should be considered in the deposition process.

Shortage problem

Previously in our study, silicon nitride was deposited by plasma enhance chemical vapor deposition (PECVD) after the HF releasing. Nitride coated by

PECVD has low thermal stress compare with LPCVD. However, the technology suffers from poor step coverage on the sidewalls and the bottom corners, as shown in Fig. 3.4. This result causes shortage if the variable capacitor fingers touch one another. In addition, particles were produced to influence the deposition quality in the PECVD process [45]. Therefore, LPCVD nitride is adopted due to its better step coverage.

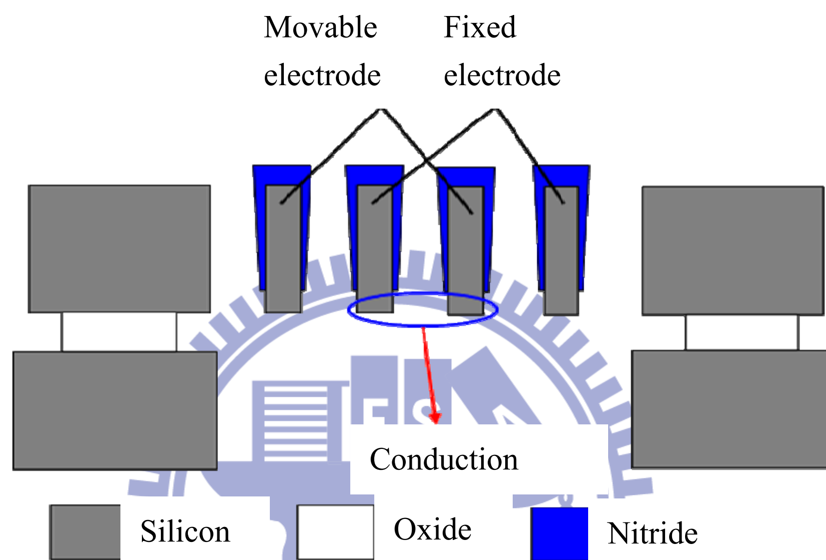

Fig. 3.4 Schematic of poor step coverage

Residue stress in LPCVD silicon nitride layer

Residue stress during the deposition is an important issue. The thickness of LPCVD silicon nitride should be considered or else the residue stress may leads to structure deformation or lifetime reduction. Fortunately, the effect of the residual stress in silicon nitride is ignorable in our case because the wafer is diced before nitride deposition. The properties of the LPCVD and PECVD nitride are listed in Table 3.1 [46]. We deposit a 3000Å-thick LPCVD silicon nitride and expect a 500Å-thick lateral silicon nitride coating based on empirical data.

Table 3.1 Thin film property of LPCVD and PECVD nitride [46]

Deposition type	LPCVD	PECVD
Typical temperature(^{o}C)	750~850	250~350
Density (g/cm^{3})	2.9 to 3.1	2.4 to 2.8
Resistivity(Ω.cm)	10^{16}	10^{6} to 10^{15}
Dielectric strength (10^{6} V/cm)	10	5
Stress (M Pa)	1000 (tens.)	200(comp.) to 500 (tens.)

3.2.3 Metal deposition issues

Shadow mask

Shadow masks produced with highly accuracy must be applied in order to prevent metal conduction at the bottom gap between anchors. The shadow mask was made of silicon and the open windows were defined by normal photolithography and ICP etching. The Shadow mask is a 14mm × 14mm square as shown in Fig. 3.5. The experiment result is shown in Fig 3.6. The metal regions are successfully separated.

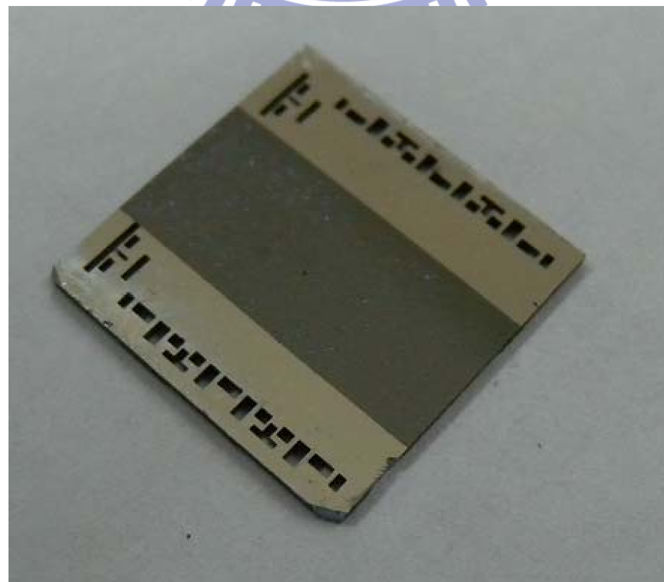

Fig. 3.5 Shadow mask

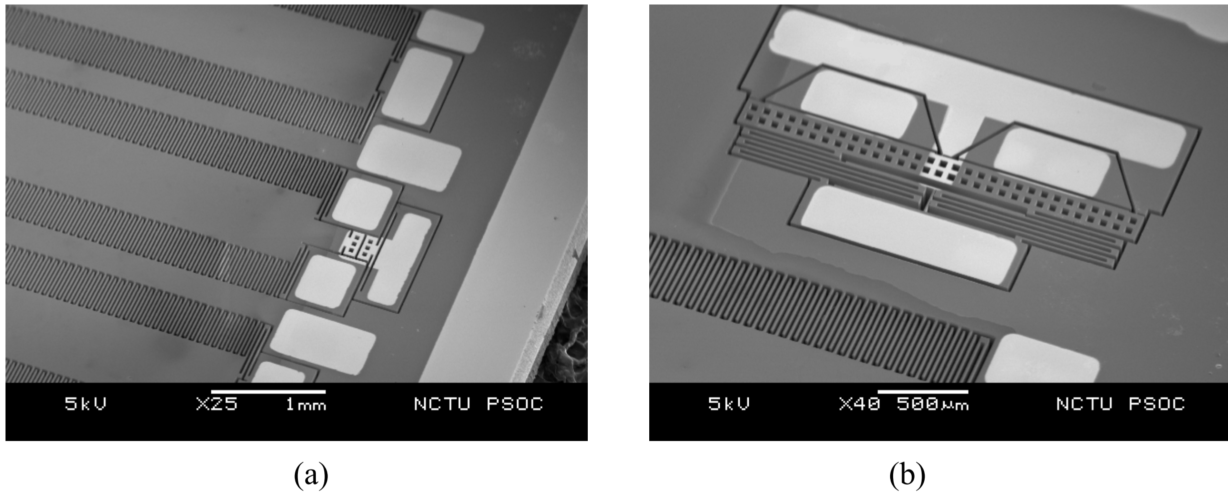

(a) (b)

Fig. 3.6 (a) Gold deposition on SW1 and anchors (b) Gold deposition on SW2

Sidewall metal contact

Contact switches are critical for the device to work properly. Previously in our study [47], the switches suffered from low contact conductance. This is potentially caused by the oxidation corrosion and poor step coverage of the aluminum coating. To solve this problem, we conducted gold evaporation experiment to test the side coating capability of the E-gun evaporating process. The minimum thickness of gold as a conducting material is approximately 200 Å based on empirical data. We examined the devices to determine if the gold coating met our requirement.

Fig. 3.7 is the upper part of a test finger covered by gold. The gold particle can be seen very clearly. The EDS (Energy Dispersive Spectrometer) result at the position indicated in Fig 3.7(b) is shown in Fig 3.8, confirming that the coating material is gold.

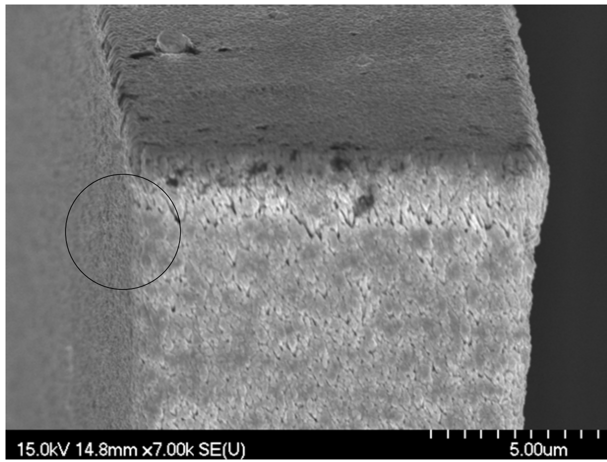

(a)

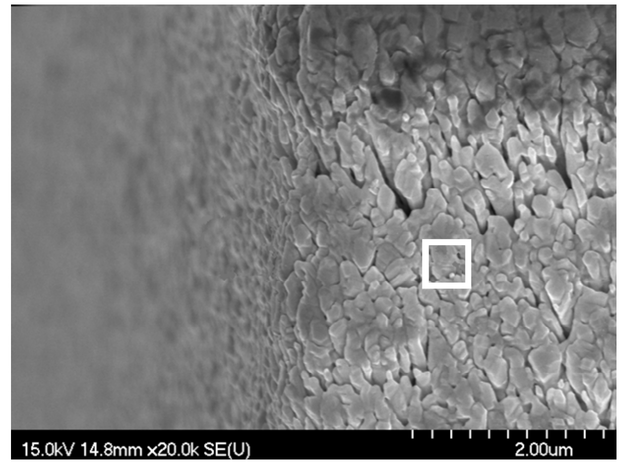

(b)

Fig. 3.7 (a) Upper part of a gold coated test finger, (b) close-up view

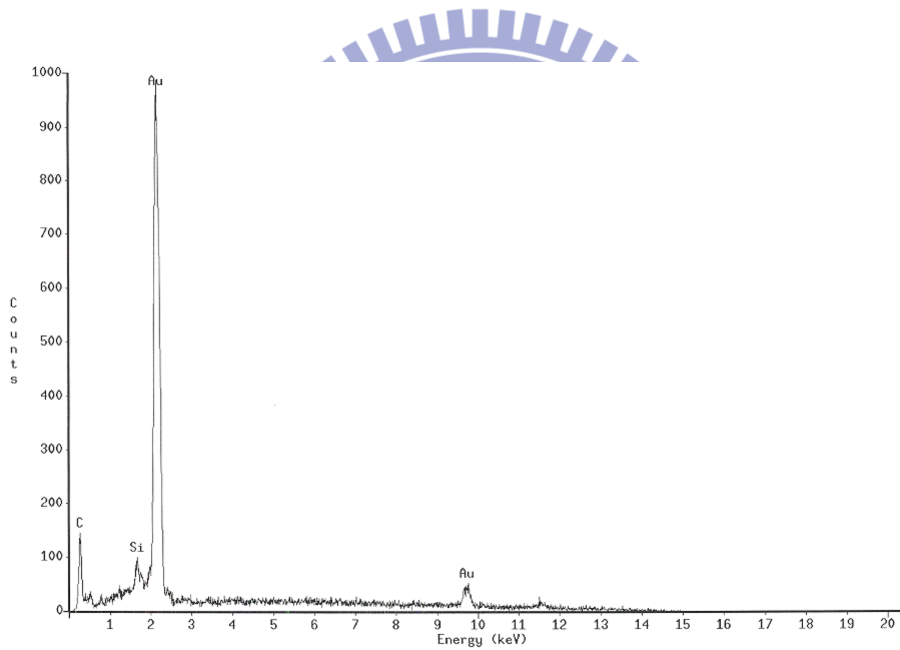

Fig 3.8 EDS result at square in Fig 3.7(b)

Fig 3.9 shows the cross section of the upper test structure. The thickness of gold on the side wall is approximately 0.3 μm which is larger than the 200Å requirement. The EDS result in Fig 3.10 shows the exposed area is silicon as we expected.

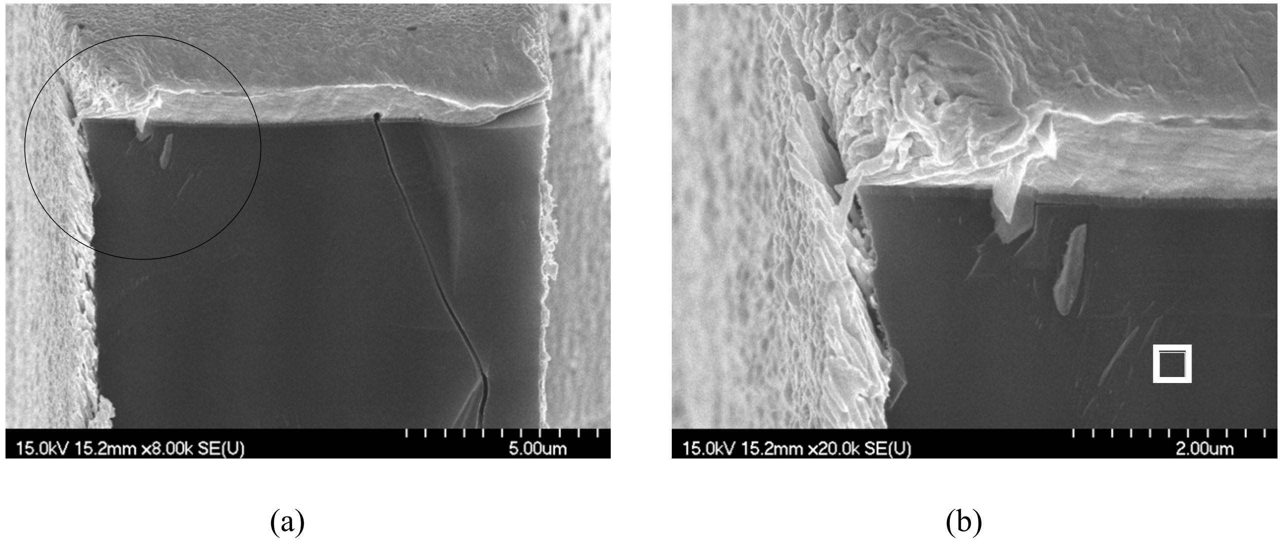

(a) (b)

Fig. 3.9 (a) Cross section of test structure, (b) close-up view

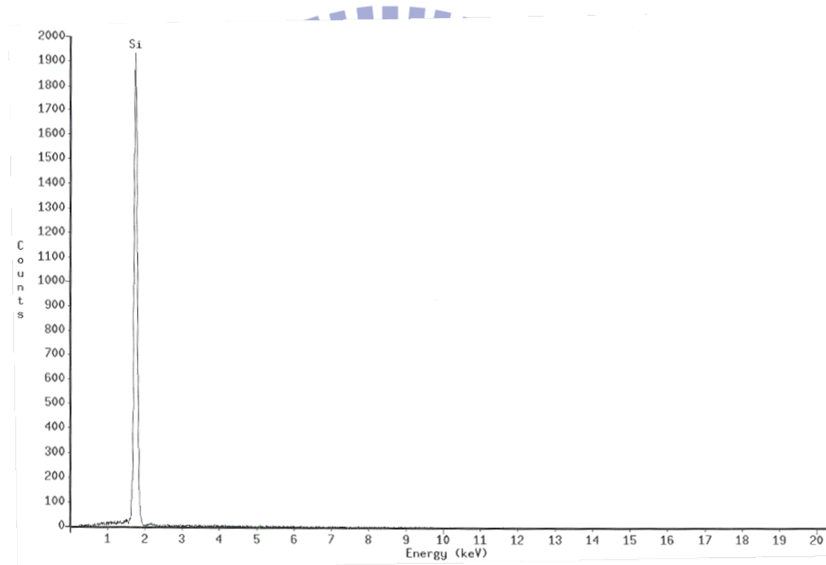

Fig 3.10 EDS result at square in Fig 3.9(b)

Fig 3.11 shows the cross sectional view of the test structure 130 μm below the substrate surface. In the high resolution SEM photo we can still see the gold particle clearly as shown in Fig 3.11 (c). However, the wavelike etching profile of the deep ICP etching causes difficulty to determine the actual thickness of deposited gold. The EDS result in Fig 3.12 shows the side wall gold coating density is less than the upper part. Fortunately, the gold deposited on the upper part of the sidewall is acceptable as a contact material.

(a) (b)

(c) (d)

Fig 3.11 (a) Cross section view of test structure, (b) close-up view 130 μm below substrate surface, (c) gold particles on wavelike etching profile, (d) wavelike etching profile.

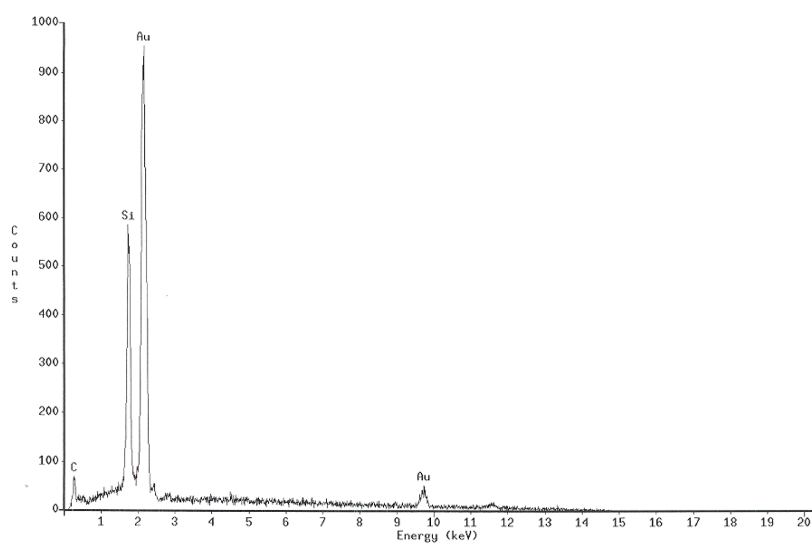

Fig. 3.12 EDS result at square in Fig 3.11(c)

In this improved coating process, the coverage of evaporated gold is good enough to achieve the contact requirement from the above measured results. The stability of gold is also far more superior to aluminum. Table 3.2 summarizes the EDS results of the sidewall coating.

Table 3.2 Element percentage at upper and lower part of sidewall

Depth	1μm	130μm
Au	88.24%	62.10%
Si	4.05%	35.62%
Others	<8%	<3%

3.3 Fabricated device

A fabricated die is shown in Fig. 3.13. The central hole is used to mount the external mass in order to adjust the resonant frequency to the design specification. The fingers and serpentine springs are shown in Fig. 3.14. The depth and width of these structures are 200 μm and 10 μm, respectively. In order to yield the ideal finger width of 10 μm, the width on the mask should be pre-enlarged to 13 μm to compensate for the dimension shrinkage during the photolithography and ICP processes. Switch 1 and Switch 2 are shown in Fig. 3.15 and Fig 3.16. We can notice that gold is successfully deposited on the sidewall of the contact region in Switch1 and Switch2, as we expected in Section 3.2.

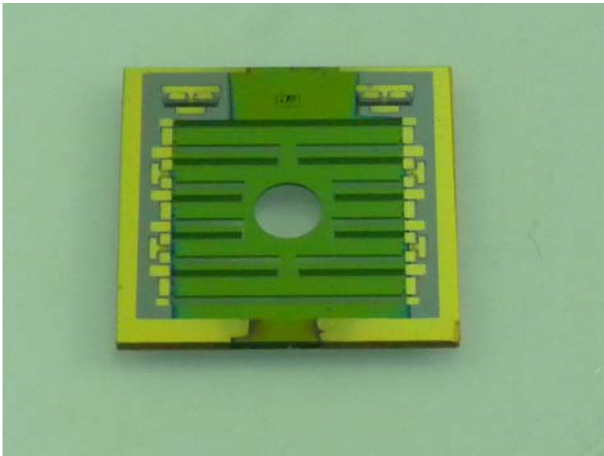

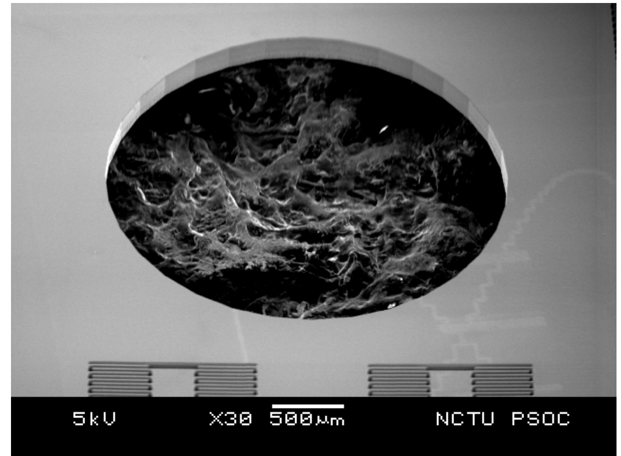

(a) (b)

Fig. 3.13 (a) Fabricated die, (b) central hole for mounting the external mass

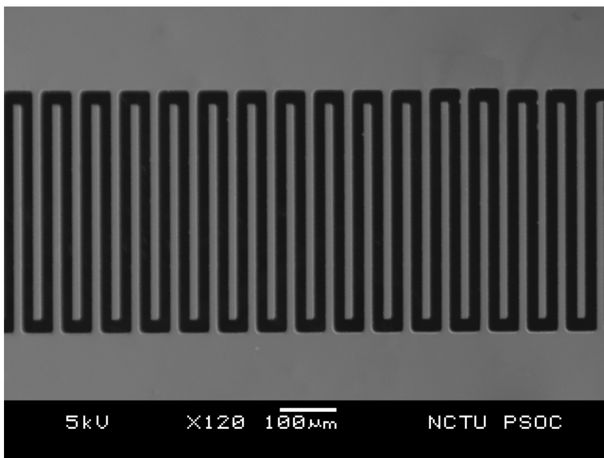

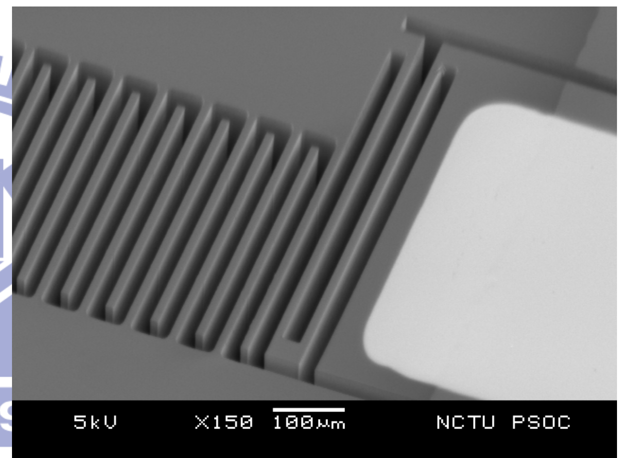

(a) (b)

Fig. 3.14 Close-up view of (a) fingers, (b) serpentine spring

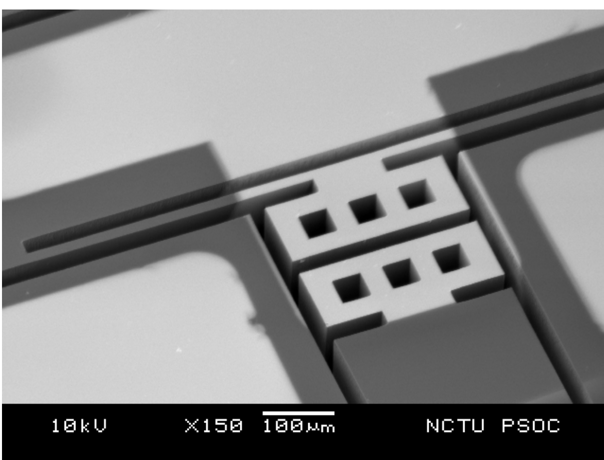

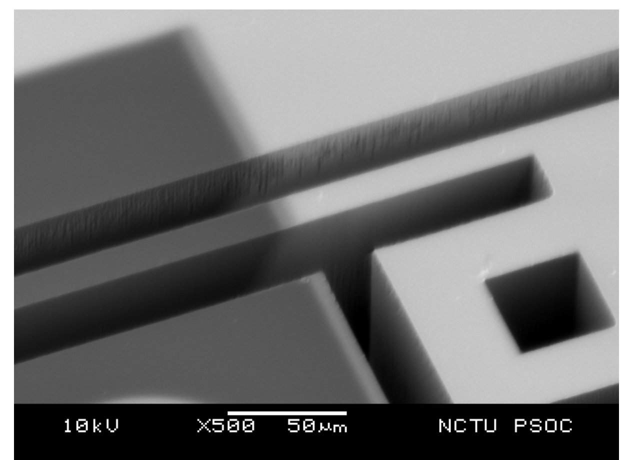

(a) (b)

Fig 3.15 (a) Close-up view of Switch 1, (b) deposited gold on silicon

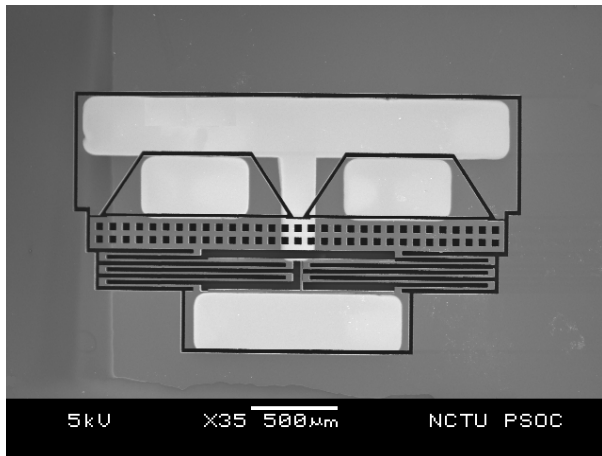

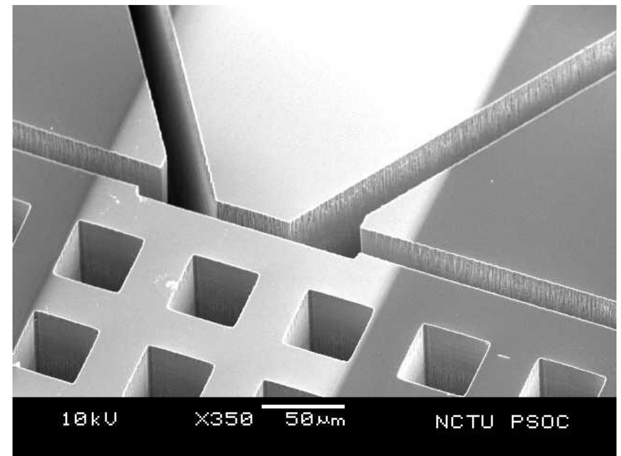

(a) (b)

Fig. 3.16 (a) Top view of Switch 2, (b) close-up view of Switch 2

The backside of the device was also inspected. Fig. 3.17 shows the backside under Switch 1. The purpose to remove the backside silicon is to reduce parasitic capacitance between the moving plate and the substrate. The backside hole can also eliminate the electrical leakage problem of Switch 1 after metal deposition.

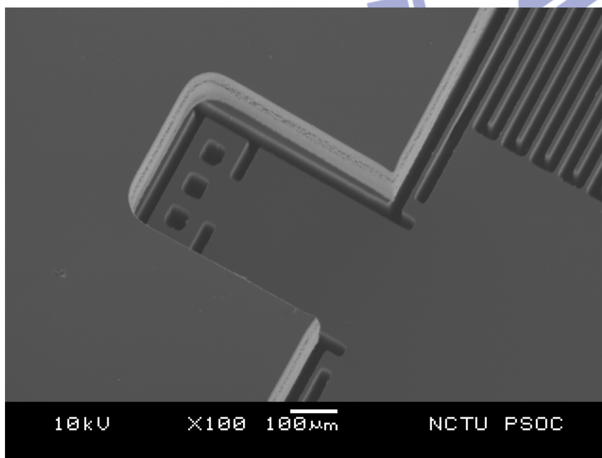

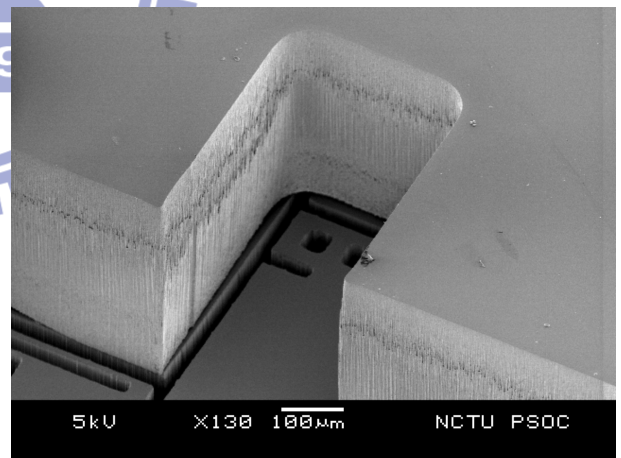

(a) (b)

Fig. 3.17 (a) Backside silicon removed under Switch 1 (b) close-up view

Fig. 3.18 shows the optical micrograph of the device with LPCVD silicon nitride coated on the fingers. The vertical line in Fig. 3.19 is the boundary between silicon and nitride after the frontside nitride is removed. It is caused by the rugged

shape of the laser cut shadow mask. Finally, the complete device is shown in Fig. 3.19. A tungsten ball is mounted on the device and the die is wire bonded to a PCB.

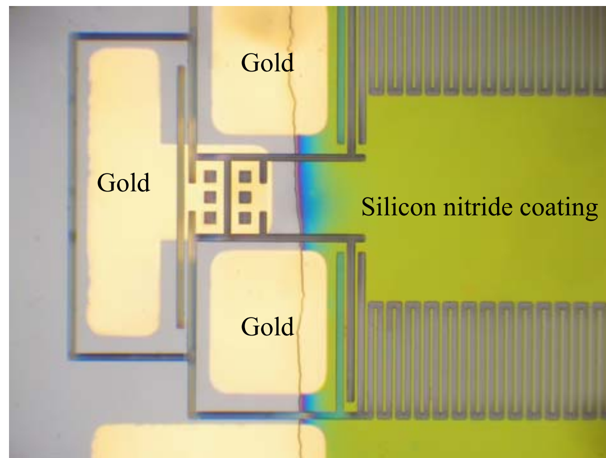

Fig. 3.18 Device with silicon nitride coating

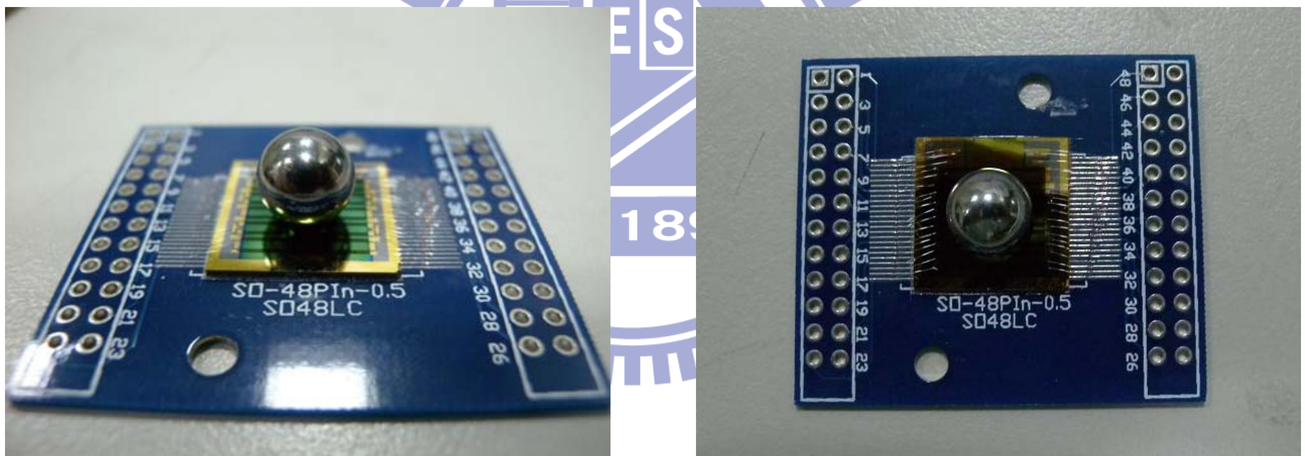

(a) (b)

Fig. 3.19 (a) Device with the external mass on PCB, (b) top view

3.4 Summary

The high-aspect-ratio SOI device was finished successfully. Several process issues were encountered and the corresponding solutions were found. The unwanted conduction problem was reduced by using LPCVD silicon nitride to replace the original PECVD silicon nitride which was proven to have poor insulation capability.

Shadow masks were also utilized to prevent metal conduction between anchors and moving electrodes. Other characterization measurement will be presented in the following chapter.

Chapter 4 Measurement and Results

In this chapter, the characterization of the fabricated energy converter is presented. Device displacement and resonance condition were observed in the mechanical measurement. Electrical measurements include static parasitic capacitance and resistance measurement. Mechanical switch measurement is presented in both the dynamic and static electrical measurement.

4.1 Mechanical measurement

The goal of mechanical measurement is to measure the mechanical frequency response of the device and determine its resonant frequency. Mechanical characteristics of the device are measured with input vibration acceleration generated by a shaker. The measurements were performed with the external mass attachment.

4.1.1 MEMS Motion Analyzer measurement

The dynamic response of the device was measured by the MEMS Motion Analyzer (MMA) as shown in Fig. 4.1. A piezoelectric-shaker mounted on the platform provided the input vibration. A function generator connected to the shaker applied the driving signal. The device was glued on the mini-shaker to ensure the stability during test. The MMA system utilizes image processing technique to determine dynamic characteristics. The MMA measures the periodic relative motion between the movable and the static structures of the device by captured images.

The device with and without the external mass were measured by the MMA system. The experiment results are shown in Fig. 4.2 and Fig. 4.3. From the amplitude and phase response, the resonant frequency is around 122 Hz and 1680Hz with and without the external mass, respectively.

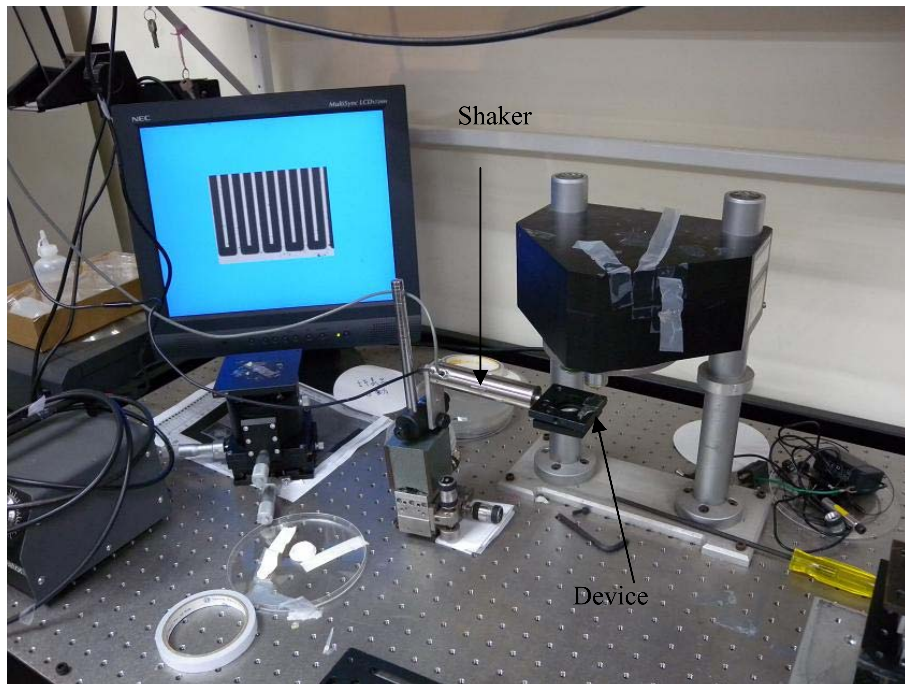

Fig. 4.1 MMA system

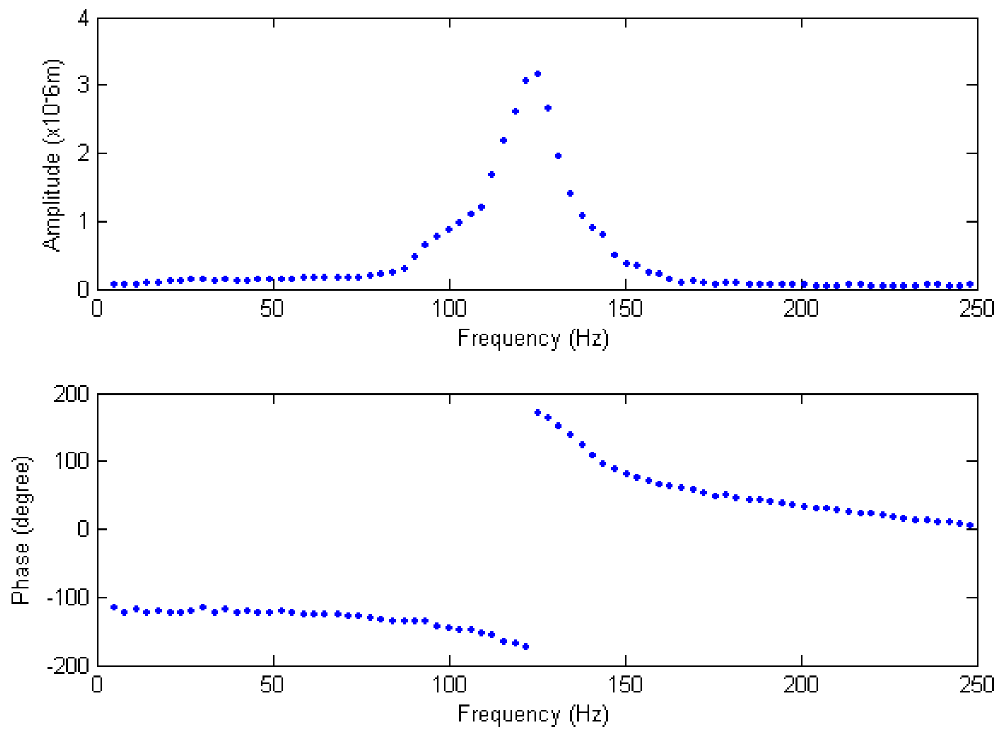

Fig. 4.2 Frequency response with external mass

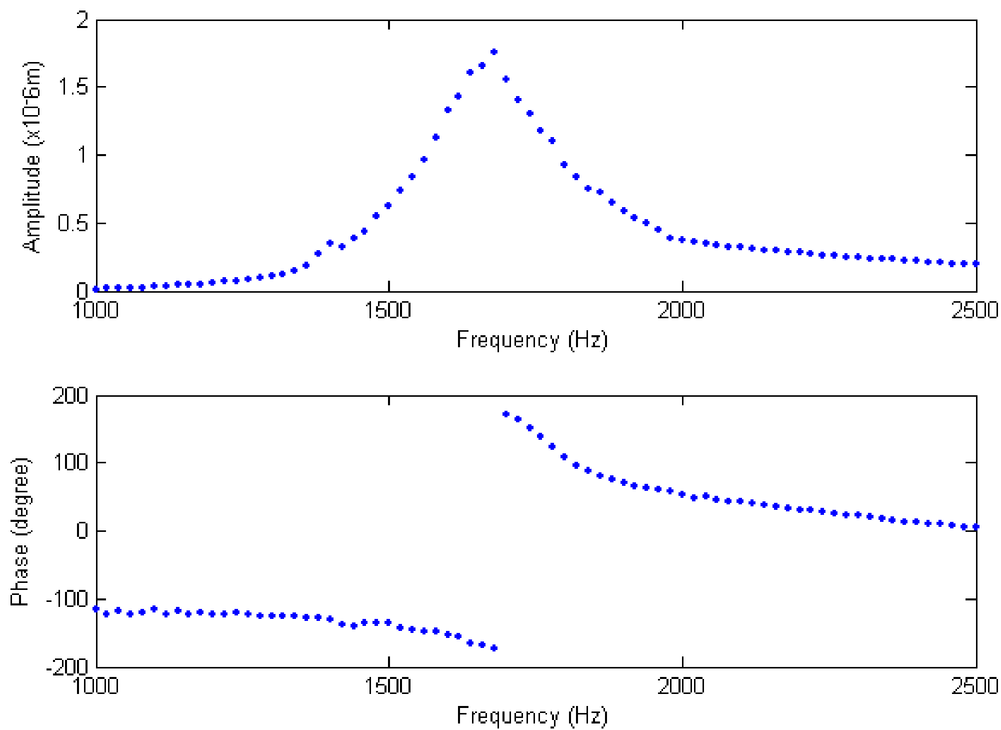

Fig. 4.3 Frequency without external mass

The amplitude and phase responses match a mass-damper-spring system characterized by the equation

$$|Z| = \frac{m\omega^2}{\sqrt{(k-m\omega^2)^2 + b_m{}^2\omega^2}}|Y|, \tag{4.1}$$

$$\phi = -\tan^{-1}\frac{b_m\omega}{k-m\omega^2}, \tag{4.2}$$

where Y as the input displacement amplitude, Z as the output displacement amplitude, and ϕ is the phase difference. The response is zero at DC frequency and constant when frequency is over the resonant frequency. The amplitude response indicates a 3dB bandwidth of about Δω = 14 Hz with external mass, and 160Hz without external mass. The quality factor is 8.6 with external mass and 10.5 without external mass respectively. The low value does not match the expectation by the equation.

$$Q = \sqrt{\frac{km}{{b_m}^2}} \tag{4.3}$$

From the Eq. 4.3, the device can operate in a low-damping environment to get a high quality factor. So the device packaging under vacuum environment is a proposed solution.

4.1.2 Vibration measurement by our shaker

Our test setup is shown in Fig. 4.4. The amplified sinusoidal signal was used to drive a LABWORK INC. ET-132 shaker. The sinusoidal vibration was measured by a piezoelectric accelerometer (PCB Piezotronics model 353B17) connected to an oscilloscope. The resonance of device was observed by an optical microscope and image of the relative displacement were captured.

Fig. 4.5(a) shows the device at rest. The vibration frequency was tuned from 100 Hz to 150 Hz to find the resonant frequency. From the images taken from the optical microscope, the resonant frequency was observed to be 118 Hz. For the accelerometer reading of 234.5mV, 2.27 m/s^2 input acceleration was calculated with the sensor sensitivity of 103.2mV/m/s^{-2}. The device has a displacement of 21 μm due to the large inertial force carried by the external mass, as shown in Fig. 4.5 (b). The input acceleration measured by the accelerometer module is shown in Fig. 4.5 (c)

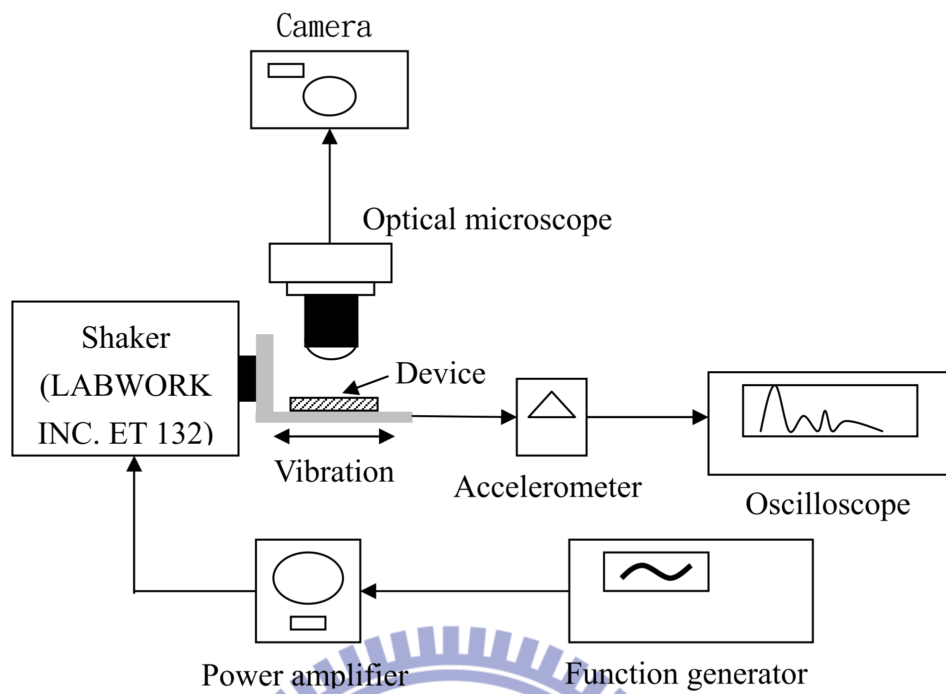

(a)

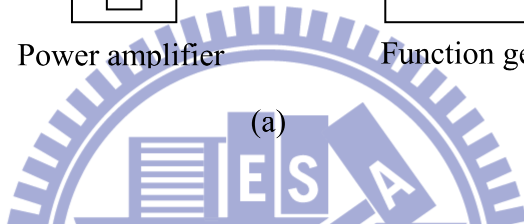

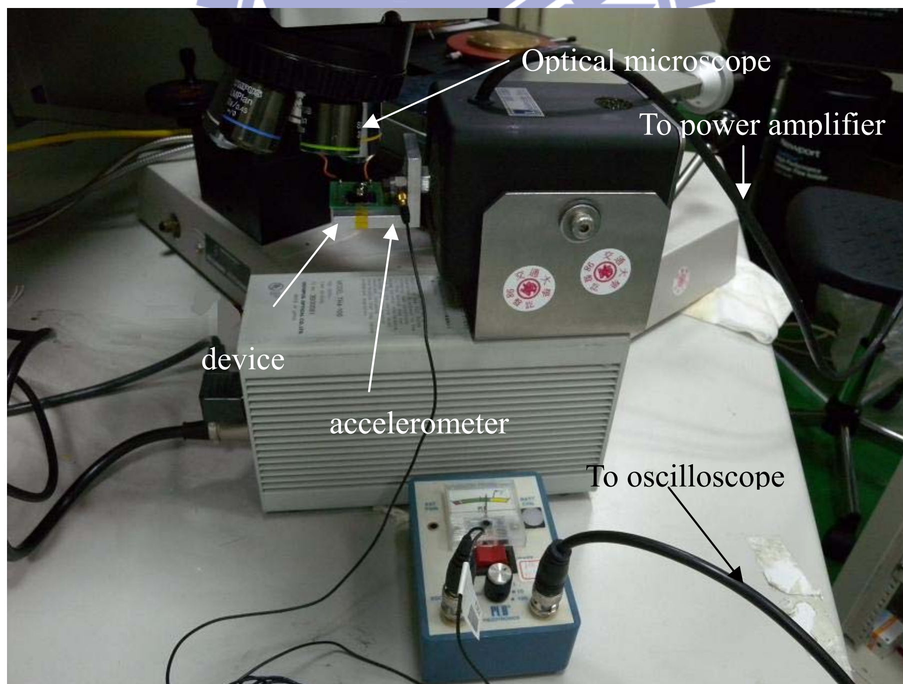

(b)

Fig. 4.4 (a) Mechanical measurement schematic (b) measurement setup

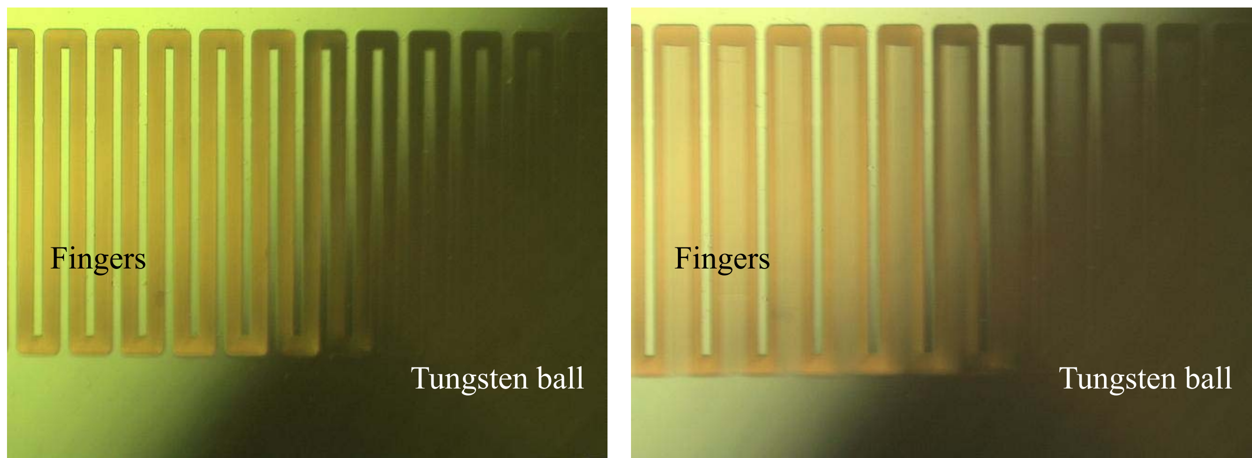

(a) (b)

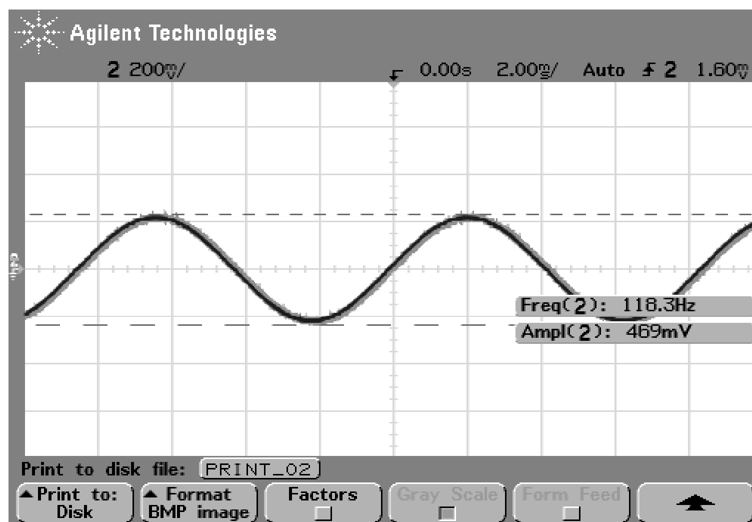

(c)

Fig. 4.5 (a) Device at rest (b) device at resonance of 118 Hz (c) input acceleration waveform.

4.2 Static electrical measurement

Parasitic resistance and variable capacitance of our devices were measured in static electrical measurement. In order to improve the insulation between fixed and movable fingers, LPCVD nitride layer was employed. The measurements were also compared with theoretic values and the difference between measurements and theoretical values are discussed in this section.

4.2.1 Leakage resistance

In order to ensure good insulation, a measurement circuit was implemented to measure the leakage resistance of the LPCVD nitride insulation, as shown in Fig. 4.6. The DC current through the device is zero if no leakage resistance R_p exists, resulting in a zero voltage drop across R_T. The input bias current of the CA3140 CMOS operational amplifier is below 10 pA, and the output voltage offset caused by the buffer can be neglected. Using this measurement circuit with V_T = 10 V and R_T = 10 MΩ, the output voltage was 0.6 V, indicating a leakage resistance of about 156.7 MΩ. The leakage resistance was also measured by an INSTEK-LCR-816 LCR meter. The results was 150 MΩ which agreed with the measurement from Fig. 4.6.

In our previous fabrication without using the high precision shadow mask, the parasitic resistance is below 1MΩ [43]. In the first device using shadow mask, the leakage resistance had been increased to 103MΩ [47]. Therefore, we had increase the value by 50% .

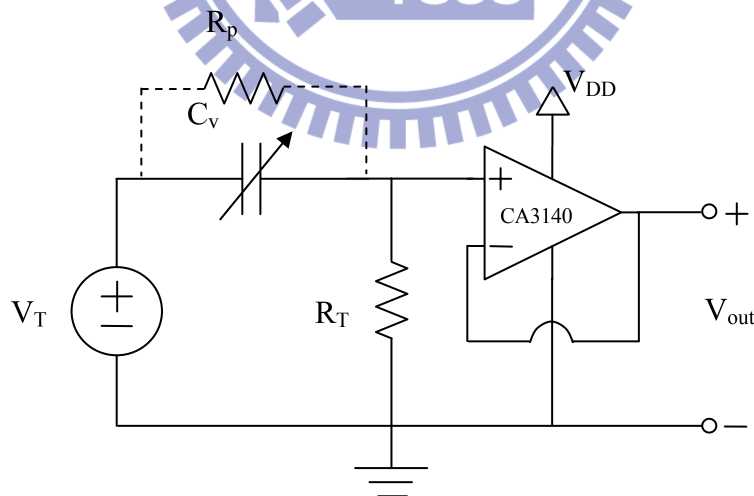

Fig. 4.6 Leakage resistance measurement circuit

Another circuit was used to measure the RC discharge time constant versus finger displacement, as shown in Fig. 4.7 [43]. In this case, SW_r is a relay controlled

by a 5 V input V_{tri}. The relay SW_r is initially closed by the control voltage V_{tri}. The variable capacitor is charged to $V_{in,}$ and then the relay is opened so that the charge on C_v is discharged through R_L. The pulse wave of V_{tri} is produced by a function generator to trigger the switch.

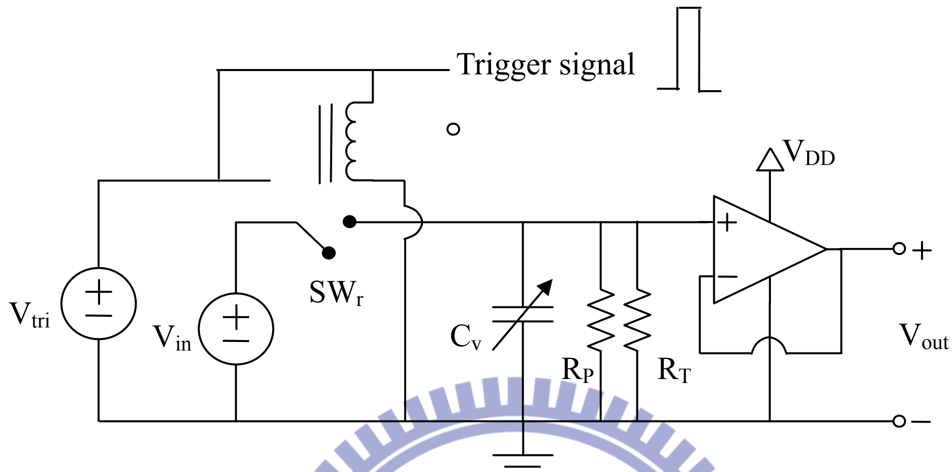

Fig. 4.7 Variable capacitor measurement circuit [43]

With a R_L of 10 MΩ and a V_{in} of 10 V, the RC discharge time constant versus finger gap displacement is measured. Fig. 4.8 shows the RC discharge for different positions of the variable capacitor. The variable capacitor is moved by a microprobe and the static displacement is measured from the image captured by the optical microscope. The RC discharge time constant was calculated from the time span between 100% and 36.8% of $V_{in.}$

The discharge resistance is equal to the parallel connection of R_T and the leakage resistance R_P. The capacitance can then be calculated from the time constant. The calculated capacitance (C_{actual}) can be compared with the theoretical value (C_{ideal}), as shown in Fig. 4.9. The calculated value of the minimum variable capacitor is 94 pF (theoretical value of 60 pF), indicating a parasitic capacitance of 34 pF in the device.

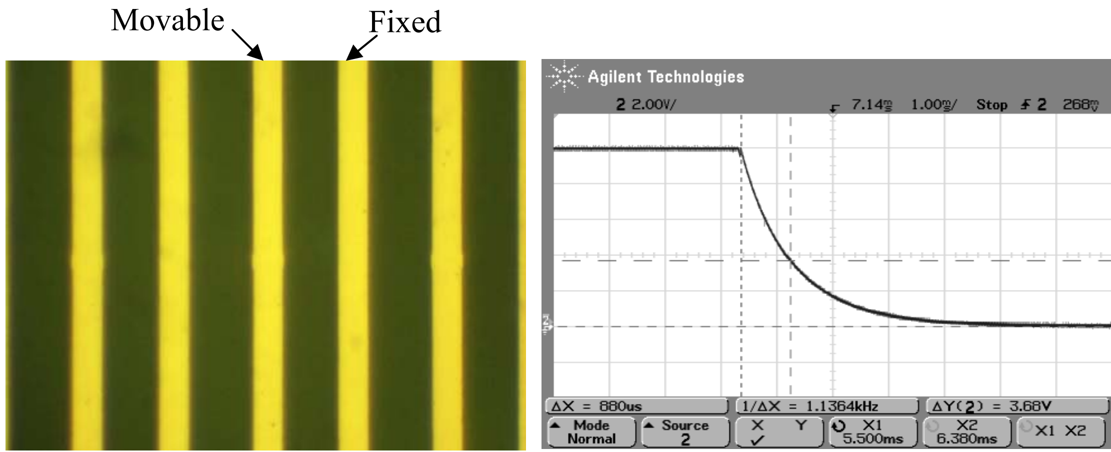

Displacement = 0μm　　　　Time constant τ = 880μs

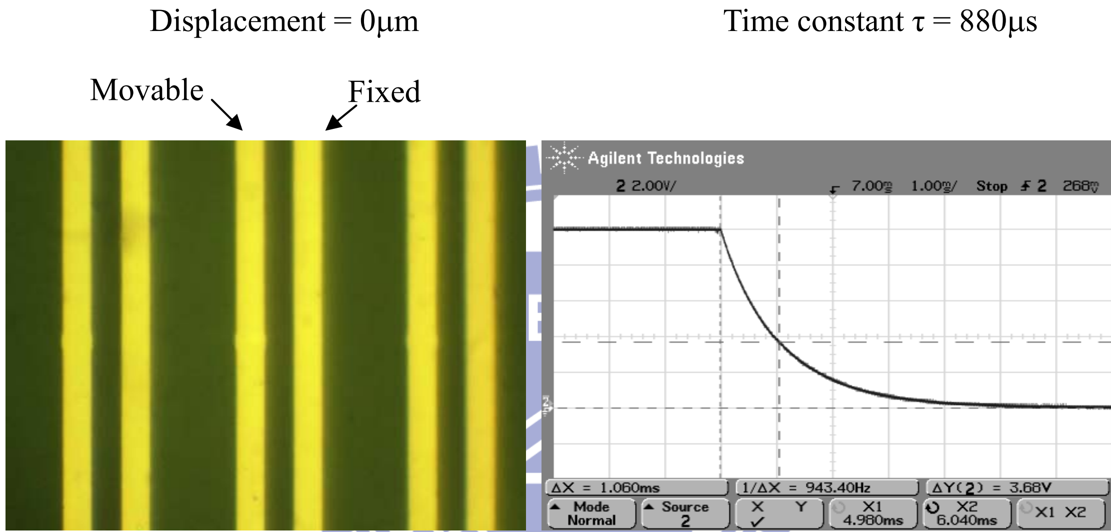

Displacement = 13μm　　　　Time constant τ = 1.06ms

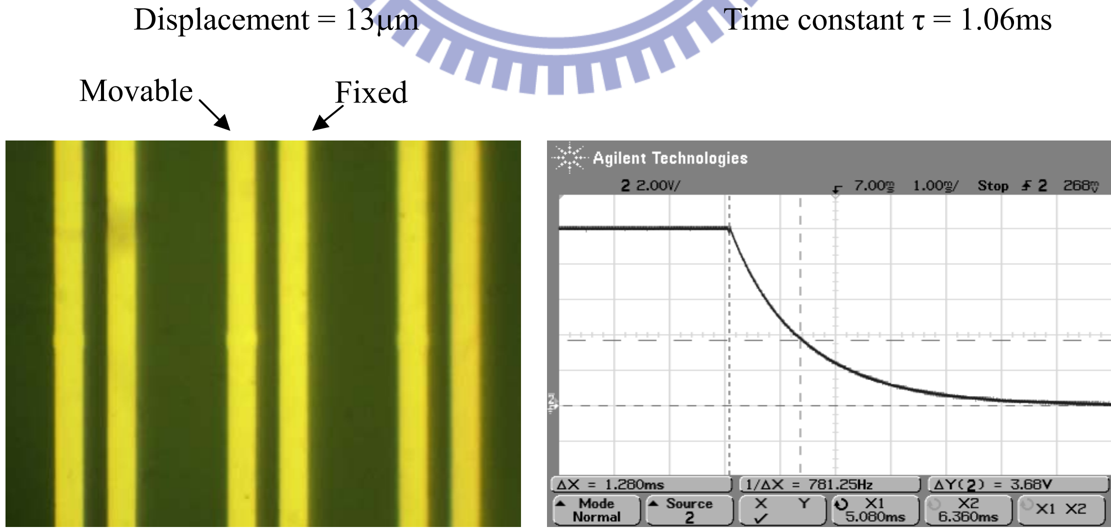

Displacement = 17μm　　　　Time constant τ = 1.28ms

Fig. 4.8 RC discharge time constant measurement

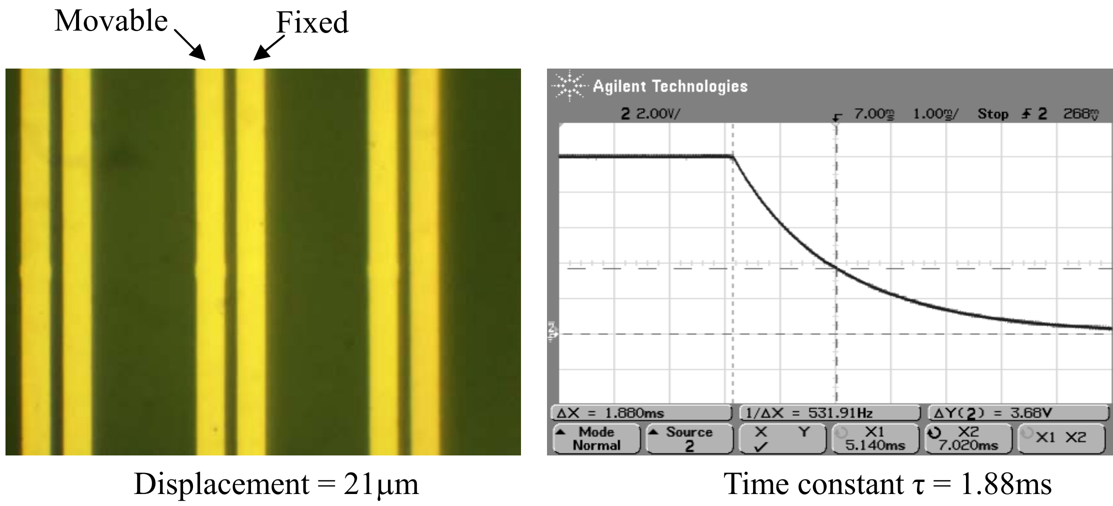

Displacement = 21μm Time constant τ = 1.88ms

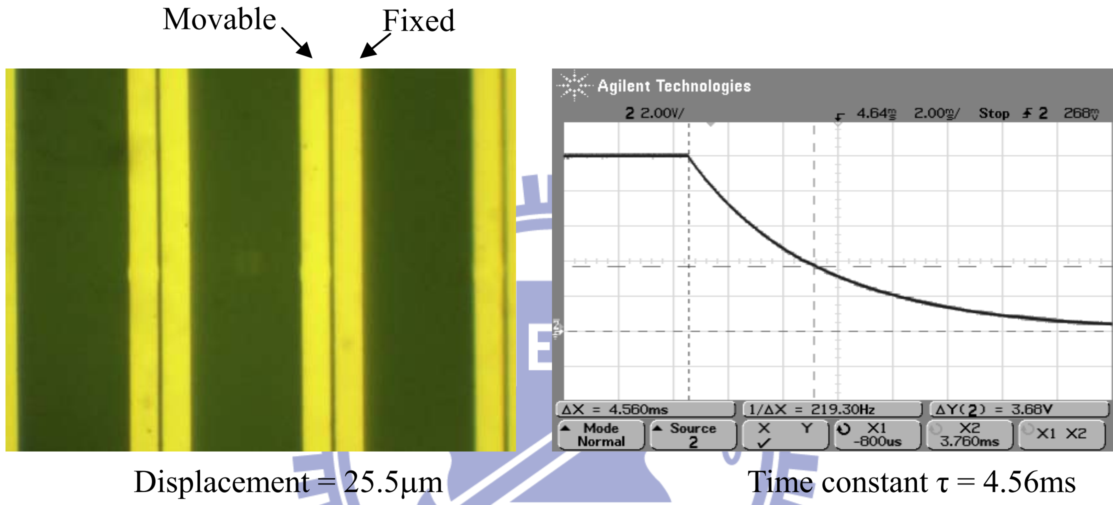

Displacement = 25.5μm Time constant τ = 4.56ms

Fig. 4.8 RC discharge time constant measurement (continued)

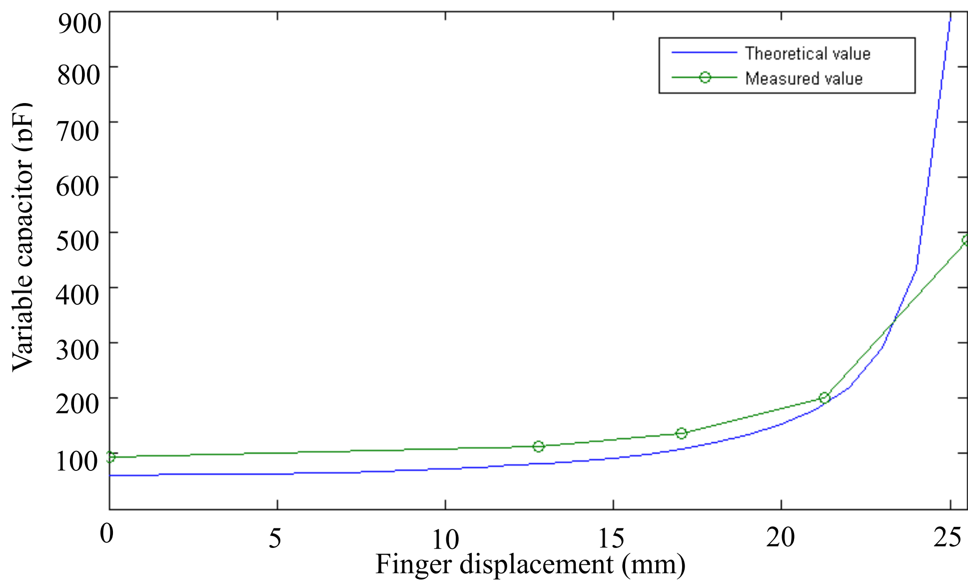

Fig. 4.9 Measured variable capacitor versus displacement

Moreover, the maximum capacitance of 485 pF is far lower than theoretical value C_{ideal} of 1570 pF. Therefore, the oblique sidewall issues were considered. A non-parallel capacitance was defined by the non-vertical ICP etching [48]. The schematic of the non-parallel capacitance is shown in Fig. 4.10, where h is thickness of fingers, θ is the oblique angle of the finger sidewall, and $d_1 = 0.6\mu m$ and $d_2 = 51.4\ \mu m$ are gap between the fingers. The non-parallel capacitance C_{actual} is expressed as follow [48]

$$C_{actual} = \frac{\varepsilon L_f}{2\theta} \ln\left(\frac{(d_1+2h\theta)(d_2+2h\theta)}{d_1 d_2}\right) \tag{4.4}$$

The ratio between the actual and the ideal capacitance (θ=0) is

$$r = \frac{C_{actual}}{C_{ideal}} = \frac{d_1 d_2}{2h\theta(d_1+d_2)} \ln\left(\frac{(d_1+2h\theta)(d_2+2h\theta)}{d_1 d_2}\right) \tag{4.5}$$

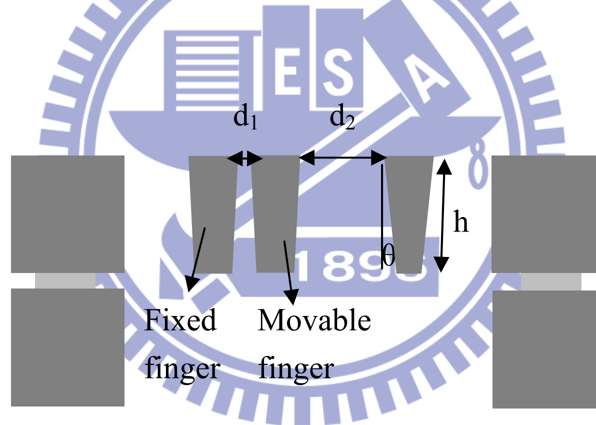

Fig. 4.10 Cross-section of non-parallel capacitor

The relationship between the oblique angle and ratio is plotted in Fig. 4.11. The ideal maximum capacitance of 1570 pF is shown in Fig. 4.9. Our measurement result of the maximum capacitance implies an oblique angle of 0.59˚. Fig. 4.12(a) shows the oblique finger sidewalls. Furthermore, the rough sidewall surface also limits the gap between the fingers and thus produces the non-ideal maximum capacitance, as shown in Fig. 4.12(b). The issues are mentioned in Chapter 3. To improve this issue, a fine tuned recipe of ICP should be adopted.

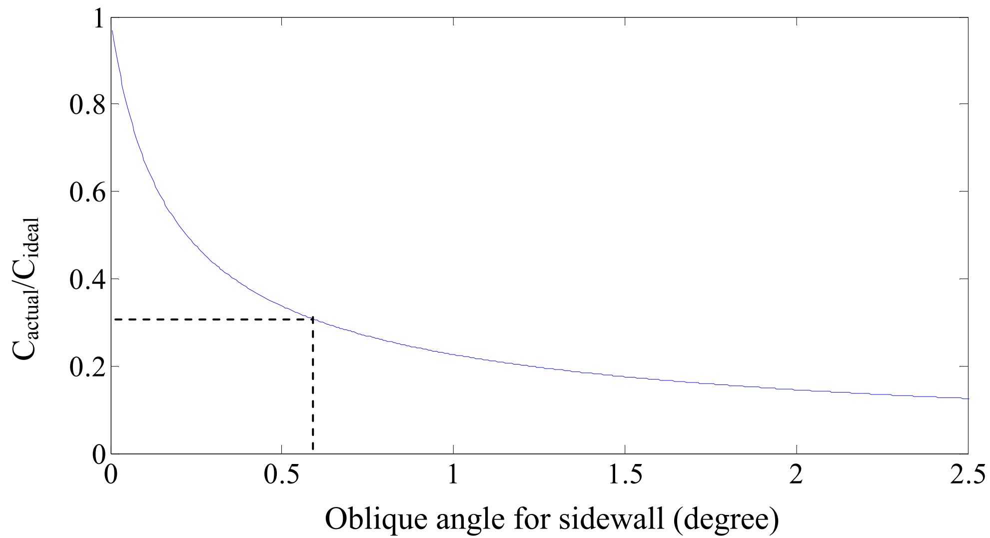

Fig. 4.11 C_{actual}/C_{ideal} versus oblique angle

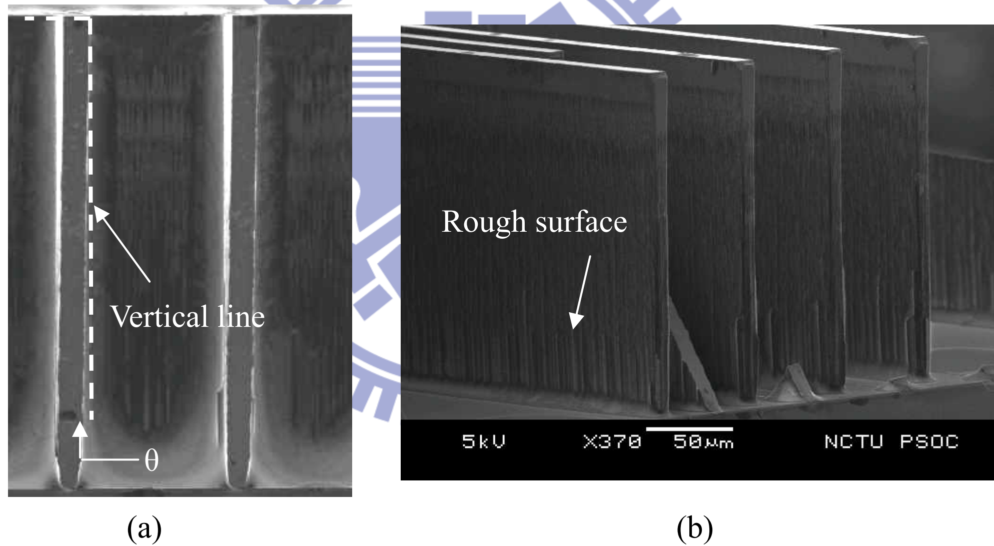

(a) (b)

Fig. 4.12 SEM photo (a) Close-up of non-parallel capacitance (b) rough surface of finger sidewall [47].

4.2.2 Static measurement of SW1

Mechanical contact switches are designed to work in the DC mode, as shown in Fig. 4.13. SW1 should be turned on in the battery charging process. In static measurement, a microprobe was used to push the movable plate to turn SW1 on, as shown in Fig. 4.14. The gold wire was bonded to the PCB. The bias voltage V_{in} for

the variable capacitor is 3.6V. The output voltage was measured by an oscilloscope, as shown in Fig. 4.15. The result shows a voltage of 3.6V was measured on node B. That means the switch was turned on and charging process can work properly. The contact resistance of SW1 was also measured by a LCR meter to be 0.5 to 2Ω. This low contact resistance indicates that the SW1 can work successfully.

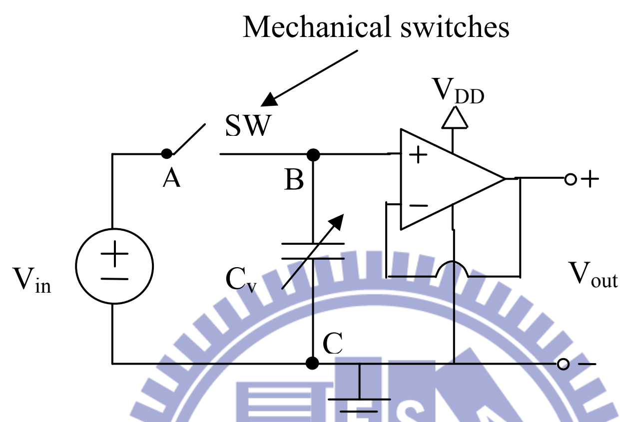

Fig. 4.13 DC model operation with mechanical switches

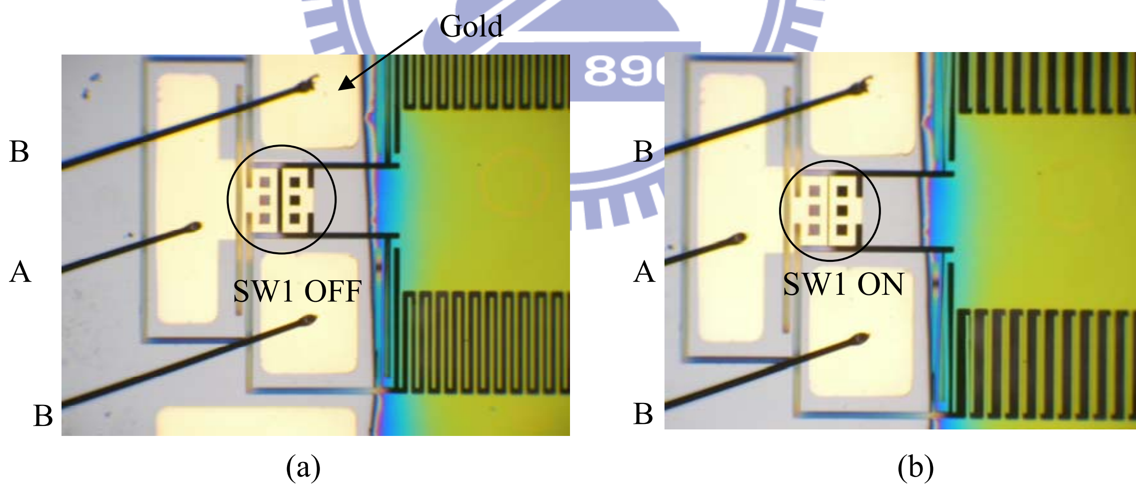

Fig. 4.14 Mechanical switch SW1 is (a) off (b) on

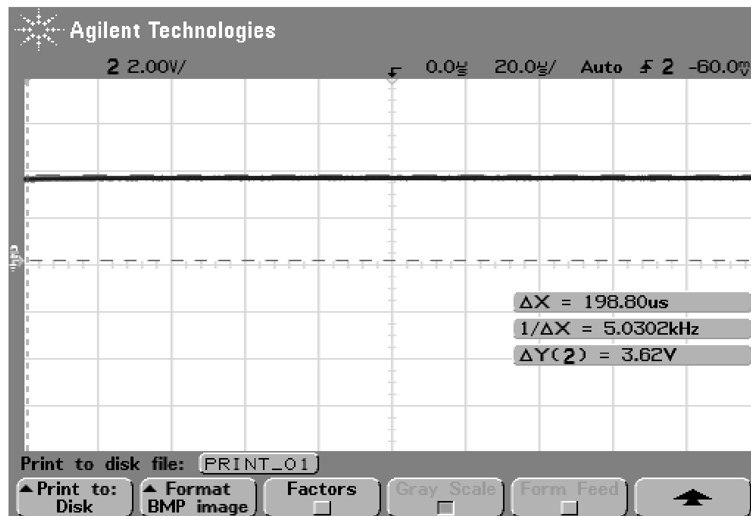

Fig. 4.15 Charge Voltage

4.2.3 Static measurement of SW2

The pull-in voltage of SW2 was measured by applying a voltage between nodes B (SW2) and GND (pull-in electrode) while the displacement was observed through a microscope. The measurement shows that the pull-in voltage of SW2 is approximately 98V. The release voltage of 54V was also measured by reduce the voltage across the B and GND node. The pull-in voltage measurement is higher than the design value of 74V and the release voltage is also higher than the design value of 50V. The difference between measured and design value is also caused by non-vertical etching profile.

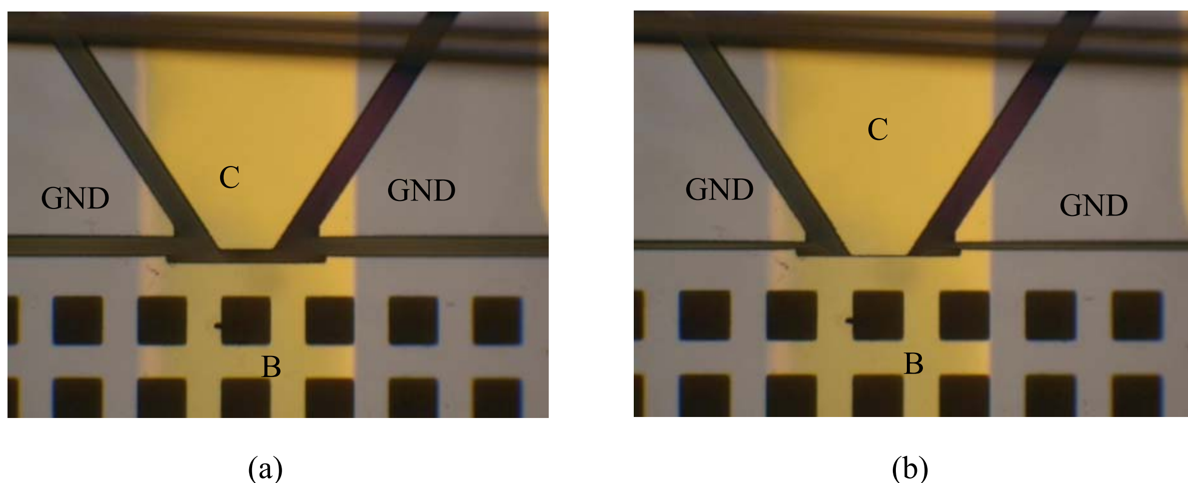

Fig. 4.16 SW2 with (a) no applied voltage, (b) 98 V applied voltage (pull-in)

4.3 Dynamic electrical measurement

The voltage of the variable capacitor increases as the capacitance decreases. SW1 are turned on when the fingers reaches the maximum relative displacement are reached. Thus the magnitude of mass movement should be large enough to make SW1 contact. The device without the mass attached was operated at the resonant frequency of 1739 Hz and the vibration acceleration of 25.2 m/s^2. The voltage on the variable capacitor was also measured by the circuit shown in Fig. 4.13. The output signal is shown in Fig. 4.17. It shows the voltage of 3.6 V during the charging process. The maximum voltage V_{max} of variable capacitor is 14.6 V which was smaller than the expected values of 91 V, indicating the change of variable capacitance is small. Fig. 4.18 shows the measurement of the voltage on the variable capacitor and the input acceleration.

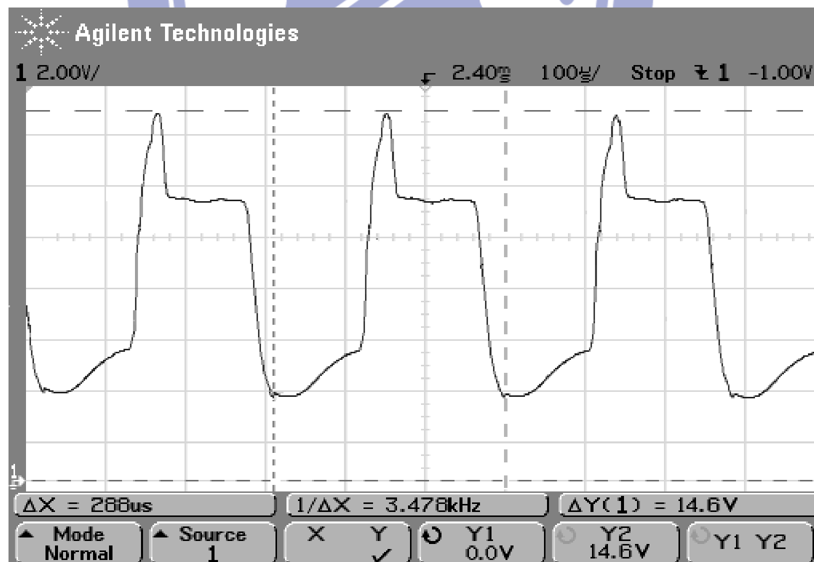

Fig. 4.17 Voltage on the variable capacitor

Because the maximum voltage on variable capacitor is far lower than the design value, we tried to increase the voltage difference by applying a negative voltage of 84V across B and GND to achieve the pull-in voltage of 98V, as shown in Fig. 4.19.

However, as the SW2 closed, the minimum voltage of 87.6V across B and GND is still large than the release of 54V, causing SW2 to stick to the close position. We thus propose another method by applying a control signal to SW2 as shown in Fig. 4.20. We first to use a full-wave rectifier to achieve synchronous, than we transfer a sinusoid wave into square wave, by controlling the delay signal, we may achieve a precise timing control of SW2. Finally, the precise control signal is amplified by a high voltage amplifier to reach pull-in and release voltage. Another method is to simply amplify the capacitor voltage by a high voltage amplifier as the pull-in control voltage. The measurement is still in progress.

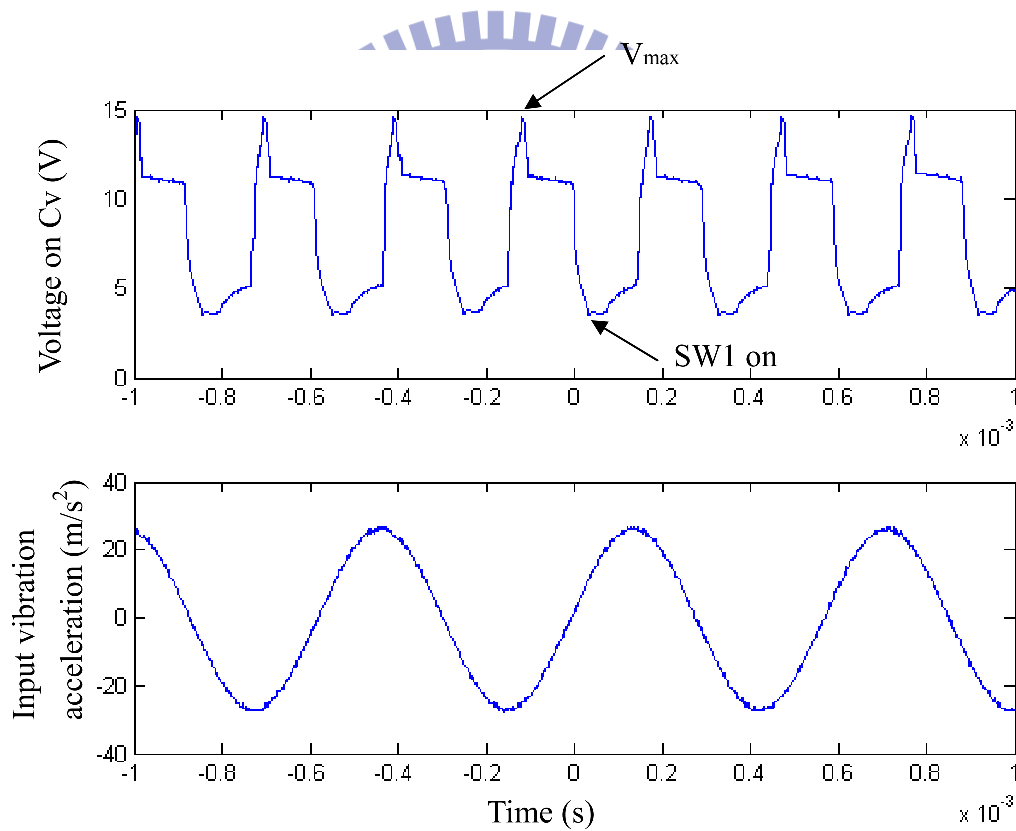

Fig 4.18 Voltage on the variable capacitor and input acceleration

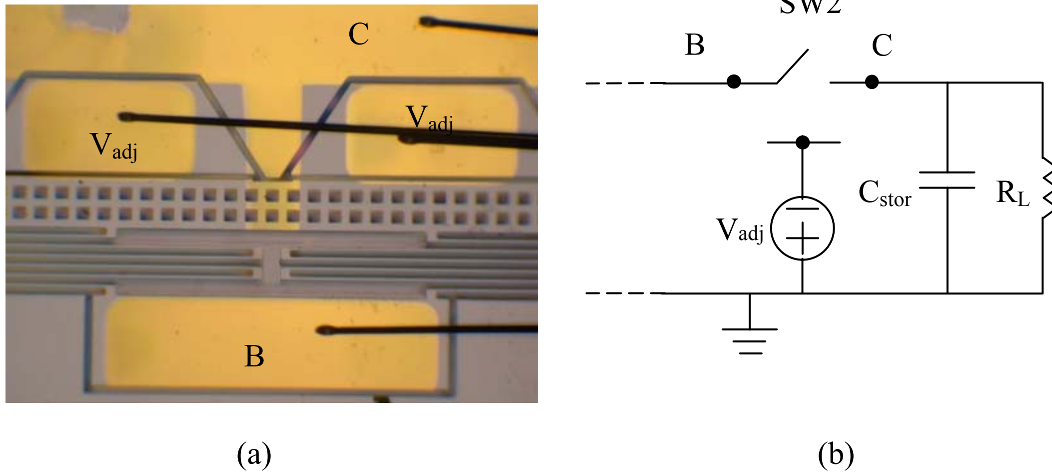

(a) (b)

Fig. 4.19 (a) SW2 overview, (b) SW2 schematic circuit

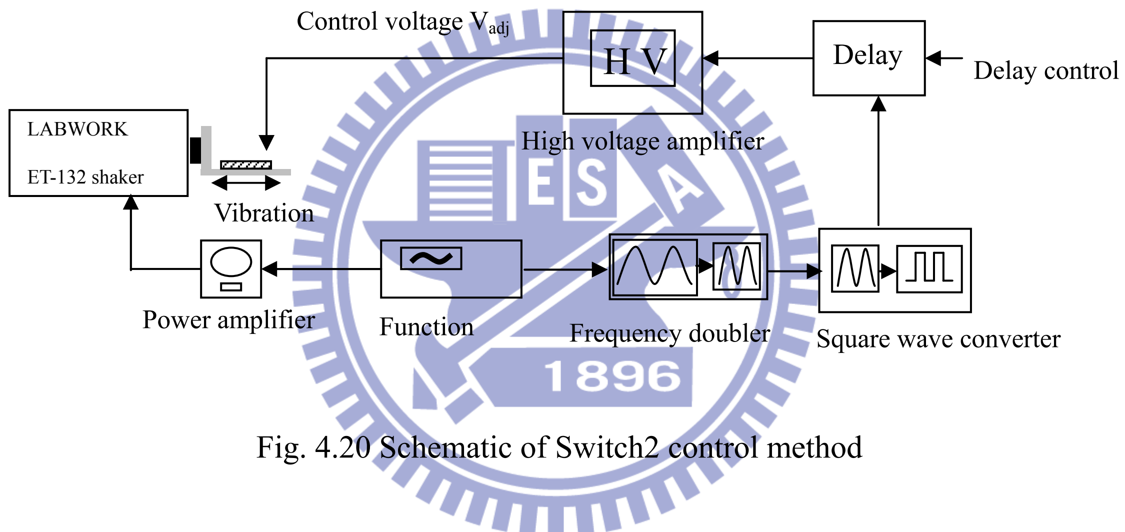

Fig. 4.20 Schematic of Switch2 control method

4.4 Summary

In this chapter, we demonstrated the results of mechanical and electrical measurement. The mechanical results included two parts, one is the MMA data which provide us with the mechanical characteristics of the energy converter. The other is the resonant frequency measured by our shaker and optical microscope. The variable capacitance and parasitic resistance was measured. The measured variable capacitance is less than the theoretical value due to the non-parallel vertical fingers effect caused by ICP etching. Finally the mechanical contact SW1 was tested. The contact resistance was ignorable. However the maximum voltage on the variable capacitor

was far lower than the voltage to trigger the SW2 to close due to non-parallel vertical comb. As a result, the DC power measurement is still in progress.

Chapter 5 Summary and Future work

5.1 Summary

The design and analysis of a DC electrostatic micropower generator with and without external mass attachment were accomplished. The optimal design parameters were found from the theoretical analysis and calculation. With the 1 cm^2 chip area constraint, the device with external mass attachment can generate an output power of 40.5 μW at the output voltage of 40 V by using an external voltage source of 3.6 V. For the device without external mass attachment, the output power is 0.87 μW.

In the fabrication process, LPCVD nitride deposition was adopted to prevent the leakage issue of the device. An accurate shadow mask was used to pattern electrical contact pads in order to avoid the electrical shortage. Gold was used as contact switch material to prevent oxidation corrosion due to its extremely high stability.

The mechanical characteristics of the device were observed by using the MMA and the vibration of shakers. The resonant frequency with and without the 4-gm external mass attachment was measured as 122 Hz and 1680Hz respectively. The results agreed with the device design value. Parasitic resistance was improved to 156MΩ and verified by using discharge time constant measurement. Finally, mechanical switches on the device were tested. The voltage on the variable capacitor had been raised to 14.6V. The pull-in and release voltage of Switch 2 of 98V and 54V were also measured.

5.2 Future work

In DC operation, the variable capacitor is charged initially by an external DC voltage source such as a battery. But the lifetime of the battery limits the application of this converter. Therefore, an AC operation mode is preferred since no net charge is needed to power the load.

The operation of the AC converter is shown in Fig. 5.1. The circuit is composed of an auxiliary power supply V_{in}, a vibration-driven variable capacitor C_v and an external load R_L. The energy converter vibrates with the frequency of the vibration source. This result in the change of the variable capacitance C_v; the charge Q on the capacitor is also changed. Therefore, an AC current flows through the circuit and produces the output voltage V_o and thus the output power to the external load R_L. There is no DC current through the auxiliary power supply V_{in} and therefore it does not provide the net output power. Its lifetime can thus be extended.

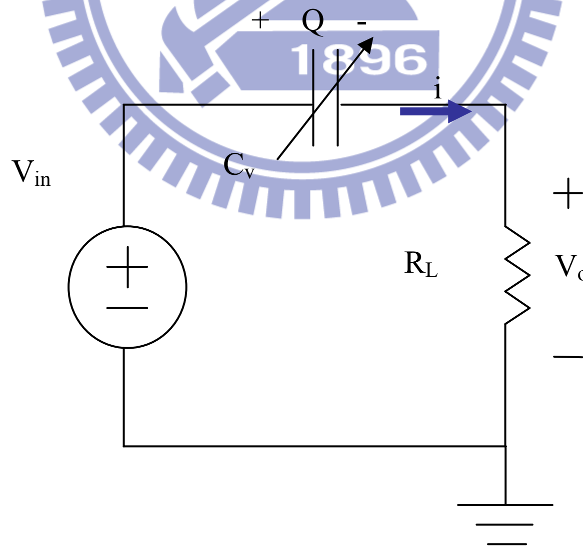

Fig. 5.1 AC mode operation of the electrostatic energy converter

Fig. 5.1 shows the mass-damper-spring model of the variable capacitor. The nonlinear equation of motion can be written as

$$m\ddot{z} + b_m\dot{z} + kz = -m\ddot{x} + F_e \tag{5.1}$$

where x is the displacement of the device frame caused by the vibration, $b_m\dot{z}$ is the mechanical damping force and F_e is the electrostatic force caused by electric charge. The time derivative of Q corresponds to the electric current i flow through the external load R_L as shown in Eq. 5.2.

$$i = \dot{Q} = \frac{V_o}{R_L} = \frac{1}{R_L}(V_{in} - \frac{Q}{C_v})$$

(5.2)

The energy converter can be described by three variables: electric charge Q, displacement z and velocity $\dot{z}$. The output power P of the energy converter is

$$P = i^2 R_L = \frac{1}{R_L}\left(V_{in} - \frac{Q(d^2 - z^2)}{2d\varepsilon L_f hN}\right)^2 \quad (5.3)$$

Therefore, the average output power to the external load R_L can be written as

$$P_{av} = \frac{1}{T}\int_0^T P dt \quad (5.4)$$

This mathematical model can be used to optimize the design parameters for the maximum output power for different initial gap and external load .

Because there is no net charge flows out the source, the auxiliary battery can be replaced by a pre-charged electret. In this case, the potential application of capacitive energe converter is extended.

Theoretical analysis for energy scavenging technology is an essential objective in our effort. Energy from vibration can be converted into the electrical power through different methods such as electrostatic, electromagnetic, and piezoelectric. But difficulties emerge when comparing characteristics between these methods. Thus, a common theoretical description or comparison foundation is one of the next goals for our group.

References

[1] "Battery Power Trade-offs, Low Voltage or Higher Capacity, " EE Times, 2002.

[2] B. Linden and T. Reddy, *Handbook of Batteries*: New York: McGraw-Hill, 2002.

[3] J. N. Harb, R. M. LaFollette, R. H. Selfridge, and L. L. Howe, "Microbatteries for self-sustained hybrid micropower supplies, "*Journal of Power Sources,* vol. 104, pp. 46-51, 2002.

[4] A. Heinzel, C. Hebling, M. Muller, M. Zedda, and C. Muller, "Fuel cells for low power applications, "*Journal of Power Sources,* vol. 105, pp. 250-255, 2002.

[5] M. Daugherty and K. Leonard, "Ultracapacitors for Renewable Energy Storage," SolRanol Inc, Feb. 21, 2009. [Online]. Available: http://www.solrayo.com/SolRayo/Ultracapacitor/Entries/2009/4/3_Ultracapacitor_Presentations_files/Ultracapacitors_for_Renewable_Energy_Storage_Webinar.pdf

[6] L. G. Frechette, C. Lee, S. Arslan, and Y. C. Liu, "Design of a microfabricated rankine cycle steam turbine for power generation," *Proceedings of IMECE'03, ASME International Mechanical Engineering Congress & Exposition,* vol. 16-21, p. 42082, 2003.

[7] H. Li, A. Lal, J. Blanchard, and D. Henderson, "Self-reciprocating radioisotope-powered cantilever," *Journal of Applied Physics,* vol. 92, pp. 1122-1127, 2002.

[8] R. Amirtharajah and A. P. Chandrakasan, "Self-powered signal processing using vibration-based power generation," *Solid-State Circuits, IEEE Journal of,* vol. 33, pp. 687-695, 1998.

[9] S. Roundy, P. Wright, and J. Rabaey, *Energy Scavenging for Wireless Sensor Networks with Special Focus on Vibrations*: Kliwer Academic Press, 2003.

[10] S. O. Kasap, *Optoelectronics and Photonics: Principles amd Practices*, 2001.

[11] S. Lee, “Development of High-efficiency Silicon Solar Cells for Commercialization,” *Journal of Korean Physical Society,* vol. 39, pp. 369-373, 2001.

[12] T. W. Silk and A. J. Schofield, “Thermoelectric effects in anisotropic systems: measurement and applications,” *Condensed Matter - Materials Science,* pp. 1-27, 2008.

[13] G. Savelli, M. P. J. Bablet, C. Salvi, and J. M. Fournier,“Energy conversion using new thermoelectric generator,” *DTIP of MEMS & MOEMS,* 2006.

[14] S. Roundy, D. Steingart, L. Frechette, P. Wright, and J. Rabaey, “Power sources for wireless sensor networks,” in *Wireless Sensor Networks*, 2004, pp. 1-17.

[15] T. Starner, “Human-powered wearable computing,” *IBM Systems Journal,* vol. 35, pp. 618-629, 1996.

[16] Lawrence C. Rome, *et al.*, “Generating electricity while walking with loads,” *Science,* vol 309, pp.1725-1728, 2005.

[17] N. Shenck and J. Paradiso, “Energy scavenging with shoe-mounted piezoelectrics,” *IEEE Micro,* vol. 21, pp. 30-42, 2001.

[18] H. Jonathan,“Starting to explore wind power,” *Physics Education,* vol. 43, p. 572, 2008.

[19] A. S. Holmes, G. Hong, K. R. Pullen, and K. R. Buffard, “Axial-flow micro turbine with electromagnetic generator: Design CFD simulation and prototype demonstration,” *Proc. IEEE MEMS*, pp. 568–571,2004.

[20] S. Roundy, E. S. Leland, J. Baker, E. Carleton, E. Reilly, E. Lai, B. Otis, J. M. Rabaey, P. K. Wright, and V. Sundararajan, “Improving power output for vibration-based energy scavengers,” *Pervasive Computing, IEEE,* vol. 4, pp. 28-36, 2005.

[21] E. Torres and G. Rincón-Mora, "Long-lasting, self-sustaining, and energy-harvesting system-in-package (SIP) wireless micro-sensor solution," *Proceedings of International Conference on Energy, Environment and Disasters (INCEED 2005),* pp. 1-33, 2005.

[22] D. Arnold, "Review of microscale magnetic power generation," *IEEE Transactions on Magnetics.*, vol. 43, pp. 3940–3951, Nov. 2007.

[23] C. B.Williams and R. B. Yates,"Analysis of a micro-electric generator for microsystems," *Proceeding. Transducers'95/Eurosensors IX*, vol. 1, pp. 369–372, Jun. 1995.

[24] N. N. H. Ching, H. Y. Wong, W. J. Li, P. H. W. Leong, and Z. Wen,"A laser-micromachined multimodal resonating power transducer forwireless sensing systems," *Sensor and Actuators A*, vol. 97, pp. 685–690,Apr. 2002.

[25] Perpetuum Limited, PMG17 datasheet, Jan. 7, 2008. [Online]. Available: http://www.perpetuum.co.uk/resource/ PMG17-100_dsheet.pdf

[26] Ferro Solutions, VEH360 datasheet, Jan. 7, 2008. [Online]. Available: http://www.ferrosi.com/files/VEH360_datasheet.pdf

[27] L. Solymar and D. Walsh, *Lectures on the Electrical Properties of Materials*, 5th ed. Oxford, U.K.: Oxford Univ. Press, 1993.

[28] S. Roundy and P. Wright, "A piezoelectric vibration based generator for wireless electronics," *Smart Materials and Structures.*, vol. 13, pp. 1131–1142, 2004.

[29] D. S. Snyder, "Vibrating transducer powersupply for use in abnormal tire condition warning systems," U.S. Patent 4 384 382, May 1983.

[30] D. S. Snyder, "Piezoelectric reed power supply for use in abnormal tire condition warning systems," U.S. Patent 4 510 484, Apr. 1985.

[31] K. E. Reilly and P. Wright, "Thin film piezoelectric energy scavenging systems for an on chip power supply," in *Proceeding International Workshop Micro Nanotechnology Power Generation Energy Conversion Application.*, Berkeley, CA, pp.161–164. Dec, 2006.

[32] B. C. Yen and J. H. Lang, "A variable-capacitance vibration-to-electric energy harvester," *Circuits and Systems I: Regular Papers, IEEE Transactions on,* vol. 53, pp. 288-295, 2006.

[33] I. Kuehne, A. Frey, D. Marinkovic, G. Eckstein, H. Seidel, "Power MEMS—A capacitive vibration-to-electrical energy converter with built-in voltage," *Sensors and Actuators A*, vol.142, p.p.263–269, 2008

[34] T. Sterken, K. Baert, R. Puers, G. Borghs, and R. Mertens, "A new power MEMS component with variable capacitance," *in Proceeding Pan Pacific Microelectronics Symposium,* pp. 27-34, 2003.

[35] S. Meninger, J. O. Mur-Miranda, R. Amirtharajah, A. Chandrakasan, and J. H. Lang, "Vibration-to-electric energy conversion," *Very Large Scale Integration (VLSI) Systems, IEEE Transactions on,* vol. 9, pp. 64-76, 2001.

[36] S.Roundy, P. Wright, and K. Pister, "Micro electrostatic vibration-to-electricity converters," *Proceedings of IMECE ASME International Mechanical Engineering Congress& Exposition*, pp. 17-22, 2002.

[37] D. Hohlfeld, B. Op het Veld, R. J. M. Vullers, J de Boeck, "Coupled-domain modeling of electrostatic energy scavengers and power mamagement circuitry" *powermems2007*, p.p.335-338, 2007

[38] S. Roundy, "Energy scavenging for wireless sensor nodes with a focus on vibration to electricity conversion" PhD thesis, University of California, Berkeley, 2003

[39] Y. Chiu, V F G Tseng, "A capacitive vibration-to-electricity energy converter with integrated mechanical switches," *Journal of Micromechanics and Microengineering,* vol. 18, 104004, 2008.

[40] E. Kreyszig, *Advanced Engineering Mathematics,* 9th ed. (2005) Wiley.

[41] D. Hohlfeld, B. Op het Veld, R. J. M. Vullers, J de Boeck, "Coupled-domain modeling of electrostatic energy scavengers and power management circuit," *proceeding, Power MEMS 2007*, pp. 335-338, 2007

[42] J. Li, Q. X. Zhang, A. Q. Liu, W. L. Goh, and J. Ahn, "Technique for preventing stiction and notching effect on silicon-on-insulator microstructure,"*Journal of Vacuum Science & Technology B: Microelectronics and Nanometer Structures,* vol. 21, pp. 2530-2539, 2003.

[43] V. F. G. Tseng, "Micro capacitive vibration-to-electric energy converter with integrated mechanical switches" Master dissertation, National Chiao Tung University, Hsinchu, ROC, 2007.

[44] J. Karttunen, S. Franssila, and J. Kiihamaki, "Loading Effects in Deep Silicon Etching," *Proceedings of SPIE 2000 International Society of Optical Engineering,* vol. 4174, pp. 90-97, 2000.

[45] M. Orfert and K. Richter, "Plasma enhanced chemical vapor deposition of SiN-films for passivation of three-dimensional substrates," *Surface and Coatings Technology,* vol. 116-119, pp. 622-628, 1999.

[46] G. T. A. Kovacs, *Micromachined Transducers Sourcebook*: McGraw-Hill Companies, 2000.

[47] H. A. Chen, "Optimal Design and Improvement of an Electrostatic Micropower Converter" Master dissertation, National Chiao Tung University, Hsinchu, ROC, 2008.

[48] F. E. H. Tay, X. Jun, Y. C. Liang, V. J. Logeeswaran, and Y. Yufeng, "The effects of non-parallel plates in a differential capacitive microaccelerometer " *Journal of Micromechanics and Microengineering* vol. 4, pp. 283-293, 1999.

APPENDIX A

The M-files used in calculation are listed in Table A.1

Table A.1 M-file used in calculation

M-file	Descriptions
Fun01.m	Nonlinear equation sets
Initial01.m	Parameter setting and result acquiring

Fun01.m

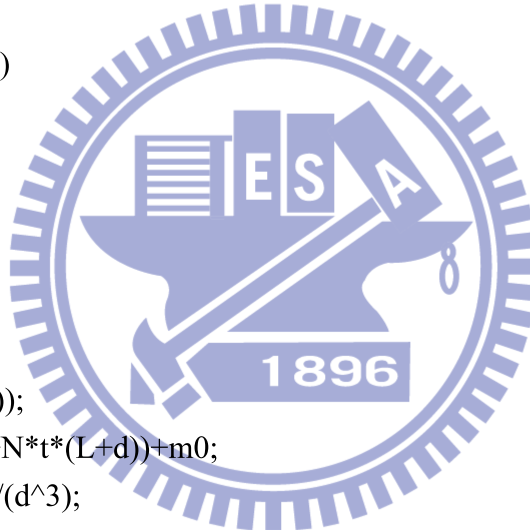

ES
A
1896


```
function F = myfun(x)

w0=2*pi*f;
a0=1.74;
u0=1.82e-5;
e0=8.854e-12;
Sp=S*Sr;
N=Sp/(2*(d+t)*(L+d));
m=rosi*h*(S*(1-Sr)+N*t*(L+d))+m0;
b=(a0*u0*N*L*h^3)/(d^3);
phi=2*N*e0*L*h*d;

%-------------------------------------------------------

  w1= sqrt((k0-phi*vin^2/(d^2-x(7)^2)^2)/m);
  wd1= sqrt(((k0-phi*vin^2/(d^2-x(7)^2)^2)/m)-b^2/(4*m^2));
  w2= sqrt((k0-(Qr^2*phi*vin^2/(d^2-x(7)^2)^2))/m);
  wd2=sqrt((k0-(Qr^2*phi*vin^2/(d^2-x(7)^2)^2))/m-(b^2)/(4*m^2));

%------------------------------------
  A1= (y0*w0*w0)/(((w1)^2-w0^2)^2-(b*w0/m)^2);
  A2= (y0*w0*w0)/(((w2)^2-w0^2)^2-(b*w0/m)^2);
%------------------------------------
```

```
 p1= atan2(b,sqrt(4*(m^2)*((w1)^2)-b^2));
 p2= atan2(b,sqrt(4*(m^2)*((w2)^2)-b^2));
%--------------------------------------------------------------


F=[-w1*(exp(-(0.5*b/m)*x(6)))*(x(1)*sin(wd1*x(6)+p1)-x(2)*cos(wd1*x(6)+p1)) + A1*w0*((w1^2-w0^2)*cos(w0*x(6))+(b*w0/m)*sin(w0*x(6)));

-(w2)*exp(-(0.5*b/m)*(pi/w0+x(6)))*(x(3)*sin((wd2)*(pi/w0+x(6))+p2)-x(4)*cos((wd2)*(pi/w0+x(6))+p2))+(A2)*w0*(((w2)^2-w0^2)*cos(w0*(pi/w0+x(6)))+(b*w0/m)*sin(w0*(pi/w0+x(6))));

exp(-(0.5*b/m)*x(6))*(x(1)*cos(wd1*x(6))+x(2)*sin(wd1*x(6)))+(A1)*(((w1)^2-w0^2)*sin(w0*x(6))-(b*w0/m)*cos(w0*x(6)))+exp(-(0.5*b/m)*(pi/w0+x(6)))*(x(3)*cos((wd2)*(pi/w0+x(6)))+x(4)*sin((wd2)*(pi/w0+x(6))))+(A2)*(((w2)^2-w0^2)*sin(w0*(pi/w0+x(6)))-(b*w0/m)*cos(w0*(pi/w0+x(6))));

exp(-(0.5*b/m)*(x(5)*pi/w0+x(6)))*(x(1)*cos((wd1)*((x(5)*pi/w0+x(6))))+x(2)*sin((wd1)*((x(5)*pi/w0+x(6)))))+(A1)*(((w1)^2-w0^2)*sin(w0*(x(5)*pi/w0+x(6)))-(b*w0/m)*cos(w0*(x(5)*pi/w0+x(6))));

exp(-(0.5*b/m)*(x(5)*pi/w0+x(6)))*(x(3)*cos((wd2)*((x(5)*pi/w0+x(6))))+x(4)*sin((wd2)*((x(5)*pi/w0+x(6)))))+(A2)*(((w2)^2-w0^2)*sin(w0*(x(5)*pi/w0+x(6)))-(b*w0/m)*cos(w0*(x(5)*pi/w0+x(6))));

-(w1)*exp(-(0.5*b/m)*(x(5)*pi/w0+x(6)))*(x(1)*sin((wd1)*(x(5)*pi/w0+x(6))+(p1))-x(2)*cos((wd1)*(x(5)*pi/w0+x(6))+(p1)))+(A1)*w0*(((w1)^2-w0^2)*cos(w0*(x(5)*pi/w0+x(6)))+(b*w0/m)*sin(w0*(x(5)*pi/w0+x(6))))+(w2)*exp(-(0.5*b/m)*(x(5)*pi/w0+x(6)))*(x(3)*sin((wd2)*(x(5)*pi/w0+x(6))+p2)-x(4)*cos((wd2)*(x(5)*pi/w0+x(6))+p2))-(A2)*w0*(((w2)^2-w0^2)*cos(w0*(x(5)*pi/w0+x(6)))+(b*w0/m)*sin(w0*(x(5)*pi/w0+x(6))));

x(7)-(exp(-(0.5*b/m)*(pi/w0+x(6)))*(x(3)*cos((wd2)*(pi/w0+x(6)))+x(4)*sin((wd2)*(pi/w0+x(6))))+(A2)*(((w2)^2-w0^2)*sin(w0*(pi/w0+x(6)))-(b*w0/m)*cos(w0*(pi/w0+x(6)))));];
```

initial01.m

```
format long;
options = optimset('LargeScale','off','TolFun', 1e-32, 'TolX', 1e-32,
'MaxIter',10000,'display','off','MaxFunEvals',100000,'NonlEqnAlgorithm','dogleg');

for vin=3.6;
for Qr=0.5;
for k0=2392;
for d=40e-6;
for Sr=0.8;
for q0=1500:1200; f=0.1*q0;
for m0=4e-3;
for L=400e-6;
for rosi=2330;
for t=1e-5;
for h=200e-6;
for y0=3.9579e-6;
for S=1e-4;

Sp=S*Sr;
N=Sp/(2*(d+t)*(L+d));
m=rosi*h*(S*(1-Sr)+N*t*(L+d))+m0;
w0=2*pi*f;
a0=1.74;
u0=1.82e-5;
e0=8.854e-12;
phi=2*N*e0*L*h*d;
b=(a0*u0*N*L*h^3)/(d^3);

[x,FVAL,flag] = fsolve(@(x) fun01(x,k0,d,vin,Sr,f,m0,L,rosi,t,h,y0,S,Qr),x0,options)
end
end
end
end
end
end
end
```

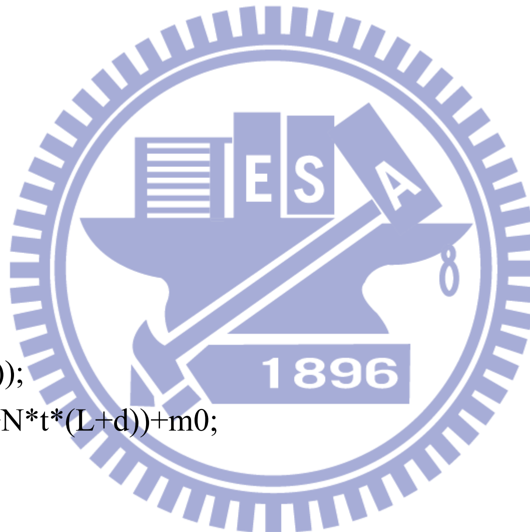

```
end
end
end
end
end
end
end
```